

# **LUMINANCE MONITORING AND DAYLIGHTING CONTROL IN BUILDINGS USING LOW-COST CAMERAS**

by

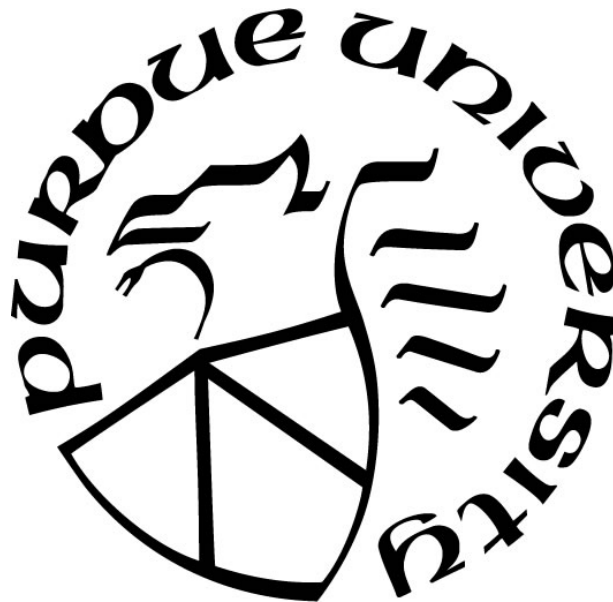
**Michael Y. Kim**

**A Dissertation**

*Submitted to the Faculty of Purdue University*

*In Partial Fulfillment of the Requirements for the degree of*

**Doctor of Philosophy**



Lyles School of Civil Engineering

West Lafayette, Indiana

December 2021

**THE PURDUE UNIVERSITY GRADUATE SCHOOL**  
**STATEMENT OF COMMITTEE APPROVAL**

**Dr. Athanasios Tzempelikos, Co-Chair**

Lyles School of Civil Engineering

**Dr. Iason Konstantzos, Co-Chair**

Durham School of Architectural Engineering and Construction, University of Nebraska-Lincoln

**Dr. Willam T. Horton**

Lyles School of Civil Engineering

**Dr. Mohammad R. Jahanshahi**

Lyles School of Civil Engineering

**Dr. Nusrat Jung**

Lyles School of Civil Engineering

**Approved by:**

Dr. Dulcy M. Abraham

*Dedicated to my parents and my future family members*

## ACKNOWLEDGMENTS

Reminiscing on the last five-year-long journey – which feels like just five seconds – of my Ph.D. degree, I realize how lucky I was to have such wonderful people and environment that made me a more professional, resilient, and humble person.

I would like to express my deepest gratitude to my advisor, Dr. Athanasios Tzempelikos, for guiding me for the past five years. He has been always fully supportive and has allowed me the freedom to pursue studies that fascinated me. As a novice researcher, I was very lucky to partially absorb his high standards of solid knowledge on disciplines and enthusiasm for innovating the building technologies. Whenever I got lost or deviated from my research, or had difficulty in making important research decisions, he always has shown patience and guided me in the right direction without hesitance. He will always be my model of the ideal researcher along the course of my career path in academia (except for the sense of humor). I would also like to thank my committee members, Dr. Iason Konstantzos, Dr. William T. Horton, Dr. Mohammad R. Jahanshahi, and Dr. Nusrat Jung, for their services and priceless comments and suggestions on my Ph.D. work. The financial supports from Lutron electronics, Center for High Performance Buildings, and Purdue Civil Engineering Department is gratefully acknowledged.

I thank all former and present fellow graduate students for making my Ph.D. life in Purdue much more pleasurable. I thank Iason Konstantzos who is my mentor, big brother, and best friend. Your past works served as solid stepping stones for my Ph.D. studies. You may not be happy to hear this but you are the one who most resembles Dr. Tzemplikos as a Fullmetal researcher (but you are the funnier). I'd like to also thank Seungjae Lee, who has known me for over 15 years but became close only 5 years ago. I was very fortunate to have a fellow with such a passion for research (and beer). The small talks we had done in the late night at Herrick Labs sharing our thoughts and passions on buildings will be an unforgettable memory. I'd like to thank Sangwoo Ham for serving as a best beer friend and a roommate. Hope you find a nice lady in sunshine California. There are so many others I want to thank, but I guess I can do it in person. I wish all of you have nice memories of me as I do of you.

Finally, I would like to thank my parents and my brother, who is everything to me. You have been always supporting my dreams. I pray for your happy, healthy, and long life to see how



sparkling my future will be. I will always be a nice and humble person, pursuing the right values following your lives.

# TABLE OF CONTENTS

LIST OF TABLES .....	10
LIST OF FIGURES .....	11
ABSTRACT .....	15
1. INTRODUCTION .....	17
1.1 Background .....	17
1.2 Objectives .....	19
1.3 Thesis overview .....	19
2. LITERATURE REVIEW .....	21
2.1 Daylight glare.....	21
2.1.1 Daylight glare in buildings .....	21
2.1.2 Discomfort glare metrics .....	22
2.2 High Dynamic Range Imaging (HDRI) for luminance measurement .....	25
2.2.1 High Dynamic Range Imaging (HDRI).....	25
2.2.2 Relevant tools for the HDRI .....	28
2.2.3 HDRI application in daylighting research .....	29
Visual comfort studies using HDRI .....	29
Simulation studies using HDRI.....	31
2.2.4 Daylight-linked control systems .....	34
2.2.5 Existing daylight-linked control algorithms .....	35
2.2.6 Current limitations of daylight-linked controls .....	37
2.2.7 Studies on visual comfort oriented DLCs.....	39
2.3 Low-cost camera sensor-based daylighting controls .....	42
2.3.1 Low-cost camera sensor .....	42
2.3.2 Camera sensor-based daylighting control studies.....	44
2.4 Photogrammetry for 3D building interior reconstruction .....	46
2.4.1 Photogrammetry .....	46
2.4.2 Structure-from-Motion – Multiview Stereo pipeline.....	46
2.4.3 Application of 3D reconstruction in building research.....	48

2.5	Research gaps and aims of the thesis.....	48
3.	REAL-TIME DAYLIGHT GLARE CONTROL USING A LOW-COST, WINDOW-MOUNTED HDRI SENSOR .....	51
3.1	Scope and objectives of the study.....	51
3.2	Low-cost image sensor .....	51
3.3	Glare source detection and positioning for glare control.....	52
3.3.1	Overall Process .....	52
3.3.2	HDRI Photometric and Geometric calibration .....	53
3.3.3	Glare source detection .....	58
3.3.4	Glare source positioning.....	60
3.3.5	Solar Tracking for daylight glare control using fisheye HDRI sensor .....	62
3.4	Glare-based shading operation using the window-mounted HDRI sensor.....	64
3.5	Implementation of the HDRI-based glare control framework and case study.....	68
3.5.1	Experimental setup and control integration with the Building Management System.....	68
3.5.2	Implementation and comparison with common shading controls for glare protection . .....	70
3.6	Chapter conclusion.....	75
4.	A LOW-COST FISHEYE-STEREO CAMERA SENSOR FOR DAYLIGHTING AND GLARE CONTROL .....	77
4.1	Scope and objectives of the study.....	77
4.2	Fisheye-Stereovision System.....	77
4.3	Fisheye-Stereovision Sensor Calibration.....	79
4.3.1	Photometric calibration.....	79
4.3.2	Geometric calibration .....	80
4.4	Positioning of glare sources.....	81
4.5	Overflow correction for the solar disk.....	84
4.6	Sensor validation.....	85
4.7	Chapter discussion and conclusion .....	86
5.	NON-INTRUSIVE LUMINANCE MONITORING FRAMEWORK VIA HIGH DYNAMIC RANGE IMAGING AND PHOTOGRAMMETRY .....	88
5.1	Scope and objectives of the study.....	88

5.2	Framework overview .....	88
5.3	Devices & calibration .....	89
5.3.1	Photometric calibration.....	90
5.3.2	Geometric calibration .....	92
5.4	Data collection and preprocessing .....	95
5.4.1	Video and image collection .....	95
5.4.2	Data pre-processing .....	96
5.5	Photogrammetry task pipeline .....	97
5.5.1	COLMAP sparse model reconstruction.....	98
5.5.2	OpenMVS dense point cloud & mesh reconstruction .....	100
5.6	Luminance re-projection.....	101
5.7	Implementation of non-intrusive luminance monitoring framework and experimental performance evaluation.....	107
5.7.1	Experimental setup .....	107
5.7.2	Experimental procedure, data analysis and performance evaluation.....	109
5.8	Discussion .....	112
5.9	Chapter conclusion.....	114
6.	PERFORMANCE EVALUATION OF NON-INTRUSIVE LUMINANCE MAPPING TOWARDS HUMAN-CENTRIC DAYLIGHTING CONTROL .....	117
6.1	Experimental evaluation and data analysis .....	117
6.1.1	Experimental setup .....	117
6.1.2	Experimental procedure and data collection.....	119
6.2	Performance evaluation .....	120
6.2.1	Structural Similarity Index Measure (SSIM).....	121
6.2.2	Visual comfort metrics comparison – DGP and Ev.....	122
6.2.3	Region-by-region analysis .....	122
6.2.4	Receiver Operating Characteristic (ROC) Curve .....	123
6.3	Results.....	126
6.3.1	Data statistics, overall and regional similarity measure of re-projected luminance .....	127
6.3.2	Visual comfort metrics using re-projected luminance maps .....	130
6.4	Discussion .....	133

6.5 Chapter Conclusion.....	135
7. FUTURE WORKS .....	138
7.1 Development of open-toolset for High Dynamic Range Imaging application .....	138
7.2 Improvement of luminance re-projection framework for non-intrusive luminance mapping .....	139
7.3 Luminance-based human-centric daylight-linked control .....	140
VITA .....	158
PUBLICATIONS.....	159

## LIST OF TABLES

Table 2.1 Glare metric thresholds .....	24
Table 3.1 Camera settings for HDR image creation .....	54
Table 5.1 Camera settings for HDR image creation .....	91
Table 5.2 RGB projections and depth maps from reconstructed 3D models.....	101
Table 5.3 2D projections before and after Open3D modification. ....	103
Table 5.4 Pinhole-projected images with varying focal lengths.....	105
Table 5.5 Mathematical representations of camera projections used .....	105
Table 5.6 Equidistant fisheye projection pseudo-algorithm .....	106
Table 5.7 Experimental data statistics .....	112
Table 6.1 Interpretation of AUC value .....	124
Table 6.2 DGP classification for ROC analysis.....	125
Table 6.3 Optimization metrics for cut-off determination.....	126
Table 6.4 Data statistics .....	128
Table 6.5 MSSIM statistics by region.....	129
Table 6.6 Error statistics of visual comfort metrics using re-projected luminance maps.....	130
Table 6.7 Error statics of visual comfort metrics from interior-masked luminance maps .....	132
Table 6.8 Optimized cut-off values from ROC analysis.....	133

## LIST OF FIGURES

Figure 1.1 Typical side-lit open-plan office [17].....	17
Figure 2.1 False color luminance map displayed in Photosphere [73] .....	25
Figure 2.2 Camera response curve estimation from LDR images via Photosphere software [27,74] .....	26
Figure 2.3 The vignetting function of Nikon FC9 fisheye lens. a) Measured data points and the vignetting function derived to fit the measured points; b) digital filter developed based on the vignetting function [27] .....	27
Figure 2.4 Sigma 4.5mm F2.8 fisheye projection and equidistant fisheye projection [76] .....	28
Figure 2.5 Photosphere software [74] .....	28
Figure 2.6 Evalglare glare detection. a) original HDR image; b) Evalglare check HDR image with color-mapped glare sources .....	29
Figure 2.7 Rendered objects with different HDR images as a light source through IBL [85] .....	32
Figure 2.8 Comparison of the HDR image of the sky, IBL simulation, and generalized sky modelled simulation under clear sky conditions [88] .....	32
Figure 2.9 Experimental setup of cameras in [87] .....	33
Figure 2.10 Relative error of the 5 computed work plane illuminances compared with lux-meter values for an overcast sky [90] .....	34
Figure 2.11 Integrated lighting and daylighting control [23] .....	35
Figure 2.12 Cut-off strategy [101] .....	36
Figure 2.13 ‘Buffer zone’ concept: graph showing automated shading position to prevent direct sunlight falling on the work plane area at all times [114] .....	36
Figure 2.14 Vertically mounted SPN1 pyranometer [110] .....	37
Figure 2.15 Flowchart of MBC developed by Xiong and Tzempelikos [110] .....	40
Figure 2.16 Outline of DLC proposed by Iwata et al. [132] .....	41
Figure 2.17 IcyCAM HDR vision sensor equipped with fisheye lens [48] .....	43
Figure 2.18 Pi Camera & Raspberry Pi 3B+ [137] .....	44
Figure 2.19 Sensitivity analysis of DGP with respect to translational and angular displacement [140] .....	45
Figure 2.20 3D reconstruction using SfM-MVS pipeline [149] .....	47

Figure 3.1 Original image sensor and HDRI sensor with lens connected to Raspberry Pi (left); HDRI sensor attached to window using a 3D printed mount (right) .....	52
Figure 3.2 Overall process for HDRI and glare detection .....	53
Figure 3.3 Illustration of fisheye camera projection model.....	56
Figure 3.4 (a) Original fisheye projection (b) Equidistant projection. Each circle corresponds to equal $\theta$ (from 10 degrees to 90 degrees, in 10-degree increments).....	57
Figure 3.5 Estimated fisheye camera projection and fitted equidistant projection with a polynomial function .....	57
Figure 3.6 Vertical illuminance validation .....	58
Figure 3.7 (a) Example of a processed HDR image for Evalglare analysis; (b) Example of color-mapped glare sources from the Evalglare output. The HDRI sensor identifies the location, size and brightness of a potential glare source in real-time. ....	60
Figure 3.8 Illustration of proposed logic for finding the lowest profile angle of glare sources ...	62
Figure 3.9 Solar tracking example from a processed HDR fisheye image .....	63
Figure 3.10 Comparison of the profile angle calculated from HDR images and Sun-path method (left). Overlay of solar disk on fisheye HDR images (right) .....	64
Figure 3.11 Illustration of shade control operated by the new sensor-based control system. Eye-height protection from exterior glare source system (top); Work plane protection from direct sunlight (bottom).....	65
Figure 3.12 Glare protection flowchart with HDRI sensor.....	66
Figure 3.13 Illustration of angular deviation caused by different distances from the glare source (top); Ratio of tangents of the angles $\delta$ and $\Omega$ dependent to glare source distance from the window (bottom).....	68
Figure 3.14 Instrumentation schematic (left); observed scene with the exterior glare source (reflector) visible from the interior of the test office, and additional sensors installed at the occupant location (right) .....	69
Figure 3.15 Overview of HDRI sensor and shading control integration in the BMS.....	70
Figure 3.16 HDR images from the implementation case study: Exterior Scene (a) and occupant views with the solar-tracking control (b); excessive illuminance control (c); and HDRI-based control (d), fully protecting from the detected glare source. ....	72
Figure 3.17 40 data points (x-axis) sorted by average luminance of the reflector in ascending order (top) and comparison between respective shade positions, DGP and vertical illuminance at the occupant position, with each shading control. ....	74
Figure 4.1 Overview of fisheye-stereo vision sensing system.....	77
Figure 4.2 Raspberry Pi B+ with IVMECH V2 camera multiplexer (left). Fisheye camera integrated with 3D printed mount (right).....	78



Figure 4.3 Fisheye stereovision sensor mounted attached to window .....	78
Figure 4.4 Measurable luminance range by fisheye-stereovision.....	80
Figure 4.5 Generic fisheye camera model .....	81
Figure 4.6 Epipolar lines in rectified stereo image pair.....	82
Figure 4.7 Template-matching in rectified stereo image pair.....	83
Figure 4.8 3D Positioning from the disparity .....	84
Figure 4.9 Overflow correction for solar disk pixels.....	85
Figure 4.10 Stereo-depth validation.....	85
Figure 4.11 Vertical illuminance validation. Horizontal error bar shows measurement error ( $\pm 5\%$ ) for LI-COR photometer .....	86
Figure 5.1 Overview of the proposed framework.....	89
Figure 5.2 Photometric calibration for HDRI sensor.....	90
Figure 5.3 Estimated camera response function .....	91
Figure 5.4 Vignetting curve (left). Vignetting correcting function (middle). Vignetting correcting mask (right).....	92
Figure 5.5 Geometric calibration for HDRI sensor and user-owned camera device.....	94
Figure 5.6 Intrinsic-preserving fisheye rectification example .....	94
Figure 5.7 Example video frames extracted from Video A .....	95
Figure 5.8 Rectified video frames example extracted from Video B .....	97
Figure 5.9 Text file creation for camera translation vectors .....	97
Figure 5.10 Overview of photogrammetry task pipeline .....	98
Figure 5.11 Example sparse reconstruction rendered in COLMAP-GUI.....	99
Figure 5.12 Rendered views of textured mesh model.....	101
Figure 5.13 Luminance re-projection pipeline.....	102
Figure 5.14 Left: Rectified LDR image captured by HDRI sensor; Middle: Mesh projection into 3-channel texture map; Right: Mesh projection into single channel depth map.....	102
Figure 5.15 Luminance map re-projection.....	104
Figure 5.16 Equidistant-fisheye luminance maps (occupant camera-captured vs. re-projected) .....	106
Figure 5.17 Instrumentation and space layout for Experiment I (left: side view; right: top view) .....	108
Figure 5.18 Interior view of test office with two camera sensors installed .....	108

Figure 5.19 HDR images captured by Sensor I during a sunny day .....	109
Figure 5.20 False-color luminance maps comparison: occupant camera-measured vs re-projected .....	111
Figure 5.21 Scatter plot of DGP, Lavg and Ev with RSME for each metric (re-projected quantities vs. actual measurements from occupant position) .....	112
Figure 5.22 Scatter plot of DGP, Lavg and Ev with RSME for each metric with increased window views and open shades (re-projected quantities vs. actual measurements from occupant position) .....	114
Figure 6.1 Instrumentation and space layout for experiment (left: side view; right: top view) .	118
Figure 6.2 Interior view of testbed office .....	118
Figure 6.3 LDR images captured by HDRI sensors (a) Sensor I (b) Sensor II (c) Sensor III ....	119
Figure 6.4 Fisheye transformation example. Concentric circles represent incident angles with 10- degree increment (a) Original Sensor I projection (180-degree FOV); (b) Output equidistant fisheye projection (170-degree FOV) .....	120
Figure 6.5 Masks by region. (a) Interior; (b) Window; (c) Task; and (d) Computer screen as seen from occupant Sensor I .....	123
Figure 6.6 Masked luminance map with interior region-only as seen from occupant sensors (a) Sensor I (b) Sensor II .....	123
Figure 6.7 Representative false-color luminance maps comparison: occupant camera-measured vs re-projected maps.....	127
Figure 6.8 Visual comfort metrics distribution from luminance maps .....	128
Figure 6.9 MSSIM distribution.....	128
Figure 6.10 MSSIM distribution by region.....	129
Figure 6.11 Scatter plot comparison of visual comfort metrics (re-projected vs measured luminance maps).....	130
Figure 6.12 Relative error histograms of visual comfort metrics .....	131
Figure 6.13 Scatter plot comparison of visual comfort metrics from interior-only luminance maps .....	132
Figure 6.14 ROC curves from re-projected visual comfort metrics .....	133

## ABSTRACT

Daylighting has a significant impact on occupants, including not only visual comfort and visual task performance but also on workplace satisfaction and psychophysiological responses such as alertness, mood, and circadian rhythm. Intelligent, dynamic control of daylight via a building automation system is therefore crucial to maximizing the positive impacts of daylight provision in perimeter offices. However, existing daylight-linked controls (DLCs) lacks the fundamental ability to govern indoor luminous condition in a human-centric manner. It is mainly because the sensing technologies – such as ceiling-mounted photosensor - adopted in current DLCs are incapable of monitoring sufficient physical variables to suit such purpose. Hence, this Thesis aims to utilize a High Dynamic Range Imaging (HDRI) sensor in DLCs to unlock abilities to enhance human-centric features that have not been possible with conventional photosensors. The sensor, made of a low-cost programmable camera can capture a wide-area luminance distribution highly correlated with occupant visual perception, compared to conventional illuminance-based metrics.

This Thesis begins with a development of a window-mounted HDRI sensor for real-time detection of potential glare sources including the sun. The sensor can capture the full luminance distribution of the exterior scene visible through the window and identify and locate potential sources of glare. To overcome the pixel-overflow by the extreme luminance of the sun and to estimate the accurate 3D position of the glare sources, the HDRI sensor was upgraded into a new fisheye-stereovision sensor made of dual cameras with different exposures. Experiments in full-scale offices showed that the calibrated window-mounted HDRI sensor can efficiently identify and locate potential glare sources in real time. The daylight control implementation included integration with shading controls to mitigate the risk of glare and comparison with conventional shading operation.

Monitoring of indoor luminance distribution is equally important for human-centric DLCs. There are practical challenges in utilizing the HDRI sensor for monitoring luminance distribution perceived from the occupant perspective. Therefore, a new framework was developed for non-intrusive monitoring of luminance distribution perceived from occupant field-of-view (FOV), using a fisheye HDRI sensor installed at a non-intrusive position. The framework leverages the

state-of-the-art photogrammetry (Structure-from-Motion – Multiview Stereo) pipeline to automatically reconstruct 3D surfaces of the room, which will be used for re-projection of luminance map captured by HDRI sensor into occupant FOV.

To validate the performance of the framework, a systematic performance evaluation was conducted in a real-office experiment under variable lighting conditions to compare the re-projected luminance maps and the actual luminance measurement captured from occupant positions.

# 1. INTRODUCTION

## 1.1 Background

Daylighting is an essential part of commercial building design and operation. Daylight harvesting significantly reduces electricity consumption from artificial lighting, which accounts for at least 17% of energy use in U.S. commercial buildings [1–3]. Its apparent impact on building occupants’ visual comfort and satisfaction as well as visual task performance has been proven through various studies in past decades [4–6]. Also, non-image-forming (NIF) effects of daylight play an important role in human physiological and psychological functions, such as circadian rhythm, alertness, mood, gaze behavior and occupational stress [4,7,16,8–15]. A major challenge associated to maximizing the daylighting potential in perimeter building zones is visual discomfort (daylight glare), which can be induced by excessive daylight or luminance patterns in the field of view of the occupants.



Although the most efficient way to maintain visually comfortable conditions in the building interior is through performance-based design of façade and seating layouts [18–22], in cases of existing buildings, daylight-linked controls (DLC) can be cost-effective solutions. The most common form of automatic, closed-loop DLC is comprised of movable shading devices (or

dynamic glazing systems) integrated with dimmable lights, designed to block direct sunlight for glare mitigation and then adjust dimming levels of lighting fixtures to maintain target illuminance on the work plane [23].

Despite the potential benefits of the automated DLCs, they are not as widespread as one would expect, according to [24]. In a survey targeted U.S facility managers where 78% of respondents comprised of commercial or institutional buildings, it was reported that only 35% of their facilities are equipped with daylighting controls. To facilitate the wide adoption of automated DLC mentioned above, the performance and robustness of DLCs need improvement, particularly in terms of visual comfort. Even the most advanced forms of DLCs – including Model-Based Controls (MBC) or visual comfort-oriented controls – frequently fail to deliver comfort to occupants or provide over-protection from glare compromising the daylight provision.

The fundamental basis for the poor visual comfort delivered by existing photosensor-based DLCs is associated with the lack of sensing capabilities for measuring critical indices, such as luminance distribution of interior and exterior of the room, or detection of the sun. If the exterior luminance distribution can be measured, it is possible to identify potential glare sources of extreme luminance that cannot be detected from photosensors. Also, it is possible to detect and track the sun regardless of location or surrounding environment of the buildings. In case the indoor luminance distribution can be monitored, then the DLC will provide higher satisfaction to occupants by maintaining visually comfortable luminous condition.

Low-cost camera sensors coupled with the High Dynamic Range Imaging (HDRI) technique have the potential to address the current limitations of photosensor-based DLCs. HDRI allows retrieval of luminance maps by merging low dynamic range (LDR) images [25,26]. The accuracy of luminance maps acquired from HDRI has been validated [27–29] and well-established through efforts from several research groups in lighting research domain [30–35]. Most commonly, researchers attempted to associate scene luminance characteristics, measured by HDR images, to subjective visual comfort [20,21,36–43]. Those studies mainly focused on the development and validation of daylight glare metrics based on occupant-perceived luminance distribution.

Despite the obvious potential of employing HDRI techniques for acquiring luminance maps and initial efforts of application in DLCs [44–48], such studies are scarce and need further investigation.

## 1.2 Objectives

The objectives of this thesis are:

1. To develop a low-cost HDRI sensor for real-time, accurate luminance map acquisition for monitoring the interior and exterior of the room.
2. To develop a new daylighting control framework based on a window-mounted HDRI sensor, that identifies potential glare sources and provides adequate real-time protection to the occupants.
3. To develop a new fisheye-stereo HDRI sensor to solve the limitation of low-cost monovision HDRI sensors – luminous overflow and positioning ambiguity - for exterior luminance monitoring.
4. To develop a semi-automated method for monitoring of occupant-perceived luminance distribution within the visual field, based on the state-of-the-art computer vision techniques.

## 1.3 Thesis overview

Chapter 2 presents a thorough review of existing DLCs and their limitations, HDRI experimental studies on assessment of human visual comfort and HDRI sensor-based controls, and photogrammetry and its application in building research domain. Remaining research gaps in the literature and overall aims of this thesis are also included.

Chapter 3 presents a novel daylighting control framework based on a window-mounted, fisheye HDRI sensor. The scope of the study includes the development and calibration of the HDRI sensor, glare source identification, and positioning algorithms via HDRI, and shade control logics for glare mitigation based on the exterior luminance map.

Chapter 4 presents the development of a fisheye-stereovision HDRI sensor, as an amendment to the fisheye-monovision HDRI sensor, to address issues identified in Chapter 3. The new sensor is capable of capturing a solar disk through the window, without causing luminous overflow – a common phenomenon in low-cost cameras with limited dynamic range- and also estimating the 3D position of potential glare sources through the window.

Chapter 5 presents a semi-automated framework for non-intrusive monitoring of luminance distribution perceived from occupant field-of-view (FOV), using a fisheye HDRI sensor installed at a non-intrusive position. The framework leverages the state-of-the-art photogrammetry (Structure-from-Motion – Multiview Stereo) pipeline to automatically reconstruct 3D surfaces of the room, which will be used for re-projection of luminance map captured by HDRI sensor into occupant FOV.

In Chapter 6, the performance of the non-intrusive luminance monitoring developed in Chapter 5 is evaluated via experimental validation. The framework is implemented in real office-like testbed in various conditions to compare the re-projected luminance maps and the actual luminance measurement captured from occupant positions.

Conclusions, extensions and recommendations for future work are presented in Chapter 7.



## **2. LITERATURE REVIEW**

### **2.1 Daylight glare**

#### **2.1.1 Daylight glare in buildings**

According to Lighting Handbook of the Illuminating Engineering Society of North America, definition of glare is “ the sensation produced by luminance within the visual field that is sufficiently greater than the luminance to which the eyes are adapted to cause annoyance, discomfort or loss in visual performance and visibility” [49]. Glare can be categorized into two types: disability glare and discomfort glare. Disability glare refers to “the masking effect caused by light scattered in the ocular media which produces a veiling luminance over the field of view” [50]. When disability glare is present, occupants experience immediately reduced visual performance and inability to see for a period of time. The knowledge of disability glare is now well established and modelled in CIE Disability Glare formulae [51].

Discomfort glare is a phenomenon arising from high luminance contrast or undesirable luminance distribution within the visual field, causing discomfort [52]. When discomfort glare occurs, occupants may not notice immediate degradation of visual performance, however, may experience progressive degradation of the visual performance and premature tiring of eyes or other symptoms such as headaches [53]. Despite the number of related studies over the past 80 years, complete understanding of discomfort glare is yet and still being an active research topic among researchers [12]. It is mainly because discomfort glare is rather subtle and subjective phenomenon that is closely linked to a person’s perception of overall indoor environment, not only regarding the luminous condition, but also many other factors such as preference of outdoor view, personal difference, type of task, or psychological factors [16,54]. The variability of the above factors, also with time, does not allow the straightforward development of a robust universal metric for daylight discomfort glare, and existing studies are not designed according to grouping of these factors [55].

In day-lit perimeter offices, the main concern in terms of visual comfort is discomfort glare, since it occurs most frequently during daylight hours and identification of disability glare is rather obvious thus can be addressed immediately. [56] reviewed some post-occupancy evaluation (POE) studies on day-lit open plan observed high percentages of occupants who have glare issues. In [57],

a POE study of open plan offices in Brisbane 56% of occupants reported discomfort from daylight and electric lighting. In another study by the same author, 49% of 493 occupants of green buildings in Brisbane reported visual discomfort [52]. [20] found that 60-70% of 44 occupants in open-plan offices in San Francisco reported visual discomfort from windows, of which 20% referred to ‘very uncomfortable’.

### 2.1.2 Discomfort glare metrics

Despite the subjective nature of discomfort glare, there have been several efforts to develop metrics for generalized prediction of daylight glare. Generally, the development of glare indexes is based on laboratory-type human experiments to collect coupled data of human subjective glare ratings and objective measurements. Despite the difference in individual variables and exponents of those metrics, they can be expressed in a generalized equation as Eq 2.1[42]:

$$G = \log \sum_{i=1}^n \left( \frac{L_{s,i}^{exp} \omega_{s,i}}{L_b^{exp} f(\psi)} \right) \quad (2.1)$$

The parameters in this general form as follows:

- $G$  is glare index which predicts the subjective glare sensation;
- $n$  is number of detected glare sources;
- $exp$  is a weighting exponent for each variable;
- $L_b$  is background luminance which determines the adaptation levels of the observer’s eye;
- $L_s$  is glare source luminance;
- $\omega_s$  is the solid angle subtended by the source, indicating its perceived size;
- $f(\psi)$  is the angular displacement of the source from the observer’s line of sight

### *Daylight Glare Index (DGI)*

The earliest metric for daylight glare was Daylight Glare Index (DGI) or Cornell Equation, formulated by Hopkinson in 1972 (Eq 2.2):

$$DGI = 10 \cdot \log_{10} \left( 0.48 \sum_{i=1}^n \frac{L_{s,i}^{1.6} \omega_{pos s,i}^{0.8}}{L_b + 0.07 \omega_{s,i}^{0.5} L_{s,i}} \right) \quad (2.2)$$

where  $\omega_{pos}$  is the solid angle of the glare source with modification for its position in the field of view. DGI was developed from a modification of Glare Index, his former work focused on small

glare sources [58]. Unlike Glare Index, DGI accounts for the large glare sources, particularly, diffuse sky patch visible through the window. The equation was developed through experiments using the artificial light source (fluorescent lamps) behind an opal-diffusive screen. However, validation studies on DGI show that the correlation between the prediction and self-reported daylight glare sensation is not as strong as in the original study [58–60], despite the several attempts to modify the mathematical formulation through continued human experiments [61,62]. However, neither of the DGI variants gain wide acceptance in practical building design [63].

### ***CIE Glare Index (CGI)***

In 1979, Einhorn developed CIE Glare Index, primarily built upon DGI and was adopted by CIE. The equation form is as below:

$$CGI = C_1 \log_{10} C_2 \frac{1 + \frac{E_d}{500}}{E_d + E_i} \sum_{i=1}^n \frac{L_{s,i}^2 \omega_{s,i}}{P_i^2} \quad (2.3)$$

where  $E_d$  is direct vertical illuminance at eye,  $E_d$  is diffuse vertical illuminance at eye, and  $p_i$  is Guth's position index which grows larger as a glare source located further from center of human FOV [64]. In this metric, the adaptation level to the glare sources is encoded as a function of ratio between diffuse and direct vertical illuminance at eye. The major limitation of metric is that the derivation of equation did not involve human experiments.

### ***Daylight Glare Probability (DGP)***

In 2006, Wienold and Christofferson developed Daylight Glare Probability, based on the equation form of CGI [42] formulated as below:

$$DGP = 5.87 \cdot 10^{-5} E_v + 9.18 \cdot 10^{-5} \log_{10} 2 \left( 1 + \sum_{i=1}^n \frac{L_{s,i}^2 \omega_{s,i}}{E_v^{1.87} P_i^2} \right) \quad (2.4)$$

where  $E_v$  is vertical illuminance at eye. A major difference of DGP from its predecessors is that DGP was designed to predict the percentage of people who experience visual discomfort, rather than the glare sensation of a so-called “standard observer”. It was intended to make the new metric more accountable for individual difference in glare perception observed in their data. Another major difference is the inclusion of  $E_v$  as measure of both overall brightness and adaptation level, instead of using  $L_b$ . An glare analysis tool, evalglare [65] based on RADIANCE (an open-source

backward-tracking lighting simulation tool)[66] was used for derivation of the DGP. In their study DGP demonstrated a very strong correlation ( $R^2=0.94$ ) with the subjective glare perception of the subjects. A limitation of glare metrics based on luminance distribution within human FOV, including the DGP, is that an annual simulation of the metrics is computationally expensive. Simplified Daylight Glare Probability (DGPs) and enhanced Daylight Glare Probability (eDGP) are simplification of DGP for faster computation, that are primarily based on vertical illuminance at eye and simplified rendering image (only for eDGP) [67,68]. DGPs and eDGP both showed very strong correlation to the original DGP when direct radiation such as sunlight did not hit the observer's eye. The equation for DGPs is as below (Eq. 2.4):

$$\text{DGPs} = 6.22 \cdot 10^{-5} E_v + 0.184 \quad (2.4)$$

DGP is currently accepted as a reliable glare index in the literature [18,37,69] and showed better prediction compared to DGI in studies [15,36,42,70]. Some studies identified inconsistent predictions in certain cases such as sun in the visual field or in dimmed area such as core zones [20,38,52]. Nevertheless, a recent study [71] evaluated performance and robustness of 22 established and newly proposed glare prediction metrics, using datasets from six locations in the world, and found that DGP is the most robust, while optimizing its numerical coefficients or special condition should be studied in future studies.

### ***Glare metric thresholds***

Commonly used thresholds for above glare metrics are presented in Table 2.1 [18]:

Table 2.1 Glare metric thresholds

	DGI	CGI	DGP
Imperceptible	<18	<13	<0.35
Perceptible	18-24	13-22	0.35-0.40
Disturbing	24-31	22-28	0.40-0.45
Intolerable	>31	>28	>0.45

However, Pierson [72] revealed that the thresholds from field study were systematically lower than the laboratory ones, implicating that the discomfort glare is reported with lower stimulus in the real offices. The possible reasons for the phenomenon described by the authors are

anchor bias, difference in stimulus distribution between the laboratory and field data, experience effect, user expectation towards a familiar environment, type of participants, and broader context in which the subjective assessment is collected.

## 2.2 High Dynamic Range Imaging (HDRI) for luminance measurement

### 2.2.1 High Dynamic Range Imaging (HDRI)

The traditional method of measuring accurate luminance was using an expensive, scientific-grade luminance spot meter. However, such method is infeasible for acquisition of a scene visible from human eyes since the device can only measure a very small region at a time. A new method of luminance measurement using a camera device was then proposed, named High Dynamic Range Imaging (HDRI).

HDRI is a technique that allows of capturing of per-pixel luminance maps by merging camera photographs with bracketed exposures [25,26]. This technique allowed us to capture a detailed luminance distribution without using a numerous luminance spot meters, making luminance measurement more feasible. Combining a wide-angle fisheye lens with the camera allows to capture luminance maps within full human FOV spanning near 180 degrees. The accuracy of the HDRI luminance measurement was proven, exhibiting error margin around 10% across the several validation studies [27–29] and well-established as a solid methodology through efforts from several research groups [30,31,33].

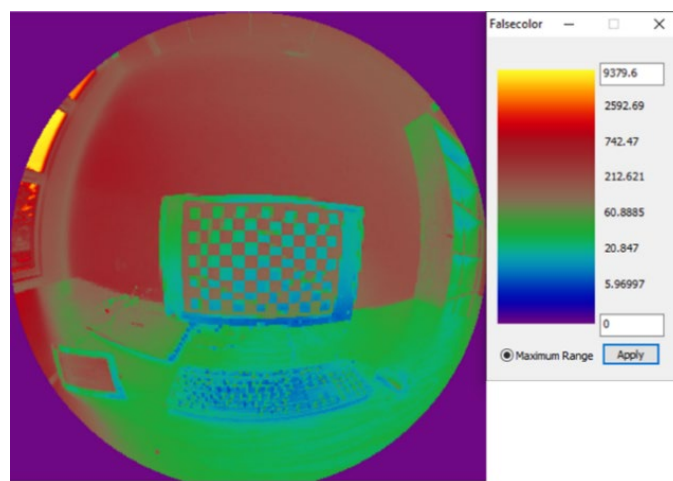


Figure 2.1 False color luminance map displayed in Photosphere [73]

For acquisition of fisheye luminance map for visual comfort assessment through HDRI, proper photometric and geometric calibration is required. Photometric calibration is essential for accurate per-pixel luminance measurement. It includes estimation of camera response function (CRF) which is non-linear relation between the measured intensity and radiometric intensity. Inverse of CRF is used to recover low dynamic range (LDR) images with linear CRF that in turn will be merged into a single HDR image via weighted averaging [26]. Vignetting effect refers to gradual degradation of luminance on the pixels closer to periphery of the image; it is a typical phenomenon in cameras with small apertures (such as fisheye camera lens). Vignetting can be corrected by estimating the light fall-off curve as a function of pixel from the principal point (image of the camera center) and then applying the inverse function to the luminance map taken. The detailed procedure is well detailed in [27,33]. Lastly, absolute luminance calibration, a retrieval of calibration factor -multiplier to match the vignetting-corrected HDR luminance map into the real luminance value – is done.

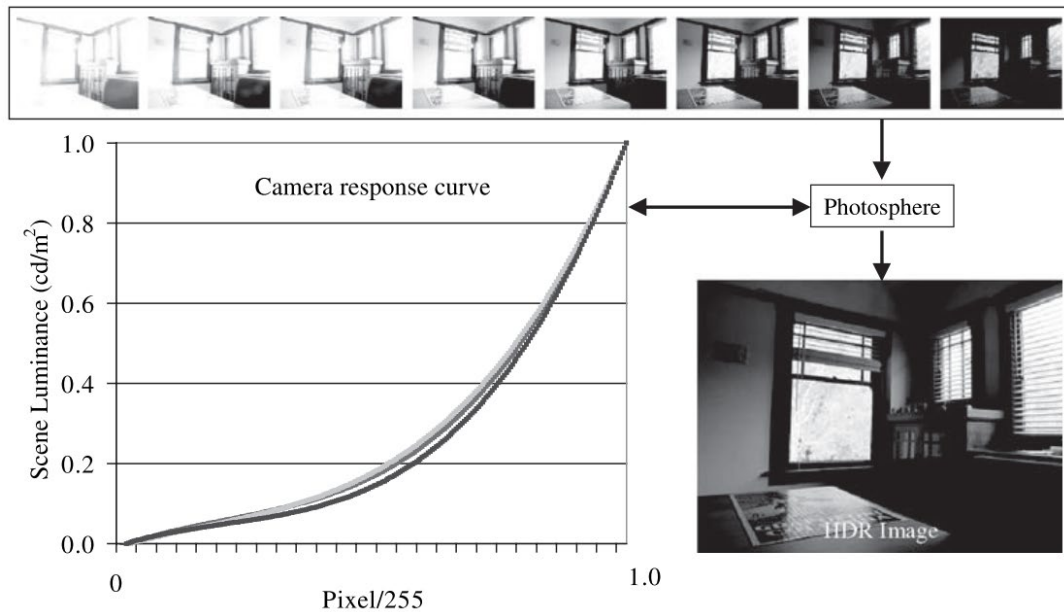


Figure 2.2 Camera response curve estimation from LDR images via Photosphere software [27,74]

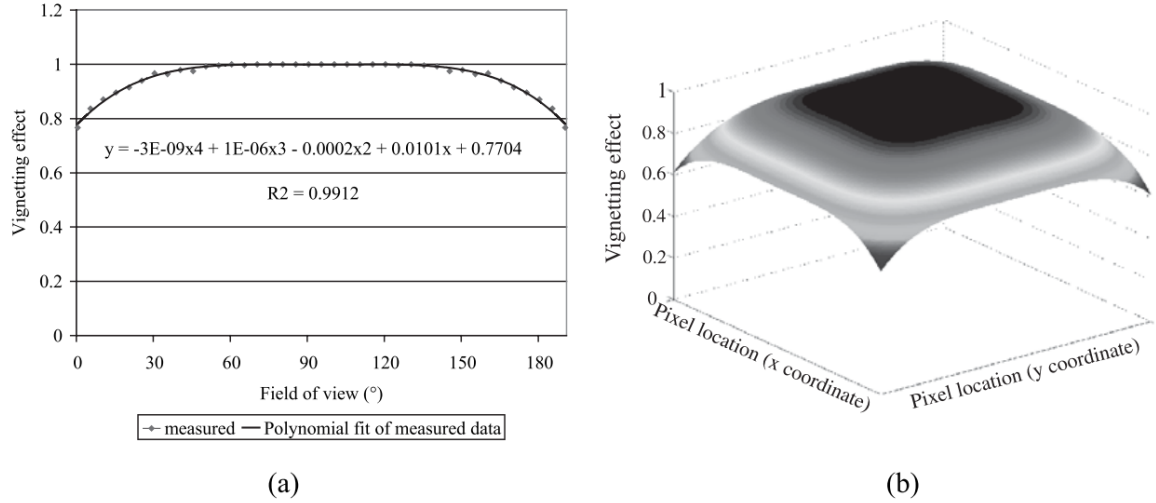


Figure 2.3 The vignetting function of Nikon FC9 fisheye lens.  
a) Measured data points and the vignetting function derived to fit the measured points;  
b) digital filter developed based on the vignetting function [27]

Geometric calibration is required depending on the cameras, as glare assessment tool such as evalglare, is only compatible with specific types of fisheye camera projection, such as equidistant and hemispherical fisheye projections [75]. However, except for some fisheye lens models commercially available in the market, most of the camera lenses does not strictly follow one of the compatible projections, or no information is given by the manufacturers (Figure 2.4). In such cases, projection of fisheye camera can be estimated by calibration. If the retrieved camera projection does not refer to any of the evalglare compatibles, the fisheye luminance maps can be transformed to match one of them prior to the glare assessment using the method introduced by [76]. There are number of methods proposed in the fisheye geometric calibration. Scaramuzza proposed a calibration method for omnidirectional camera models, which is implemented in MATLAB Computer Vision Toolbox [77,78]. A limitation of this method is that the method is validated within 150 degrees of FOV, not covering 180 degrees of human FOV. Kannala and Brandt proposed a generic camera model for conventional, wide-angle, and fisheye cameras [79]. Calibration of generic camera model is implemented in OpenCV library – an open source computer vision library works on C++ and Python language [79,80].

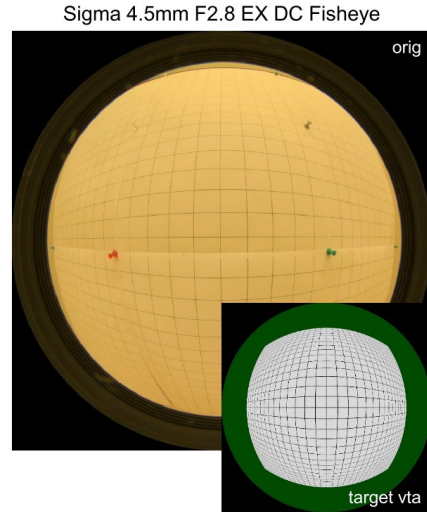


Figure 2.4 Sigma 4.5mm F2.8 fisheye projection and equidistant fisheye projection [76]

### 2.2.2 Relevant tools for the HDRI

Several tools exist for merging, calibration, and glare analysis of the HDR luminance maps. HDRgen is a command line software for estimation of camera response function (CRF) and HDR image merging [74]. Photosphere and hdrscope are user-friendly, graphical interfaced software for post-processing of raw HDR images, such as calibration or per-pixel luminance analysis (Figure 2.1 and Figure 2.5)[73,74]. Some of the RADIANCE commands, such as ‘pcomb’ can be used for vignetting correction and fisheye transformation using a specified radial function as an input [66].

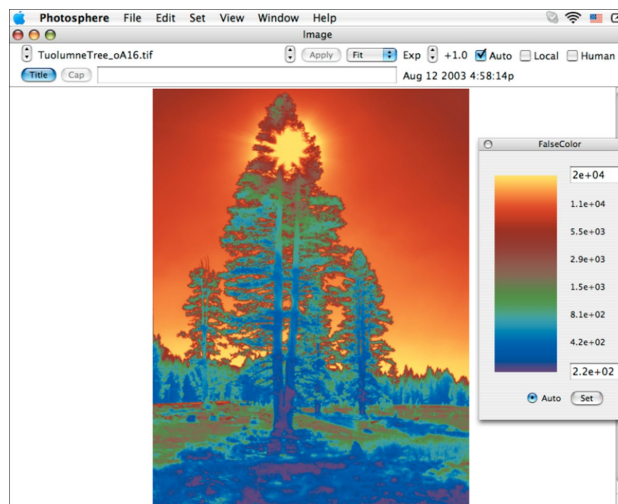


Figure 2.5 Photosphere software [74]



Evalglare developed by Wienold [65] is an open-source command-line tool for detailed per-pixel luminance analysis. In addition to the simpler form of glare metrics such as average luminance or luminance contrast between the specified task zone and the background, more complex glare metrics such as DGI or DGP can be calculated using Evalglare. Also, vertical illuminance can be calculated if the camera's hemispheric FOV is near 180 degrees. There are options for glare source detection rule: i) using an absolute luminance threshold, identifying pixels above the threshold as glare sources; and ii) using a multiplier with specified task zone, identifying pixels above the average task zone luminance times the multiplier as glare sources. Some of the studies used absolute luminance threshold [38,81], but majority of studies used the latter option [37,42,52,57,82,83].

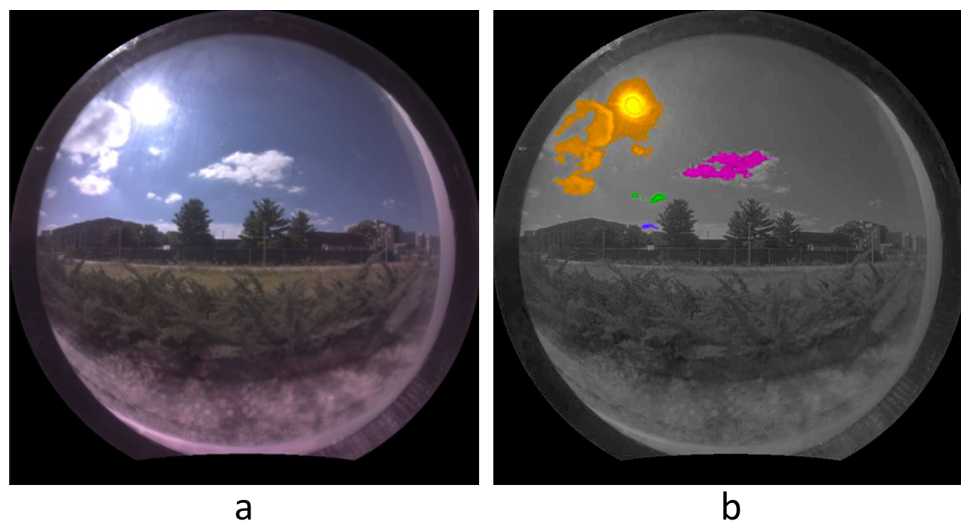


Figure 2.6 Evalglare glare detection. a) original HDR image; b) Evalglare check HDR image with color-mapped glare sources

### 2.2.3 HDRI application in daylighting research

#### *Visual comfort studies using HDRI*

HDRI was dominantly used as an assessment tool in visual comfort related studies. Researchers either attempted: i) to develop a new glare metric; or ii) to evaluate the existing glare metrics; or ii) to do both of the above. DGP is an example of glare metrics derived from an HDRI-

applied study [42]. Several follow-up researches on visual comfort that used HDRI are summarized as below:

Konstantzos et al. [37] performed an experimental and simulation study to evaluate DGP in an office equipped with roller shades. The author suggested a correction to the DGP equation to handle the case of sun in the field of view. Also, the result showed the DGPs is not a reliable metric when the sun is visible through the shades, suggesting the need for correction in such instances.

Later, the same authors performed a human experiment to evaluate the DGP in cases where the sun is visible through the roller shades [38]. 41 human subjects were test while performing office activities equipped with 14 shade products. From the statistical data analysis, discomfort glare thresholds are extracted for direction vertical illuminance (870 lx), total vertical illuminance (2,800lx) and DGP (0.4), while none of them were considered reliable as a sole discomfort predictor. Correlation of DGP with percentage discomfort of grouped people was lower than that of DGI ( $R_{DGP}^2=0.65$  and  $R_{DGI}^2=0.79$ ). As a correction to the original DGP, a new metric,  $DGP_{mod}$  was developed through optimization of exponential and coefficients which showed R-squared of 0.91 (Eq. 2.5).

$$DGP_{mod} = 8.40 \cdot 10^{-5} E_v + 11.97 \cdot 10^{-5} \log \left( 1 + \sum_{i=1}^n \frac{L_{s,i}^2 \omega_{s,i}}{E_v^{2.12} P_i^i} \right) + 0.16 \quad (2.5)$$

Hirning [57] performed a POE study in open plan offices in five green buildings in Brisbane, Australia. From a grouped analysis (similar to the [42]) of 491 responses from the employees, following observations were made. DGI shows higher correlation to the subjective glare assessment than the DGP ( $R_{DGP}^2=0.683$  and  $R_{DGI}^2=0.738$ ), partially explained by a low correlation of  $E_v$  ( $R_{E_v}^2=0.387$ ). The author suggests that this is possibly because of the difference of data distribution between where the experiments were performed. The maximum  $E_v$  recorded in Hirning's study was 2,354 lx, significantly lower than around 10,000 lx from the DGP investigation [42]. A new glare metric Unified Glare Probability (UGP) was proposed, to account for cases where the contrast effect dominates the glare probability, formulated as below:

$$UGP = 0.26 \log_{10} \frac{0.25}{L_b} \sum_{i=1}^n \frac{L_{s,i}^2 \omega_{s,i}}{P_i^2} \quad (2.6)$$

Suk et al. [39] performed a human subject study with 12 subjects who were tested different lighting conditions totaling more than 450 glare scenes in a day-lit office. DGP showed very high

accuracy rates for perceptible (90.6%) and disturbing (95.4) sensation of glare, while showing 54.5 % prediction accuracy for the entire glare sensation levels, which seems low but still higher than other glare metrics (CGI and DGI) compared.

Suk et al. [84] claimed that the existing glare metrics do not clarify the source of glare sensation, only representing the degree of visual discomfort. As an alternative, they proposed a new glare prediction method based on absolute glare factor (AGF) and relative glare factor (RGF), two major factors that cause glare. Understanding the dominant factor causing glare helps to better address in glary situation, the authors say.

Wymelenberg et al.[70] compared 150 visual comfort metrics to find the one with the highest classification rate between ‘preferred’ and ‘just disturbing’ condition. The most consistent and effective metrics were found to be the mean task zone luminance ( $adjr^2=0.59$ ), and DGP using 2,000  $cd/m^2$  as an absolute glare threshold ( $adjr^2=0.59$ ). Also, DGP consistently performed better DGI.

### ***Simulation studies using HDRI***

Several studies used HDRI in daylighting simulation. Majority of them utilized a technique name Image Based Lighting (IBL), which is “the process of illuminating scenes and objects with images of light from real world” (captured HDR images) [85]. All existing IBL studies are based on RADIANCE software [66]. The researchers simulated indoor scenes, using the HDR images taken from camera either installed indoor or exterior as lighting sources instead of using simplified sky models such as Perez All-Weather model [86]. As an HDR image captured in real-time includes much richer information - non-smooth sky luminance distribution or surroundings such as buildings or forestry [41] - as a luminous input compared to the generalized sky models with smooth luminance gradients, prediction accuracy can be significantly improved [87].



Figure 2.7 Rendered objects with different HDR images as a light source through IBL [85]

Inanici [88] examined IBL using an exterior camera to capture full exterior luminance map by comparing the prediction accuracy to a generalized sky model - CIE general sky model [89]. Validation under different sky conditions - cloudy, partly cloudy, mostly clear and clear – showed that the IBL-rendered luminance maps exhibits consistently lower errors compared to the generalized sky model-based ones.



Figure 2.8 Comparison of the HDR image of the sky, IBL simulation, and generalized sky modelled simulation under clear sky conditions [88]

Jones and Reinhart [87] compared glare measurements from actual HDR images and IBL-renderings under 240 clear and 38 cloudy sky conditions to evaluate accuracy of the glare

prediction. The author argued the generalized sky model, such as Perez all-weather model yields the correct total illuminance given the weather data, however, does not yield accurate sky luminance distribution, favoring of IBL-based simulation. As an input to the IBL, the authors tested two types of luminance map: i) environment map taken from camera mounted on window sill to capture view from window; and ii) sky map taken from roof to completely capture the sky dome. Although the Perez model showed the better prediction of interior measured values compared to the Sky-map, the environment map method showed faster simulation times and produced reasonably accurate results, while not requiring modelling efforts for outdoor surroundings.

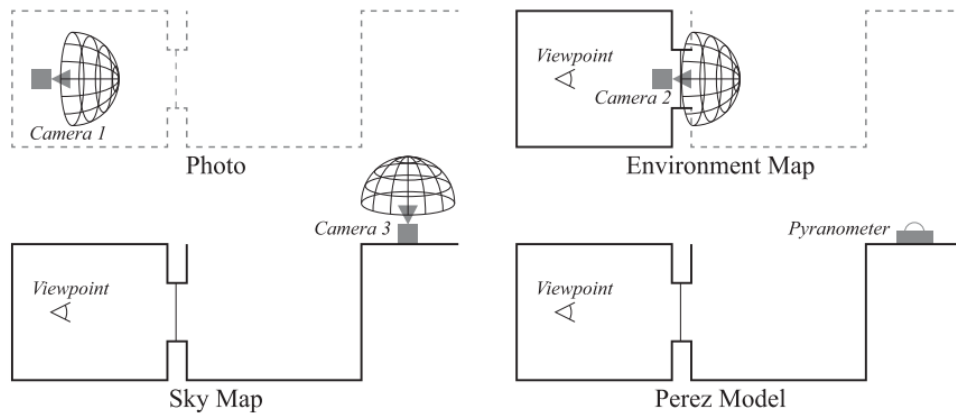
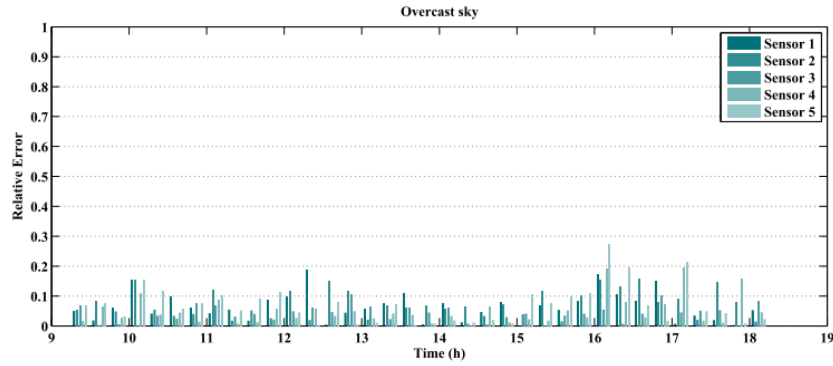
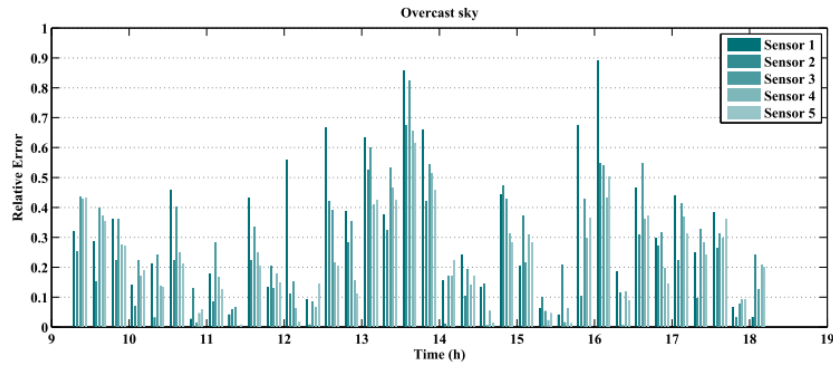


Figure 2.9 Experimental setup of cameras in [87]

Wu et al. [90] developed an embedded photometric device with a wide dynamic range (150 dB) for accurate, high-sky monitoring. The authors compared simulated horizontal work plane illuminance distribution from the sky map captured through device installed at window exterior and Perez all-weather sky model [86] under predominantly overcast sky condition. The average relative error to the photosensor-measured values were 4.1%-7.0% for IBL-method and 22%-32% for the Perez model, validating the authors' claim that IBL would perform better than the general sky models with over-simplification of the sky luminance distribution.



(a) HDR imaging approach



(b) Perez all-weather sky model

Figure 2.10 Relative error of the 5 computed work plane illuminances compared with lux-meter values for an overcast sky [90]

## 2.2.4 Daylight-linked control systems

Daylighting controls with shading systems considering visual comfort can be an effective solution to maximize the benefits from daylighting at its full potential. A number of observational field studies on occupant interaction with manual daylighting devices, found that the occupants are poor optimizers to those devices both in terms of energy saving and daylight provision. From those studies, it was repeatedly observed that the occupants tend to operate blinds only when disturbed by glare, and rarely modify the blind position (or slat angle) or operate artificial lights except for cases derived by seasonal changes [91–98]. This result favors the implementation of automatic DLCs since the occupants’ motivation for better visual comfort or daylight provision is not strong enough to drive frequent adjustments of manual daylighting systems. Therefore,

automatic daylight-linked controls considering visual comfort, have been extensively studied in the last couple of decades [23,37,99–106].

In this chapter, an overview of existing daylight-linked controls (DLC) including the state-of-the-arts is presented. Also, the literature on the occupant interactions to various DLCs are summarized.

## 2.2.5 Existing daylight-linked control algorithms

Typical form of the latest DLCs in the buildings are rule-based, deterministic algorithms is comprised of movable shading devices (either motorized blinds or roller shades) integrated with dimmable lights. Those systems are designed to block direct sunlight penetrating through window for glare mitigation –called as ‘cut-off’ strategy – and then adjust dimming level of the artificial light fixtures to maintain a target illuminance level on the work plane.

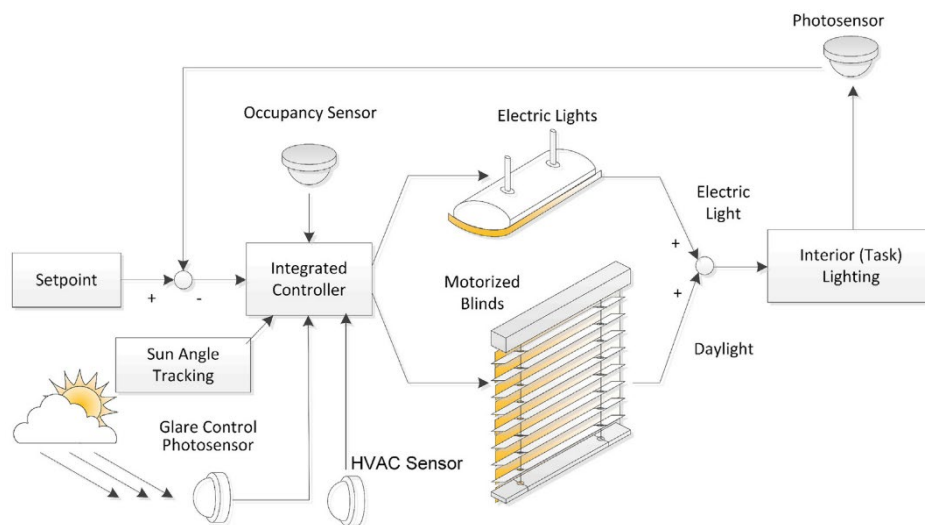


Figure 2.11 Integrated lighting and daylighting control [23]

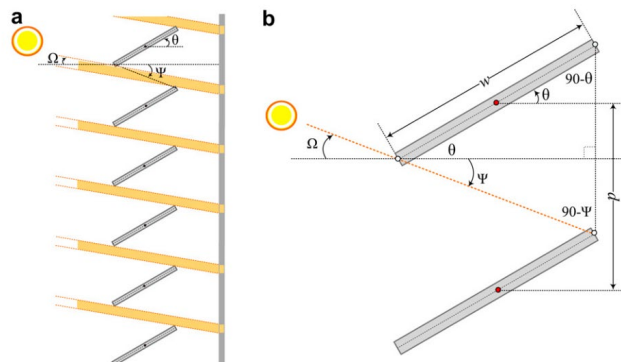


Figure 2.12 Cut-off strategy [101]

The shading operation is determined by varying logics but in common they adopt cut-off strategy based on geometric information such as shading system characteristics or room layout [99,101,107–110]. The simplest form of cut-off strategy is to block direct sunlight not to penetrate through the slats (Figure 2.12b)[101,111,112] for venetian blinds. More advanced ones allow intermediate slat angles to introduce more daylight within a specified distance from the window, called buffer zone [107]. Since slat angles made from those control algorithms may induce glare due to the specular, second-reflection from the bottom slats [102], some algorithms adopt sunlight re-direction strategy, that avoids the second reflection while being able to illuminate deeper areas [102,113] .

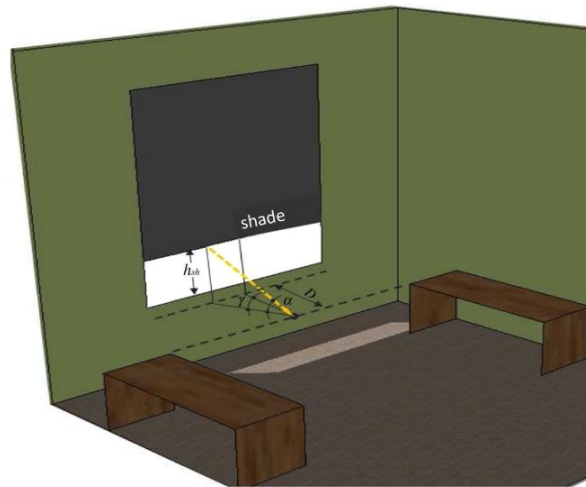


Figure 2.13 ‘Buffer zone’ concept: graph showing automated shading position to prevent direct sunlight falling on the work plane area at all times [114]

Often, vertical photosensorss or pyranometer mounted either interior or exterior of the window are needed for activation of rule-based operation of such systems [100,115–117]. Most commonly used variable for activation is global irradiance measured by vertically mounted pyranometer on the façade (Figure 2.14). The activation thresholds are normally determined based on empirical observations, for example by associating interior luminous condition to the selected variable. Yun et al. [118] introduces a simulation-based method to determine the appropriate activation threshold and blind slat angle based on several variables: climate condition, building



orientation, window-to-wall ratio (WWR), and control purpose (a weighting factor). The study result validates the need for commissioning of activation thresholds according to those variables, as suitable range of activation threshold varied across the different conditions.



Figure 2.14 Vertically mounted SPN1 pyranometer [110]

Horizontal illuminance on the work plane has used as a visual comfort constraint, although DPG and window illuminance have also been proposed and successfully implemented [101, 111]. The most widely used value is the minimum of 500 lx [99,110,112,116,118–121], while the maximum range varies across the studies. Since installing the photosensor on the work plane is impractical and disturbing, a ceiling mounted photosensor is installed alternatively, of which signal is converted into work plane illuminance. To develop methodologies for robust conversion between the ceiling photosensor readings and the work plane illuminance, extensive efforts have been made by researchers [122–127].

### **2.2.6 Current limitations of daylight-linked controls**

Despite the potential benefits of the automated DLCs, its wide application is yet to have come, according to [24]. In a survey targeted U.S facility managers where 78% of respondents comprised of commercial or institutional buildings, it was reported that only 35% of their facilities are equipped with daylighting controls [128]. In a literature review by [24], the author describes major barriers limiting the widespread of DLC are as follows: i) difficulties in design, installation and calibration; ii) limited modeling methods to quantify potential energy savings and economic benefits; and iii) occupant-tendency to prefer manual operation of lighting/window systems. To paraphrase, to widely adopt DLC in commercial buildings, their designing and installing procedure

need to be streamlined and efficient, relevant performance assessment tools need to be developed, and manual override is recommended as an extra feature for the automated DLCs (or, even better, occupant preferences need to be integrated into automated control logics [129]).

In addition to the measures for the wide-adoption of automated DLC mentioned above, there exists need for work to enhance the performance and robustness of the DLC, particularly related to visual comfort in occupant-centered aspects. Even the most advanced forms of DLCs – including MBCs or occupant-preference based controls – frequently fail to deliver comfort to occupants or provide over-protection from glare compromising the daylight provision. The reasons for failing vary across the controls and studies, however, can be generalized as described below.

Existing DLCs rely on vertical irradiance/illuminance either transmitted to identify or measure the exterior luminous condition. Those values are used to detect the presence of the sun, or to estimate cloud coverage or overall brightness of the exterior scene, which is used for activation of rule-based control logics or detailed daylight simulation. Even those indices can serve as good indicators of the overall luminous condition of the exterior scene, yet cannot provide rich information such as luminance ratio or distribution, which also affects human glare perception. Thus, cases such as in presence of small but extreme glare sources outside (for example exterior reflections by adjacent building facades), existing DLCs fail to identify uncomfortable situation since small sources of extreme luminance do not always contribute to vertical illuminance beyond the suggested limits for discomfort glare [23].

Also, solar-tracking often depends on sun position calculation algorithm without real measurement[101,105], or estimated with empirically determined vertical irradiance/illuminance thresholds in specific geographic location [100,111,116–118,130], thus are not guaranteed to work properly in different buildings. As presented in [118], activation thresholds for shading systems are not consistent across the studies, implying a single activation threshold may not be adequate to be generalize.

There are two major drawbacks of DLCs using work plane illuminance as a comfort criterion: i) calibration of photosensor signal, though can be generalized via aggressive calibration covering various factors – such as geographic locations, seasonal variation, and room characteristics – may not guarantee year-long robustness of the DLCs; and ii) the correlation between the horizontal work plane illuminance and the visual comfort is often insignificant. The reason for the popularity of illuminance-metrics for DLCs is mainly due to their predominance in

professional standards [49] for simplicity in measurement. However, Konstantzos [37] observed a poor correlation between the DGP and horizontal work plane illuminance, except for cases measured with roller shade with perfectly diffusive fabric. In a POE study of visual comfort in side-lit open offices in San Francisco performed by Konis [21], horizontal illuminance based metrics were found to be the least accurate predictors among 15 visual comfort metrics compared. Wymelenberg and Inanici [15] performed a 6-month-long human factors study with 48 participants in an office-like laboratory. They evaluated correlation of 14 visual comfort metrics with subjective assessment of luminous conditions from responses totaling 1488. The horizontal desktop illuminance only showed adjusted  $R^2$  of 0.09 for overall visual comfort, significantly lower than the vertical illuminance at eye ( $adjR^2=0.298$ ). Also, Xiong and Tzempelikos [110] found that a model-based control based on work plane illuminance often resulted in higher shade positions with potential risk of glare.

### **2.2.7 Studies on visual comfort oriented DLCs**

Only a few studies on visual comfort oriented DLCs exist. Those control algorithms are advanced in that they are operated based on visual comfort metric with higher correlation to human perception than the existing simple illuminance metrics. Since those metrics are difficult to measure by simply placing the sensor at the position of interest, researchers utilized daylighting models (MBC), either in simple or sophisticated form, to calculate them.

Chan and Tzempelikos [102] evaluated four types of control strategies – a cut-off angle control, a daylighting-redirecting control, and two glare protection control modes, using a hybrid ray-tracing and radiosity daylighting model [131] developed by the same authors. One of the glare protection control was a model-based control (MBC) that is aimed to maintain DGP below 0.35. The other, ‘simplified’ control uses pre-calculated correlations between DGP and transmitted illuminance to establish binary setpoints for model-predictive controls (MPC). Both glare protection strategies were proven to be efficient both in terms of daylight autonomy and glare risk mitigation.

Xiong and Tzempelikos [110] implemented the MBC in real office-like laboratory. The MBC calculates real-time interior lighting conditions, lighting energy use and DGP for predetermined shade positions with 10% increments at each control step, based on readings of two

vertically mount sensors (for solar radiation and illuminance) on the building façade. The control selects the highest shade position that meets any of three visual comfort criteria – DGP, vertical illuminance, and work plane illuminance. The experimental implementation of the model-based control algorithms showed that DGP did not exceed 0.35 for most cases while maintaining work plane illuminance levels, and lighting energy use was significantly reduced with all MBC strategies.

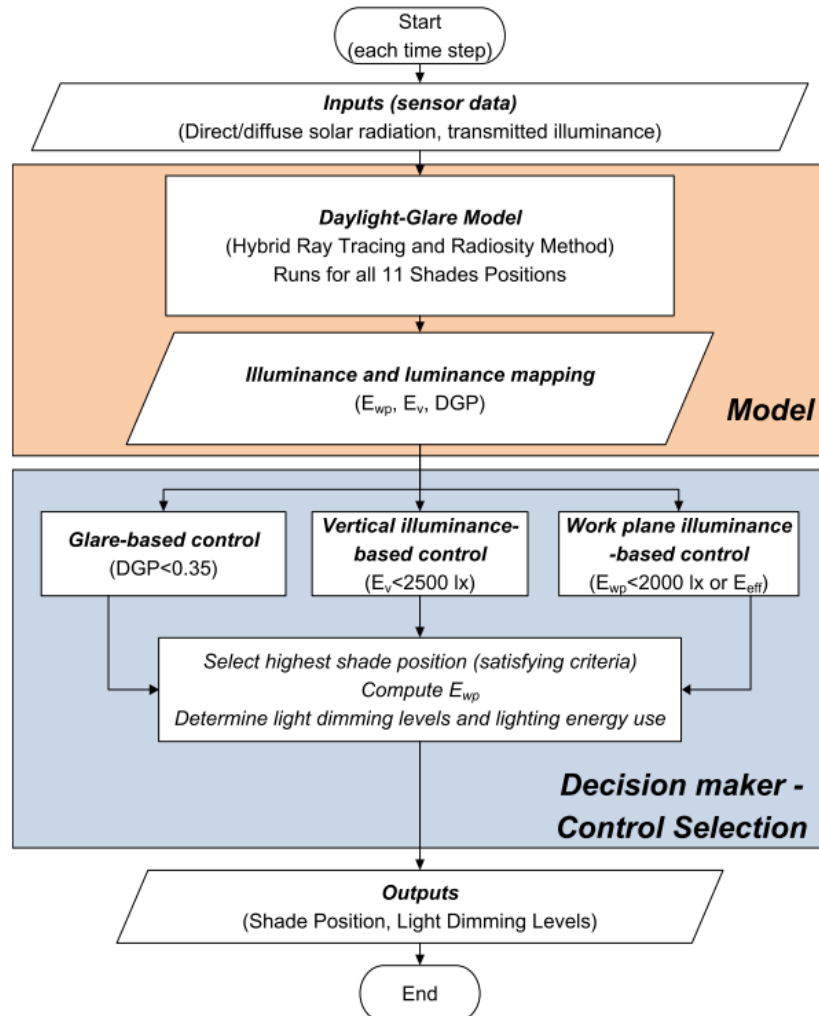


Figure 2.15 Flowchart of MBC developed by Xiong and Tzempelikos [110]

Iwata et al. [113] conducted a simulation study for controlling an automated daylighting control algorithms with venetian blinds and dimmable lights. The proposed algorithm aimed to prevent glare and reduce lighting energy use, similar to comfort-oriented MBCs. A new metric,

the Predicted Glare Sensation Vote (PGSV), is introduced, that includes the average luminance of the fixed window area (Eq. 2.6):

$$\text{PGSV} = \log \left( L_s^{3.2} \omega^{-0.64} / L_b^{0.61 - 0.79 \log \omega} \right) - 8.2 \quad (2.6)$$

where  $L_s$  is glare source luminance,  $L_b$  is background luminance, and  $\omega$  is solid angle of the glare source. Dimming control was based on rooftop photosensors, targeting ambient illuminance of 300 lx. The glare prevention control results in more conservative blind slat angles compared to the time- dependent cut-off angles, while reducing the lighting energy use by 30% in typical open plan offices in Tokyo, Japan.

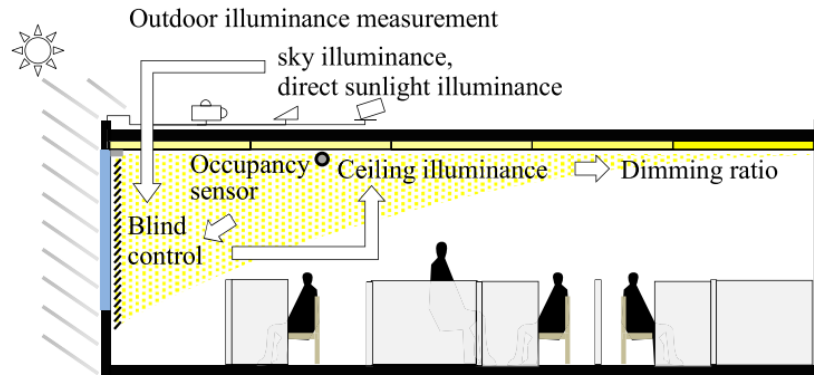


Figure 2.16 Outline of DLC proposed by Iwata et al. [132]

Shen and Tzempelikos [100] proposed simplified MBC shading control algorithm, based on the ‘effective transmitted illuminance’ concept. This algorithm moves shade to intermediate positions to maximize daylight provision while avoiding excessive work plane illuminance – 2,000 lx - to prevent glare. This approach is inherently associated with shade property and room characteristics, since control operation varies depending on the shade optical properties, façade orientation, and window geometry. The proposed algorithm performed well both in experimental settings and through the annual simulation results, despite the over-simplification of glare metric can be an issue in some cases.

In addition to above studies, several comfort-based daylighting controls are based on low-cost camera sensors. Those controls used cameras to capture luminous indices that cannot be done by existing sensors, such as photosensors – in most cases –, or pyranometers. Details of those studies are elaborated in Section 2.3.2.

## **2.3 Low-cost camera sensor-based daylighting controls**

Image-based sensing technologies, such as object detection or classification from the images or video have experienced a quantum leap over the past decades, thanks to improved computing power and machine learning algorithms, particularly deep neural networks (DNN). Such technologies are omnipresent in our everyday life and are being the most active research topics of this era.

Despite the obvious potential of image-based sensing for daylighting controls - in a sense that both are closely related to the ‘human vision’ -, researches on those topics have not burgeoned yet. To elaborate, HDRI luminance measurements, although mature, have been utilized for evaluation purposes, rather for sensing in real buildings. To justify the phenomenon, however, it is because the low-cost, programmable HDRI sensors only recently became available in the market. The following sections present an overview of low-cost camera sensors used in the relevant studies and present recent attempts to use them for smart daylighting controls.

### **2.3.1 Low-cost camera sensor**

Low-cost, programmable camera sensors with a small form factor have become more available thanks to the recent improvement in integrated circuits (IC) and embedded systems. This change drives researchers not limit the HDRI usage for evaluation purpose, but to expand it for various purposes, such as smart sensing for high performance, robust daylighting controls.

A few existing studies present custom-developed camera sensors for daylighting controls that can be categorized into two forms: i) a custom designed, embedded photometric device where the camera and the computation module (microcontroller) are integrated as a single device [48,90]; and ii) a general purpose single-board computer connected with compatible camera board [44,46,47,133–136].

In case of the former, a single device processes the entire pipeline for the luminance measurement including the HDR imaging or image calibration. The advantages of using this type of sensor is that the imaging module is highly customizable and allows standalone operation with a smaller form factor than the latter type. For example, an embedded photometric device developed by Wu et al. [90] have wide dynamic range of 150 dB, which can hardly achieved from cheap image sensors available in the market. Also, the configuration for imaging can be fine-tuned for

specific purposes with higher degrees of freedom compared to the complete camera module products. Figure 2.17 presents an example of custom-designed embedded device used in [48].



Figure 2.17 IcyCAM HDR vision sensor equipped with fisheye lens [48]

Despite the advantages of custom-designed sensors, development of such devices has logistical barriers to daylighting researchers. A combination of readily available products – a general purpose single board computer and a camera board – can suit its purpose. The most popular single board computers, such as the Raspberry Pi series [137] are designed for education purpose in developing countries, but have become a widely used research tool in various types of studies. This \$35 computer feature a Broadcom system-on-chip (SOC) with an integrated ARM-compatible central processing unit (CPU) and on-chip graphics processing unit (GPU). Processor speed ranges from 700 MHz to 1.5GHz and memory ranges from 234Mb to 8Gb. Raspberry Pi can be operated either Linux or Windows-like operating system, and allows seamless integration to compatible modules, including the proprietary Pi Camera board or other Universal Serial Board (USB) camera boards. Such module offers programming capability via various programming languages, such as C++ or Python. The latest version of Pi Camera (V2.1) based on Sony IMX219 image sensor offers maximum resolution of 8 megapixels for still photographs with a 62.2 degrees (horizontal)  $\times$  41.41 degrees (vertical). Also, its image shooting parameters such as ISO, shutter speed, white balance, or resolution can be precisely controlled through a Python Picamera library [138]. Finally, its operation can be fully automated and scheduled - such as taking LDR images with predefined multi-exposures, for HDR image creation at designated time steps for sensing and control.

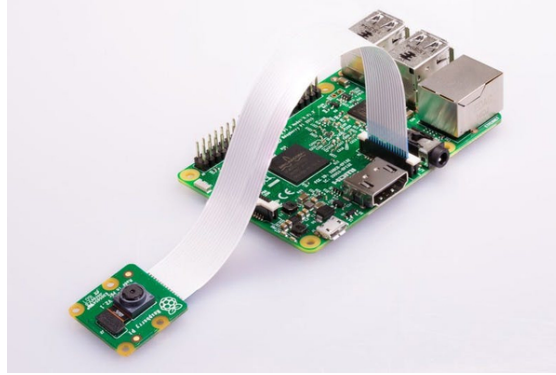


Figure 2.18 Pi Camera & Raspberry Pi 3B+ [137]

### 2.3.2 Camera sensor-based daylighting control studies

A handful of studies attempted to utilize the HDRI sensor for luminance-map-based lighting control in buildings. Sarkar & Mistrick [46] utilized an image sensor to estimate horizontal illuminance from the measured HDR luminance map to control luminaires to achieve target illuminance level on the work plane. Mardaljevic et al. [139] attempted to use HDRI sensor to quantify cumulative daylight exposure in a exposure/conservation setting in a museum buildings. The method was validated both under both controlled and in-situ conditions, but required meticulous pre-measurement of surface characteristics for its success. Goovaerts et al. [44] tested a low-cost camera-based shading control that avoids visual discomfort in a mock-up office environment, using DGP as a control variable. The occupant feedback showed that the proposed approach can better perform when the override is allowed, which makes the specific system rather limited. Motamed et al. [48] tested a lighting controller using a similar method to estimate work plane illuminance by installing the HDRI sensor on the ceiling. In addition to the horizontal illuminance, they also used DGP - measured by another HDRI sensor adjacent to the occupants - as a control parameter to optimize the electric lighting and shading operation. The proposed controller required two HDRI sensors (on ceiling and adjacent to the occupant) per occupant and also required commissioning to find the correlation between measured luminance and horizontal illuminance on the work plane, compromising the feasibility of the system.

Nonetheless, none of the referred studies yet achieved the full potential of the luminance-based lighting control system, which is operated based on the occupant-perceived luminance distribution. Apart from the computation cost and compactness factor, it is ideal for such advanced



lighting control systems to capture as much detailed information the corresponds to the occupants' FOV for sophisticated, human-centered control algorithms. Motamed et al. [140] performed a sensitivity analysis of several visual comfort metrics –average luminance, direct illuminance from glare sources, DGP and DGI – in respect to translation and rotation of the measuring HDRI sensor adjacent to the occupant position. It was observed that the DGP is less sensitive to the position variation compared to the other metrics, while showing smaller sensitivity to translation than the rotation. The maximum relative error of  $\pm 32\%$  was recorded from camera translation and rotation of  $\pm 30\text{cm}$  and  $\pm 30$  degrees. This result confirms the importance of aligning occupant and camera FOV for accurate visual comfort prediction.

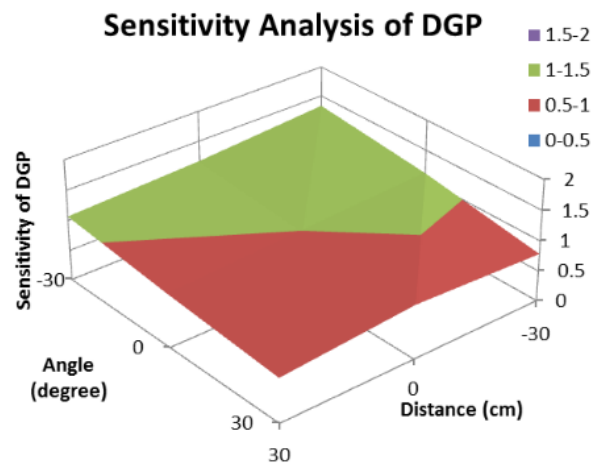


Figure 2.19 Sensitivity analysis of DGP with respect to translational and angular displacement [140]

However, installing HDRI sensors to positions to closely match occupant-views is practically challenging – the HDRI sensor is needed per each occupant and the sensor installation near the occupants will be distracting. To avoid such distraction, the HDRI sensor was installed at less-intrusive positions in the related studies – that performed a long-term assessment of human visual perception or implemented luminance-map-based lighting control systems. The alternative positions include ceiling [47,48,136,141], screen or partition [21,140,142], or the others including the occupant-vicinity [44,48,143].

Kruisselbrink [47] claimed that the ceiling-based camera sensor is the most suitable option for open-plan offices the most common configuration for office layouts since the position allows non-obtrusive, multi-region measurement. The author also examined the feasibility of using

ceiling-based camera measurement as a proxy for luminance distribution perceived by an occupant, by extracting per-pixel luminance value within mask areas corresponding to four different regions of interest seen from the occupant-view. A simple linear regression was tested for estimation of occupant-perceived average luminance within the ROIs, and the method demonstrated a reasonable accuracy when accounting for the uncertainty. However, two critical shortcomings are observed. First, the correlation between the masked regions had an inverse relationship with their sizes. This is mainly because the discrepancy between the camera and user-perceived scene under the mask becomes greater as the size of ROI grows. The fundamental reason for the discrepancy is the lacking 3D context in camera-to-occupant correspondence. Another limitation is that the proposed method requires manual commissioning – masking of corresponding ROIs and model-fitting for average luminance estimation that requires installing of the camera at occupant-position and collecting luminance maps through it. Manual commissioning is necessary for such types of methods since the correlation between camera and occupant-views largely depends on the configuration of the room including the room layout, surface properties, and the camera position.

In this regard, the scope of this dissertation includes development of a novel, non-intrusive luminance-monitoring sensing framework that resolves the aforementioned issues – lacking 3D-context and necessity of high-degree commissioning - deploying advanced photogrammetry techniques.

## **2.4 Photogrammetry for 3D building interior reconstruction**

### **2.4.1 Photogrammetry**

Photogrammetry is a broad term for technologies primarily concerned with making precise measurements of 3D objects from 2D images, using a camera as a measuring instrument [144]. Its wide-application includes precise 3D measurement of the real-world objects, generation of topographic maps, and the reconstruction of 3D point clouds for surface reconstruction, and others.

### **2.4.2 Structure-from-Motion – Multiview Stereo pipeline**

In the last decade, the coupling of photogrammetric principles with modern computer vision concepts and algorithms revolutionized 3D point cloud reconstruction – specifically

Structure-from-Motion (SfM) - Multiview Stereo (MVS) photogrammetry [145]. SfM-MVS is a general workflow for the image-based 3D point cloud reconstruction of objects comprised of two separate, sequentially-connected algorithms - Structure-from-Motion and Multi-View-Stereo - complement to each other. Structure-from-Motion (SfM) is the process of reconstructing 3D structure from its projections into a set of unstructured images taken from different viewpoints [146]. Different from traditional, beforehand photogrammetric approaches, SfM automatically estimates and refines the intrinsic parameters and poses of the cameras, thus no prior knowledge of the camera is required. SfM algorithms only reconstruct 3D points with strong saliency across the images, such as Scale-Invariant Feature Transform (SIFT) key-points from the images [147], which are far less than the number of pixels per image. For the more detailed 3D representation of the real-world scene, the sparse point cloud reconstructed via SfM algorithm is subsequently densified through an MVS algorithm. MVS leverages the estimated camera parameters from the SfM to solve stereo-matching between smaller subsets of images based on the photometric and geometric constraints. One of the common advantages of open-and-commercially available SfM-MVS pipelines is that the whole reconstruction can be highly automated except for capturing video or image sequences. More importantly, the method does not require any expensive measuring device or calibration procedure, such as for Structured-Light or LiDAR technologies: all consumer-grade digital camera, including the smartphone can be utilized [148].

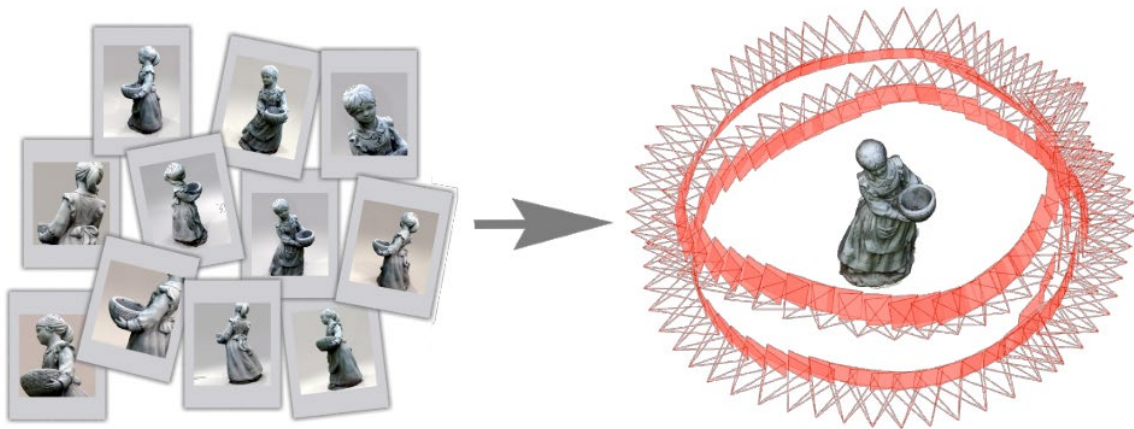


Figure 2.20 3D reconstruction using SfM-MVS pipeline [149]

### **2.4.3 Application of 3D reconstruction in building research**

Diverse applications of 3D-reconstructed as-built building interior models are active topics in the building-research domain, particularly in the field of Building Information Modeling (BIM). Scan-to-BIM is one of those, which refers to systematic approaches to create a semantically rich, as-built BIM models from reconstructed 3D point clouds. The related research topics include building component detection and segmentation from the 3D point cloud, automatic CAD drawings creation, measurement-aided tracking of construction progress, etc. [150–152]. However, the use of automatic 3D reconstruction for smart sensing and lighting control has not been investigated so far, to the best of our knowledge. This thesis is thereby the first attempt to investigate the potential of using advanced photogrammetry coupled with computer vision techniques for remote, non-intrusive luminance monitoring in building indoor environments.

## **2.5 Research gaps and aims of the thesis**

Despite the obvious benefits of human-centered daylighting control in buildings, current technologies have not achieved their fullest potential. Existing DLCs, even at its most advanced form such as MBC or MPC fail to optimize the balance between visual comfort and daylight provision. Such limitation is mainly due to fundamental inability of photosensors - predominantly used in daylighting system – to measure critical indices to human visual comfort, such as luminance distribution.

Photosensors in DLCs are typically used to monitor i) exterior weather condition and ii) indoor luminous condition. A major issue of photosensor-based weather monitoring is that such systems highly depend on site-specific commissioning. Such systems cannot be universally applied to buildings in different locations unless we choose a conservative threshold as a safety factor. Consequently, shading systems will often false-detect risk of glare, compromising daylight provision. Also, since photosensors can only quantify the overall brightness of a hemispheric visual field, they fail to identify a certain type of glare sources: small but extremely bright sources – such as façade reflection from adjacent buildings, frequently observed in dense urban environments.

As explained in Chapter 2.2.4, the dominant form of indoor brightness monitoring system adopts ceiling-mounted photosensor to maintain horizontal illuminance of (usually) 500 lux. The

drawbacks of such systems are i) commissioning issue similar to the weather monitoring (paragraph above); and ii) low prediction performance of horizontal illuminance as a visual comfort indicator. Due to the general agreement on luminance-metrics as a better visual comfort predictor than the illuminance, a few researchers pioneered visual comfort-oriented controls based on luminance-based metrics. Such studies adopted low-cost, programmable camera sensors to monitor the occupant-perceived luminance within the FOV through HDRI technique. However, instrumental settings in such studies are not feasible and robust enough to be widely adopted throughout the buildings in terms of sensor placement (elaborated in Chapter 5.1).

Also, despite the obvious advantages of camera as building lighting sensors or visual comfort assessment tool, construction and calibration of such sensors remain as a barrier to the researchers relatively new in this domain, requiring them extra effort to put on. Even through existing studies well-established the whole calibration procedure and provide software packages for calibration, visualization and various processing of HDR luminance maps, there is no open packages focusing on the operation of the hardware-side. As described in section 2.3.1, some studies opted to build a customized standalone HDRI sensor to suit their purposes which yields logistical difficulty for typical building researchers. For this reason, the majority of researchers choose another option of assembling the market-available products to constitute their own sensors. Raspberry Pi and its camera module have gained their popularity over their competitors, thanks to the supporting community and Python compatibility, however, they still lack software support for their initial build-up and calibration procedure.

Based on the above, the detailed aims of the thesis are:

1. To establish a procedure of building and calibrating a sensor that captures accurate HDR luminance map, composed of cheap, market-available camera and single-board computer.
2. To develop a new daylighting control framework based on a window-mounted HDRI sensor, that identifies potential glare sources in real time, enables solar tracking, and provides adequate protection to the occupants. The shade control logics included in the framework are based on the glare source and solar disk detection through the HDRI sensor and will perform as an additional layer of protection for glare mitigation.
3. To develop a fisheye-stereovision HDRI sensor to solve the limitations of HDRI sensor comprise of monovision camera – luminous overflow and positioning ambiguity- for exterior luminance monitoring. This new sensor allows accurate 3D positioning of detected glare

sources and capturing accurate luminance map without overflowed pixels, enabling the new sensor to fully replace the existing photosensors with better capabilities.

4. To develop a semi-automated method for monitoring occupant-perceived luminance distribution within the visual field, leveraging the HDRI and computer vision techniques. This method requires minimal commissioning effort and device requirement to establish indoor luminance monitoring system with reasonable accuracy without causing distraction to the occupants.

### **3. REAL-TIME DAYLIGHT GLARE CONTROL USING A LOW-COST, WINDOW-MOUNTED HDRI SENSOR**

#### **3.1 Scope and objectives of the study**

This paper proposes a different daylight glare control framework, in which a low-cost programmable HDRI sensor with a wide fisheye lens is attached on the inside surface of the glazing to capture the full luminance distribution of the exterior scene. With proper calibration, the sensor can accurately measure the luminance, size, and position of any potential glare sources using per pixel analysis. At the same time, the sensor can explicitly detect the presence of the sun or any bright source of small size but intense luminance (i.e., reflected glare), and track such sources without commissioning, therefore providing real-time additional glare protection to any type of daylighting controls. This could prevent control strategies from underestimating the risk of glare and also avoiding over-conservative shading operation.

Section 3.2 presents the details of the low-cost image sensor. The photometric and geometric calibration of the camera for HDR luminance map acquisition and processing are described in Section 3.3, together with the real-time solar tracking, glare detection method and an efficient glare source positioning algorithm. Section 3.4 discusses the algorithm of practical glare control with the window-mounted camera. Finally, the controller was implemented in a private office to demonstrate the advantages of the developed camera-based glare control compared to simple existing controls (Section 3.5).

#### **3.2 Low-cost image sensor**

General-purpose single-board computers, such as Raspberry Pi 3 B+ (Raspi) used in this study, have gained popularity over the past few years due to their very low price, small form factor and suitability for different problems through both external hardware using GPIO pins or through software using custom scripts [137]. Raspi in the present study runs with a UNIX-based operating system that can run Python scripts created to handle every aspect of the methodology.

To serve the purpose of a low-cost HDRI sensor, Raspberry Pi Camera Module V2, a proprietary camera-on-board compatible with the Raspi is used. The camera is based on the CMOS sensor (Sony IMX219) with a maximum dynamic range of 44.56 dB, offering a resolution of 8

megapixels (3280×2384 pixels) for still images. An open-source Python package named PiCamera provides an easy-interface to alter the image-shooting parameters (shutter speed, ISO, white balance, resolution, rotation) and operate the camera through Python scripts.

In its standard configuration in the market, the camera is equipped with a fixed-focus 3.4mm lens, allowing a rectangular FOV of 62.2 degrees (horizontal) × 48.8 degrees (vertical). However, as the objective of the study required wider FOV to capture the full exterior scene from the window, the original lens was replaced by an M12 fisheye lens, with an aperture of f/1.8 and a focal length of 1.05 mm [153]. The expanded FOV of the fisheye image sensor is 180 degrees (horizontal and vertical), covering the maximum possible area of the exterior scene. In order to perfectly fit the lens to the image sensor with minimum light leakage, a custom camera-lens mount was designed and 3D-printed (Figure 3.1). 3D printing was also used to mount the complete HDRI sensor on the window or tripods during calibration stages.

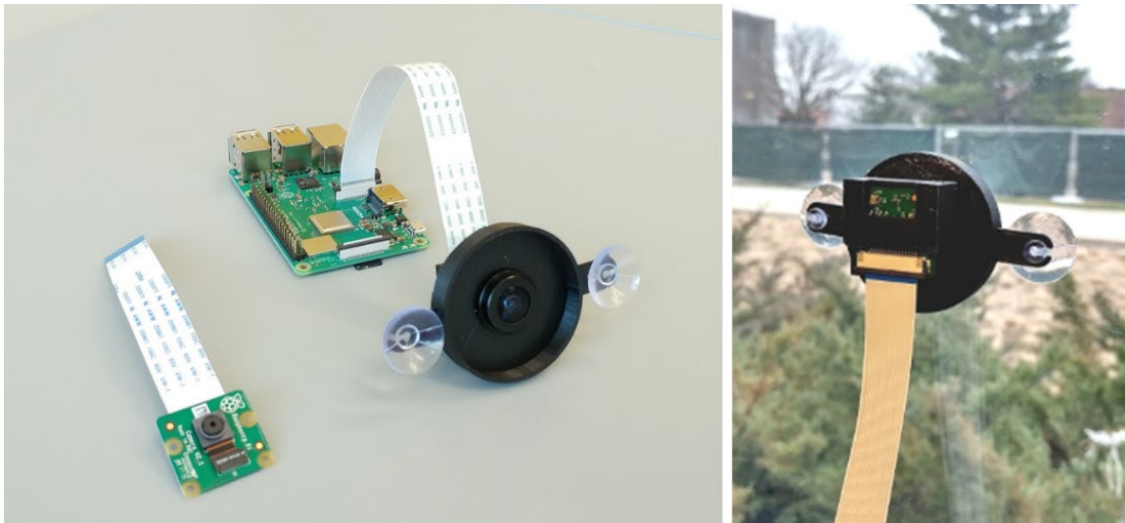


Figure 3.1 Original image sensor and HDRI sensor with lens connected to Raspberry Pi (left); HDRI sensor attached to window using a 3D printed mount (right)

### 3.3 Glare source detection and positioning for glare control

#### 3.3.1 Overall Process

The overall process of glare detection using the new sensor consists of two stages –HDR luminance map acquisition and glare source identification (Figure 3.2). Photometric and geometric



sensor calibration precedes this process. Photometric calibration is a necessary step to acquire reliable luminance values from images taken by the sensor, and includes the estimation of the camera response function (CRF) followed by a vignetting correction. These concepts and corrections are discussed in detail in Section 3.3.2. HDRI Photometric and Geometric calibration. Geometric calibration is a process to obtain camera intrinsic parameters and distortion function that is used to back-project image pixels into 3D coordinates. Once all calibration steps are finished, a complete luminance map of the camera’s FOV can be created from multiple images with different exposures by a sequence of processing. The final luminance map in this study is processed by Evalglare [65] – an open-source software for glare analysis used also to identify potential glare sources. Finally, the lowest profile angle (the projection of the angle between the light rays originating from the source and the normal to the window) is computed using an efficient positioning algorithm. The following sections present details for each step.

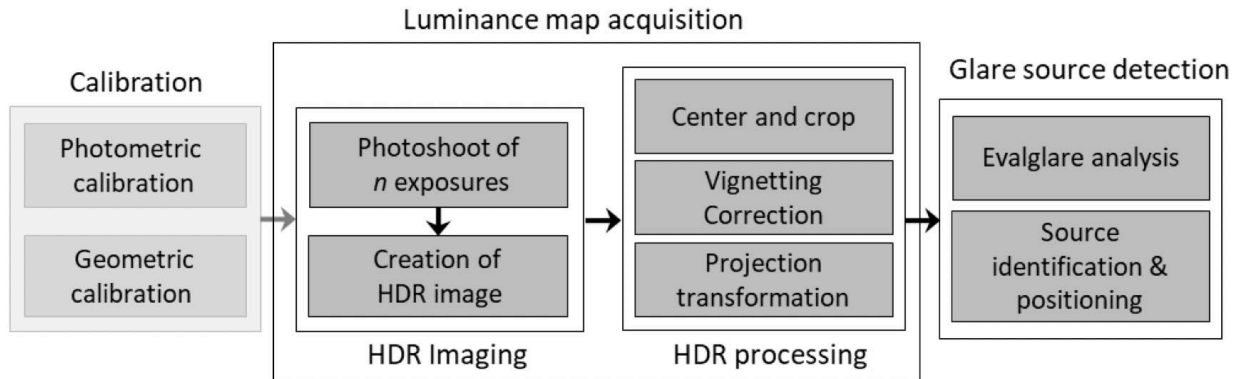


Figure 3.2 Overall process for HDRI and glare detection

### 3.3.2 HDRI Photometric and Geometric calibration

The HDRI methodology consists of the following steps: a series of photographs with different exposures is captured at any given timestamp; then, these are combined into an HDR image using a previously extracted calibration function; in the end, necessary corrections are performed towards producing a reliable luminance map. A Python script was created to schedule the camera to capture a full set of exposures at a given time interval, with shutter speed ranging from 28 to 7800 microseconds with approximately 9 stops. Table 3.1 lists the camera settings. Then, the low dynamic images were combined using the open-source command-line software

HDRgen [74], applying a camera response curve retrieved from photometric calibration. The camera response curve is the key component of HDR imaging, which refers to a non-linear curve function associating radiometric intensity to absolute values of luminance. It is obtained using a calibration procedure that corrects the luminance value from a non-calibrated HDR image, at a given point of near-neutral spectral characteristics, with the value obtained by a calibrated luminance spot meter, and applies the correction factor to all the pixels of the image. The retrieval of the response curve allows to convert the RGB pixel intensity to a linear function of luminance in the scene and photometrically combine images with different exposures. The final step of ensuring photometric accuracy of HDR luminance maps is correcting the vignetting effect, which refers to a radial decrease of luminance observed in fisheye lenses with fast apertures (low F-values). The process presented by Inanici [27] was performed to obtain a 5<sup>th</sup>-degree polynomial correction function, which was then applied to all HDR images through the use of RADIANCE [66]. To estimate the luminance range of the HDRI sensor, a method introduced by Pierson et al. [33] was used. By capturing a solar-disk-centered HDR luminance map (to avoid vignetting) and finding the maximum luminance value from overflowed pixels, the measuring capacity of 420,000 cd/m<sup>2</sup> was retrieved. Completing the photometric calibration procedure ensured accurate luminance maps from the resulting images. However, since detailed information of the position and size of glare sources is also important, given the specific objectives of this application, the images needed to be additionally geometrically corrected.

Table 3.1 Camera settings for HDR image creation

ISO	100
Number of exposures	9
Shutter speed (microseconds)	28, 47, 85, 198, 482, 992, 1994, 3885, 7798
Resolution (pixels)	Original LDR image: (1093, 821) Cropped image with fisheye circle: (602, 602)

Geometric calibration is a process that estimates the intrinsic camera parameters and distortion of a camera and determines the mapping of real-world scenes into image pixels. After a

proper geometric calibration, it is possible to retrieve the real-world position (as a 3D ray vector with two degrees of freedom) of an image pixel relative to the camera through back-projection. Also, the obtained distortion function can be used in the transformation of fisheye projection. Transforming the fisheye projection to standard forms, such as equidistant or equisolid projection is very useful since it reduces computational cost. Moreover, the up-to-date version of Evalglare is only compatible with certain projections such as equidistant, making geometric calibration a necessary task.

There are different distortion models for fisheye cameras that are mostly based on radial distortion, a function of pixel radius from the distortion center. Just recently, Wagdy et al. [34] developed a parametric method and a tool for remapping and calibrating fisheye images for glare analysis. In our study, a distortion model for omnidirectional cameras proposed by Scaramuzza et al. [77] was used. The model estimates the 3D directional vector emanating from the viewpoint as a function of pixel radius from the distortion center, as described in Eq. (3.1):

$$\begin{bmatrix} X_c \\ Y_c \\ Z_c \end{bmatrix} = \lambda \begin{bmatrix} u \\ v \\ f(\rho) = a_0 + a_2\rho^2 + a_3\rho^3 + a_4\rho^4 \end{bmatrix} \quad (3.1)$$

where  $[X_c, Y_c, Z_c]^T$  is the vector representing a ray that passes through the real-world scene in camera coordinates,  $u$  and  $v$  are pixel distances from the distortion center in  $X$  and  $Y$  axis respectively,  $\lambda$  is a scalar factor,  $\rho$  is the pixel radius from the distortion center ( $\rho = \sqrt{u^2 + v^2}$ ), and  $[a_0, a_2, a_3, a_4]$  are coefficients for the  $Z$ -coordinate retrieval (Figure 3.3). In the present study, the fisheye camera calibration function in MATLAB computer vision system toolbox was used. A set of photographs of a checkerboard pattern captured in different views is the input to the toolbox. The major outputs of interest from the calibration are the coefficients of function  $f$  in Eq. (3.1) and pixel coordinates of the distortion center, which is typically different from the image center. The estimated distortion from the calibration enables us to back-project pixels into  $\theta$ , the angle between the camera optical axis and the 3D ray to the real-world scene. This allows to retrieve the angle  $\theta$  from any pixel of an image, as shown in Eq. (3.2).

$$\rho = \text{projection}(\theta) \leftrightarrow \theta = \text{projection}^{-1}(\rho) = \arctan\left(\rho / f(\rho)\right) \quad (3.2)$$

A limitation in using Scaramuzza's camera model is that the calibration is only validated within 150 degree-FOV. However, from a practical point of view, this limitation does not cause serious issues in the method; first, glare sources that are out of the 150 degree-FOV are highly

likely to be occluded by building components (such as walls, floor, ceiling, etc.) since the occupants are not seated exactly at the window surface. Also, we performed a validation of solar-tracking through the image projection (via estimated geometric parameters of the camera) against the computed sun-path during a sunny day and found it to have a very small error, as discussed in Section 3.3.5.

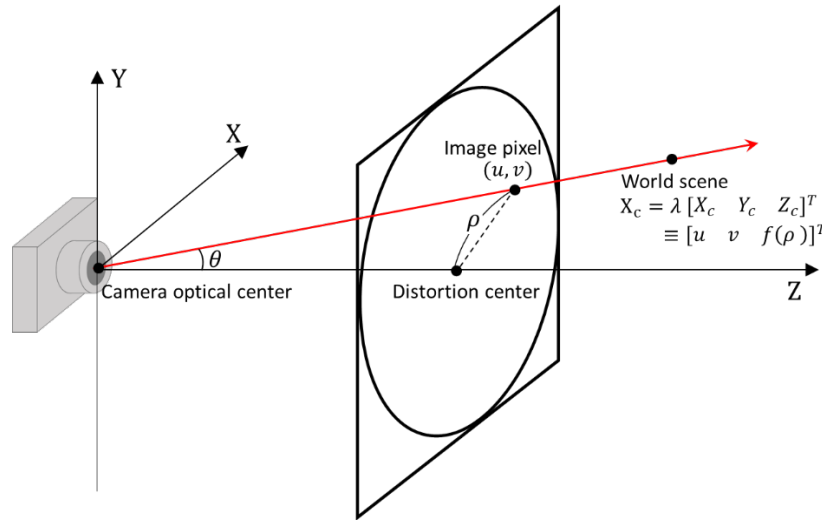


Figure 3.3 Illustration of fisheye camera projection model

The estimated projection can be used for the radial transformation of HDR images, a process essential for accurate geometry mapping. Since Evalglare is compatible only with HDR images of standard projections, such as equidistant (a projection that  $\theta$  is proportional to  $\rho$ ; see Figure 3.4b) or hemispheric fisheye projection, a 6<sup>th</sup>-order polynomial fitting (Figure 3.5) was used to create a radially mapping function that transforms non-standard fisheye projection into equidistant projection, using the RADIANCE pcomb command, according to the method described by Geisler – Moroder et al. [76]

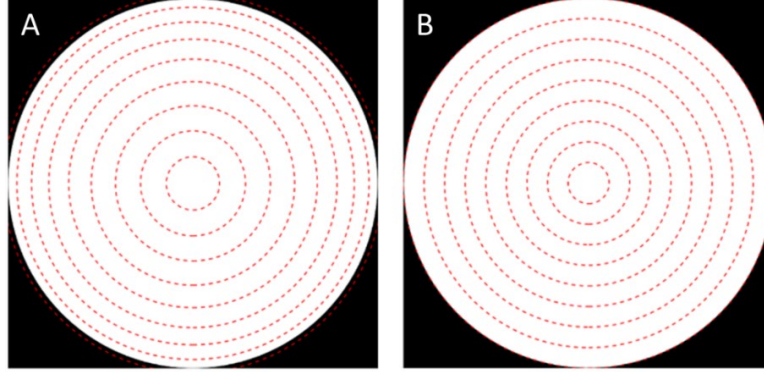


Figure 3.4 (a) Original fisheye projection (b) Equidistant projection. Each circle corresponds to equal  $\theta$  (from 10 degrees to 90 degrees, in 10-degree increments)

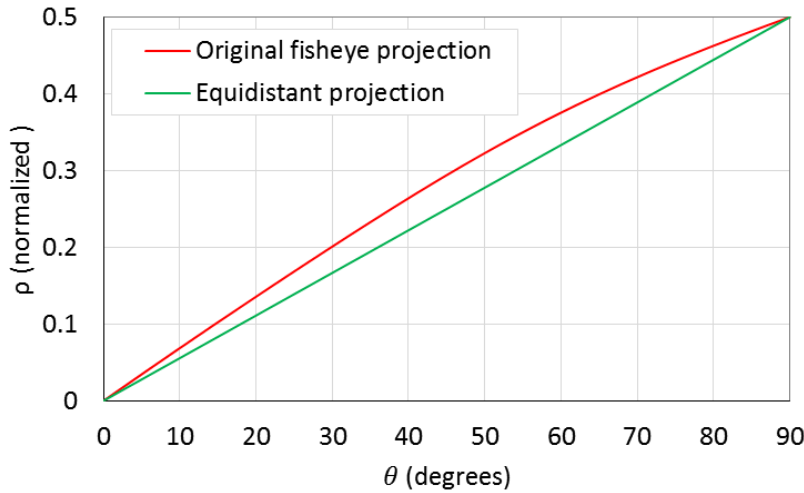


Figure 3.5 Estimated fisheye camera projection and fitted equidistant projection with a polynomial function

To validate the HDR imaging methodology, including photometric and geometric aspects, verification in terms of vertical illuminance (near the eye of the observer) was also done. This is a valid approach since illuminance is determined by both photometric and geometric factors, and is computed as the integration of luminance (photometric) in FOV along the configuration factor (geometric). This approach has been used in the past Konstantzos and Tzempelikos [38], for example when extreme luminance values are beyond the measuring range of conventional

luminance spot meters. A calibrated LI-210R photometer, with a cosine correction for incidence angles up to 80°, a response time of 0.01 ms and an absolute error of 3%, was used for the illuminance validation.

Figure 3.6 shows that vertical illuminance calculated from the HDR images showed good agreement with photometer readings, even in the higher range over 10,000 lx (RSE: 4.4%, RSME: 362 lx). Note that, when the sun is in the FOV and observed from the interior of the room, there will be overflown pixels due to the limited measuring capacity of the HDRI sensor (in the order of  $10^5$  cd/m<sup>2</sup> and higher). This can underestimate vertical illuminance when the sun is present and neutral density (ND) filters can be used to avoid this problem [38,154]. Nevertheless, this issue does not affect the operation of the proposed framework of this study, since the operating luminance threshold that will trigger shade movements is far below the measuring capacity.

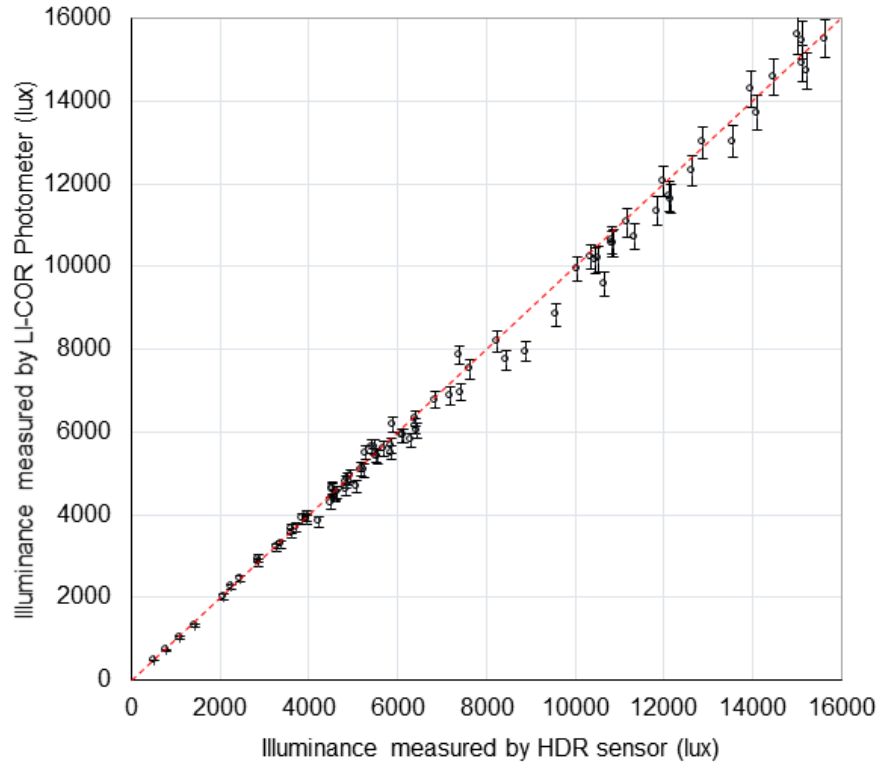


Figure 3.6 Vertical illuminance validation

### 3.3.3 Glare source detection

Evalglare is an open-source software used for glare evaluation from quantified physical entities in a fisheye HDR image Wienold [65]. Although the intended usage of Evalglare is to

analyze scenes observed by the human-FOV, its engine can also be utilized for identification of the luminance, size and position information of exterior bright sources that may contribute to glare. Figure 3.7 shows an example how Evalglare analysis is used towards identifying exterior sources of high brightness. Once the fisheye luminance map (Figure 3.7a) is read by Evalglare, pixels with luminance values above a certain threshold are identified as potential glare sources. Threshold luminance can be defined as either a fixed luminance value or as a multiplier to the average luminance of the entire FOV or the task area (the default is 5 times the average luminance of the entire scene). The neighboring source pixels are then combined into a single glare source shown as pixel groups with different colors (Figure 3.7b), depending on the maximum distance between two coupled pixels, as defined by the search radius command of Evalglare.

The detailed output of Evalglare allows access to detailed glare source information (average luminance, solid angle, position index, number of pixels, centroid pixel in x and y-coordinates) as well as overall information from the entire luminance map, such as calculated vertical illuminance, average and background luminance, and glare metrics including DGP and DGI. Peak extraction isolates pixels with extreme luminance, such as the sun or specular reflections from the identified source pixels. This is a useful method to separate the glare sources with extreme luminance such as the solar disk from other, less bright source pixels.

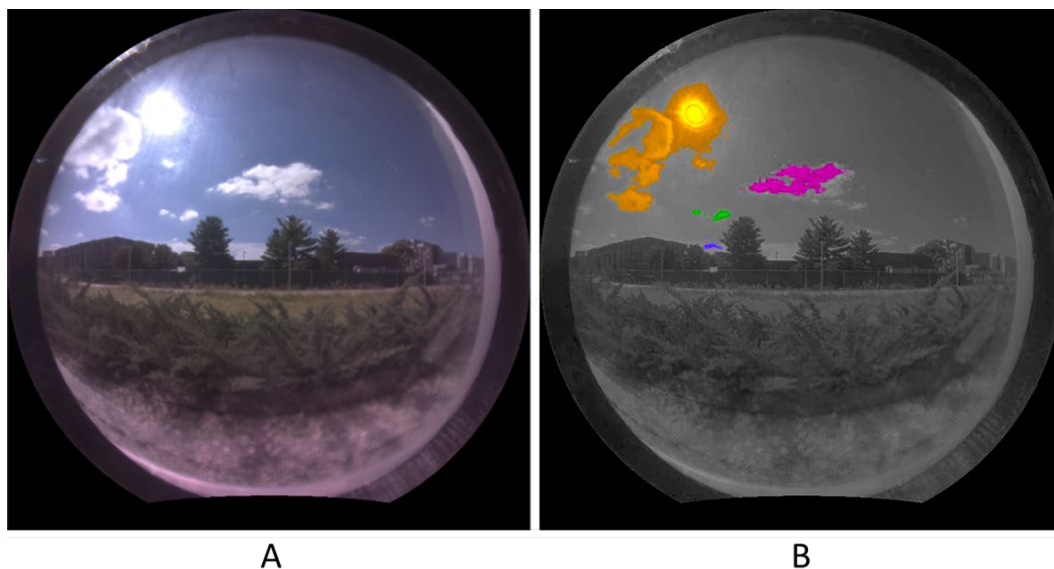


Figure 3.7 (a) Example of a processed HDR image for Evalglare analysis; (b) Example of color-mapped glare sources from the Evalglare output. The HDRI sensor identifies the location, size and brightness of a potential glare source in real-time.

Operating a shading control based on exterior reflections requires a threshold for identifying visual discomfort. However, there has been no validated border of visual discomfort in literature, and especially for instances of disability glare due to small but extremely bright sources, observed from interior workstations. Finding such a threshold is out of the scope of this paper, and it is a highly challenging goal that involves well-designed experiments with human subjects, which is ongoing research. Low thresholds, up to  $5500 \text{ cd/m}^2$  [84] have been proposed, although these include discomfort glare cases. Since human vision can capture between 2-3 orders of luminance difference and the luminance range on typical computer screens is  $30\text{-}200 \text{ cd/m}^2$ , Jakubiec & Reinhart [81] suggested a tentative upper limit luminance threshold around  $30,000 \text{ cd/m}^2$  for disability glare. As the scope of this study is a proof-of-concept for the new sensor-based glare detection and control framework, in particular due to small but extremely bright sources causing disability glare, the tentative absolute luminance threshold of  $30,000 \text{ cd/m}^2$  was tested.

### 3.3.4 Glare source positioning

Identifying the exact position of glare sources with respect to the sensor is necessary for glare-based shading control. For complete protection, the shade height needs to be set to a position that corresponds to the lowest profile angle among the entire set of glare source pixels. However, Evalglare only outputs the centroid pixel of each glare source, which may or may not be control-wise adequate information, depending on the size of the glare source of interest. For that reason, the source code of Evalglare was modified to output also the 1-dimensional pixel boundaries of every source in x and y-coordinates (red-border-lined boxes in Figure 3.8, middle).

Attaching the fisheye lens on the image sensor has the advantage of expanding the FOV. However, it also introduces complexity in finding the lowest profiles angle from the image. Because of the high distortion towards the edges of the fisheye image, horizontal lines in the image are not equivalent to lines of equal profile angles (Figure 3.8, left). Identifying the pixel of the lowest profile angle is not as simple as choosing the pixel with the lowest y-coordinate. There are



two options to find the exact pixel of interest: (i) exhaustively iterate over all the source pixels to find the one with the minimum profile angle; and (ii) rectify the fisheye image to remove the distortion and choose the source pixel that appears at the lowest vertical position. However, these solutions require high computational cost that would defeat the purpose of having a low-cost sensing system with restricted processing power. Consequently, an alternative method was used, which needs only four reference pixels – the pixel boundaries from the Evalglare output – per source. The modified code outputs the rectangular boundaries of glare sources similar to the illustration of Figure 3.8 (left). Instead finding the exact pixel of interest (with the lowest profile angle), the proposed logic simply chooses the lower of two profile angles that correspond to bottom vertices of the rectangle encircling the source. As seen in Figure 3.8 (left), the pixel location relative to the x-axis determines whether the profile angle increases or decreases with respect to the distance from the y-axis of the normalized image. For the upper half of the fisheye circle, the profile angle is lower in pixels closer to the mid-vertical line and the vice-versa for the bottom half. Since the chosen profile angle is the lowest within the rectangular boundary of the source, it is guaranteed that the sensing system always selects the profile angle closest to the actual lowest one. The profile angle  $\Omega$  required for the shade control is then retrieved by a simple trigonometric function as in Eq. (3.3):

$$\Omega = \arctan\left(v/f(\rho)\right) \quad (3.3)$$

where  $v$  is normalized y-coordinate of the pixel, and  $f(\rho)$  is the Z-component of the back-projected ray, which is a function of normalized radius from the distortion center, retrieved by the geometric calibration described in the previous section.

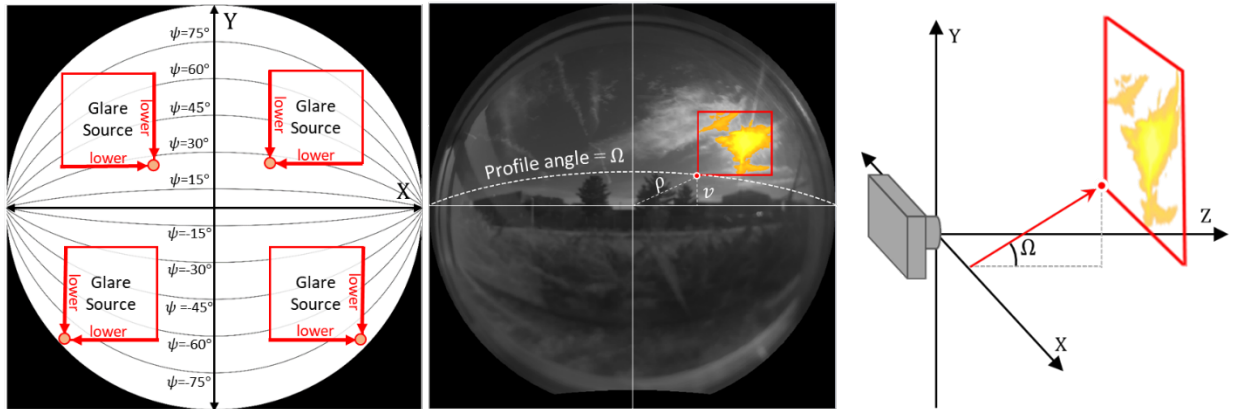


Figure 3.8 Illustration of proposed logic for finding the lowest profile angle of glare sources

### 3.3.5 Solar Tracking for daylight glare control using fisheye HDRI sensor

Solar tracking is an essential feature in daylighting controls since (i) avoiding sunlight on the person is required and (ii) the presence of sunlight and its direction significantly changes interior luminous conditions. Existing daylighting controls based on solar tracking calculate the sun path or position based on the location and orientation of the building; these are then used to calculate the incident or profile angle of the solar rays incident on the facade and transmitted through the windows. However, the solar path method is not always self-sufficient for robust daylight glare control. If the building is located in a dense urban environment, the sun may be occluded for part of the day, or even at all times. Also, the visibility of the solar disk can significantly vary depending on the weather conditions. For these reasons, simple solar path-based shading controls tend to be over-conservative, and often need to be paired with extra feedback sensors on the window, which still cannot efficiently handle reflections from surroundings.

Image-based solar tracking overcomes these problems and can eliminate the need for a solar path model or building geometry and location information. The solar tracking based on the luminance map is performed by the peak extraction method of Evalglare. The absolute luminance of  $380,000 \text{ cd/m}^2$  was chosen as the peak threshold (we could select a lower value since anything close to this value will definitely cause disability glare anyway). For capturing the exact position of the sun from the window view, a similar positioning method with the one described in Section 3.3.2 was used. However, in this case the centroid of the solar pixels' block is used instead of the pixel corresponding to the lowest profile angle. Once the centroid is retrieved from the Evalglare output, the incident and profile angle of the solar rays can be calculated. The profile angle can be obtained using the same method for other glare sources, while calculating the solar incident angle  $\theta$  to the façade is trivial since the processed image already has equidistant projection. The angle between the camera's optical axis and the sun's rays is proportional to the pixel distance between the centroid and the distortion center (Figure 3.9).

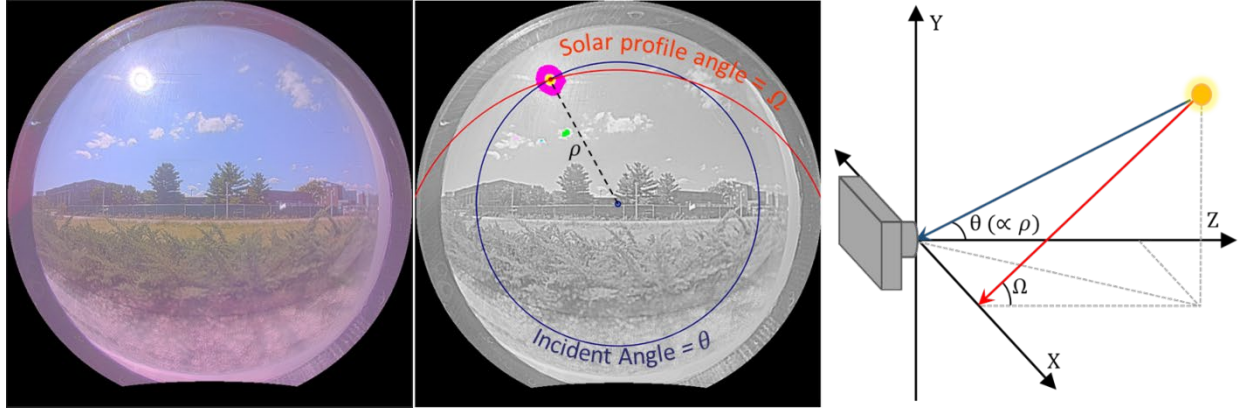


Figure 3.9 Solar tracking example from a processed HDR fisheye image

To evaluate the solar tracking methodology, we compared the profile angle of the sun calculated based on HDRI images and using the standard calculation (Eq. 3.5) with known parameters using a Python library, PyEphem-Sunpath [155]. The library allows retrieval of accurate solar azimuth and altitude at the Earth surface given the geographical information (latitude and longitude) and local time.

$$\Omega = \arctan\left(\frac{\tan(\alpha)}{\cos(\varphi - \gamma)}\right) \quad (3.4)$$

where  $\alpha$  is the solar altitude angle,  $\varphi$  is the solar azimuth angle, and  $\gamma$  is the surface solar azimuth with respect to true south. Figure 3.10 shows the solar profile angle calculated with both ways in four-minute intervals during a sunny day in April. The RMSE is 1.33 degrees (2.1% RSE) which shows that the image-based solar tracking method works well. For a realistic illustration, the position of the solar-disk centroid, monitored from the fisheye image, was overlaid together with a projection of the sun calculated by the sun-path algorithm in Figure 3.10. The average Euclidean distance between corresponding pixels is 3.83 pixels (0.006 when normalized with the image resolution). Despite the small pixel error outside the 150-degree-FOV zone, the profile angle difference is noticeable in early morning and late afternoon. That is mainly due to excessive solar azimuth angle range (above 65 degrees) with respect to the building facade. However, as shown in Figure 3.10 (left), the solar profile angle estimated from the HDRI sensor is consistently lower in these cases. This means that the HDRI sensor will allow a more conservative control during these times and can be safely applied in building control systems.

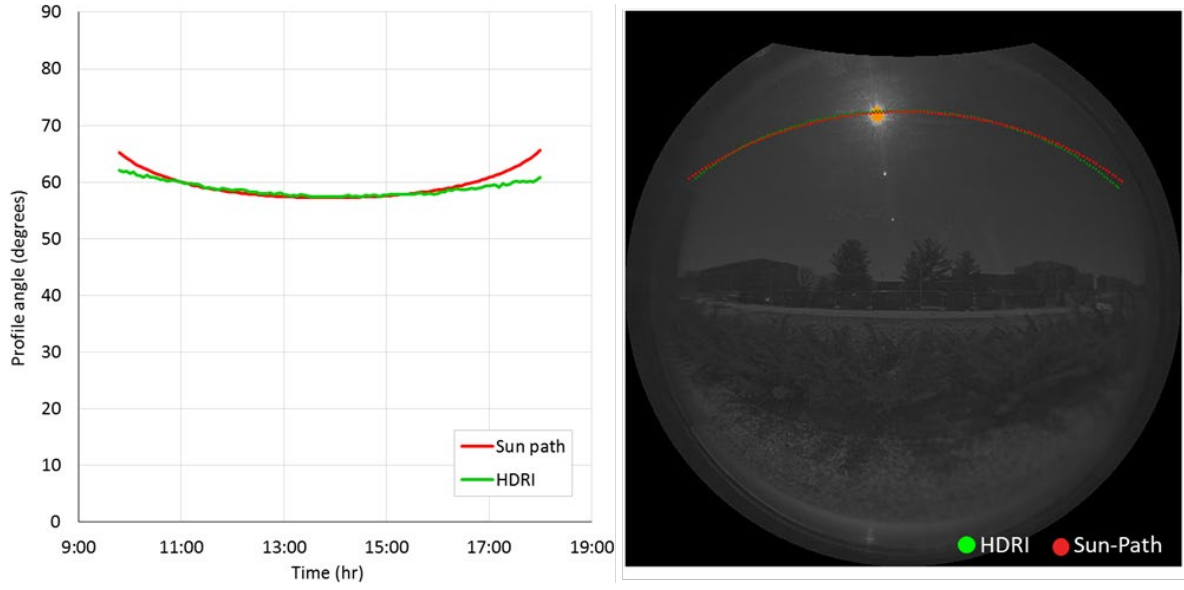


Figure 3.10 Comparison of the profile angle calculated from HDR images and Sun-path method (left). Overlay of solar disk on fisheye HDR images (right)

### 3.4 Glare-based shading operation using the window-mounted HDRI sensor

Two layers of automated glare protection utilizing the HDRI sensor are proposed, aiming at deploying roller shades at a height that avoids glare induced either from exterior or interior bright sources (sunlight or reflections). The first layer protects the occupant from any exterior glare-inducing sources detected by the HDRI sensor (over  $30,000 \text{ cd/m}^2$ ). To that end, it moves the shade to a height where the source-to-eye ray intersects the glazing (Figure 3.11, top), based on the eye-height ( $h_{eye}$ ) and target distance of the "minimum glare-free" zone from the window ( $d_{eye}$ ). If no glare source is captured by the sensor, the shade position is set to fully-open.

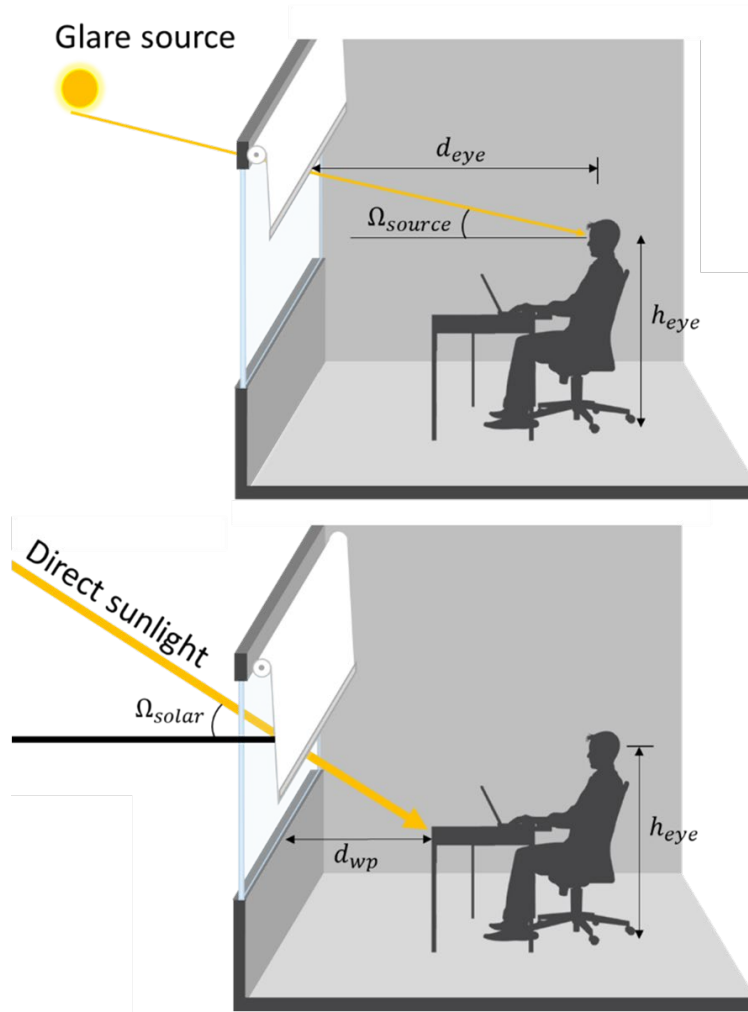


Figure 3.11 Illustration of shade control operated by the new sensor-based control system. Eye-height protection from exterior glare source system (top); Work plane protection from direct sunlight (bottom)

The second layer of protection protects the work plane (at height  $h_{wp} = 0.8\text{ m}$ ) from directly transmitted sunlight at a target distance from the window ( $d_{wp}$ ) as shown in Figure 3.11 (bottom). That is because interior sunlight reflections near the work area can trigger discomfort. This is simply based on geometry and has been applied in earlier studies [99,100]. Here this logic is operated only when the camera detects the sun as a glare source (as described in the previous section). At each control iteration, the HDRI sensing system calculates shade positions from both control objectives and chooses the lowest between them (Figure 3.12).

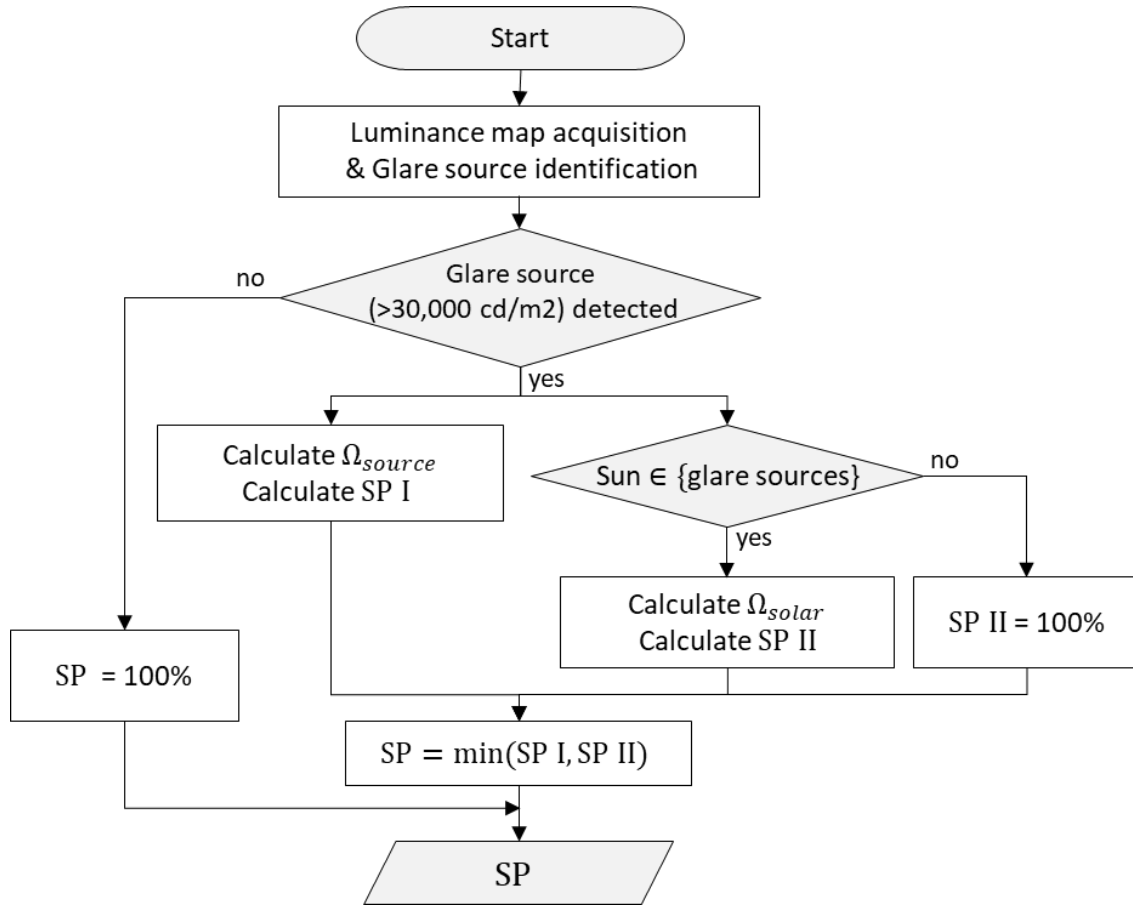


Figure 3.12 Glare protection flowchart with HDRI sensor

However, controlling based on the profile angle observed from the window HDRI sensor involves some limitations. The occupant's FOV can be substantially different from what is captured by the window HDRI sensor in two different levels, because: (i) a portion of the window sensor's visual field is not visible from the inside due to occlusion from the building enclosure and (ii) even when a glare source is perceived by both the occupant and the sensor, the observed profile angles are not the same, when the source is not far away like the sun. While the former is a limitation that will always lead to a more conservative shade operation, the latter is more complicated and is analyzed below.

As illustrated in Figure 3.13, different positions of the occupant and the window HDRI sensor create different profile angles (occupant:  $\delta$ ; window HDRI sensor:  $\Omega$ ) perceived for the same glare source. If the source is located below the occupant's line of sight, the control algorithm

detects the source in the lower position ( $\Omega_l$ ) than the actual ( $\delta_l$ ), behaving more conservative and limiting daylight harvesting. On the contrary, for glare sources above the line of sight, the shade height will be determined by  $\Omega_h$  which is higher than the actual profile angle  $\delta_h$ , potentially exposing occupants to glare sources. Assuming that occupants are seated at least 1 m from the windows, the shade distance from the floor is simply calculated by adding the tangent of  $\Omega$  to the occupant eye height ( $h_{eye}$ ). Considering that, for typical urban environments and street widths, any reflected glare source should be at least 10 m away from the window, the relative error between the tangents of  $\delta$  and  $\Omega$  (shade position differences) is less than 10%, as shown in the graph of Figure 3.13 (bottom). The further away the source is, the smaller the difference in the controlled shade positions due to the occupant-sensor distance. Also note that the maximum difference between the shade positions, based on  $\delta$  and  $\Omega$  respectively, is limited because the maximum of  $\tan(\Omega)$  –total shade height minus occupant eye height is typically lower than 2.5m since ceiling heights are around 3 m in most offices.

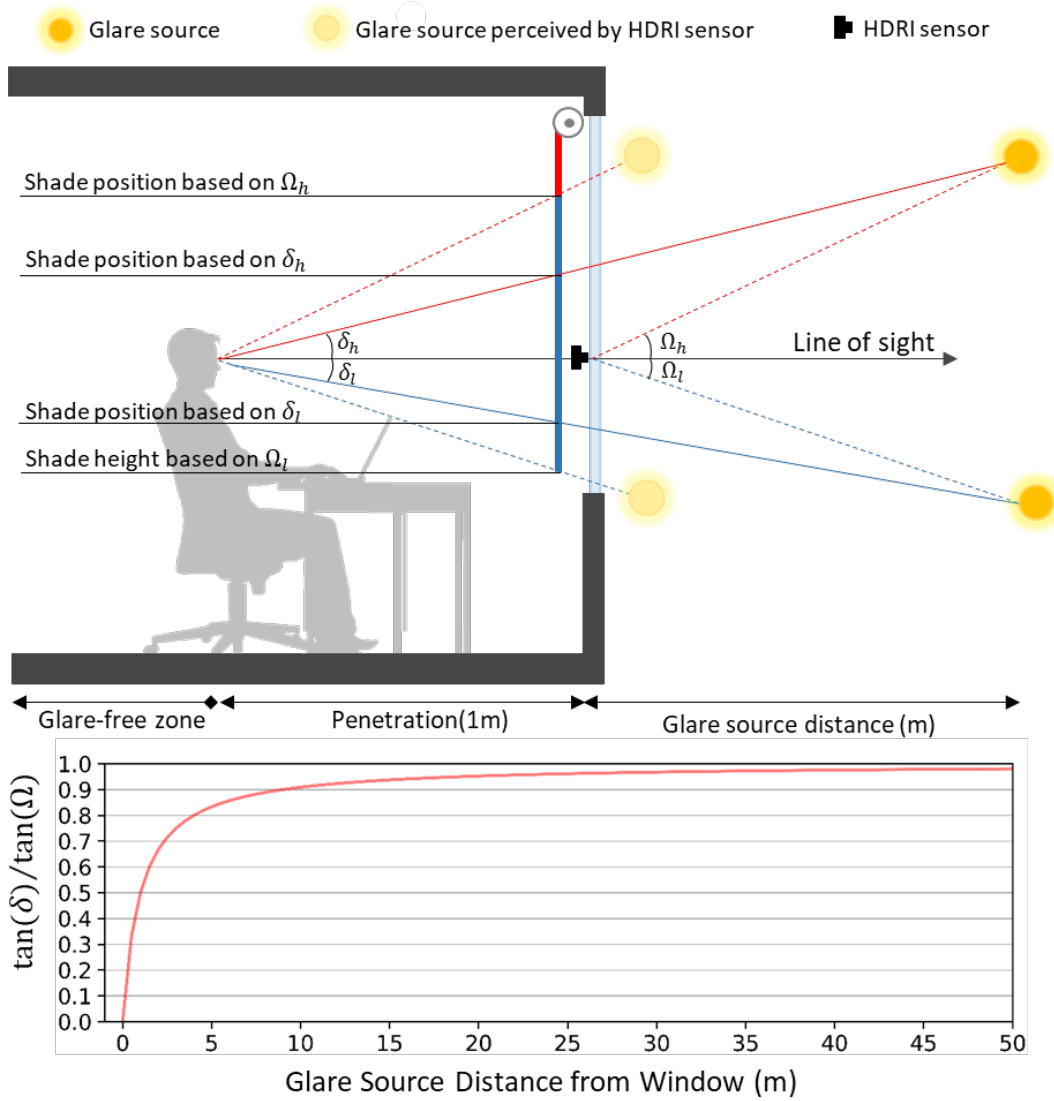


Figure 3.13 Illustration of angular deviation caused by different distances from the glare source (top); Ratio of tangents of the angles  $\delta$  and  $\Omega$  dependent to glare source distance from the window (bottom)

### 3.5 Implementation of the HDRI-based glare control framework and case study

#### 3.5.1 Experimental setup and control integration with the Building Management System

A 3.3 m  $\times$  3.7 m  $\times$  3.2 m high private office in West Lafayette, Indiana (40°25"N, 86°55"W) with a south-facing façade was used to implement the proposed control framework with the window-mounted HDRI sensor. The façade consists of aluminum curtain wall framing and a high-



performance glazing unit (normal  $T_v=64\%$ ) with a window-to-wall ratio of 54%. The room is equipped with interior dark-colored motorized roller shades (normal  $T_v=2.53\%$  and  $OF=2.18\%$ ) and two suspended electric lighting fixtures (each with two 32-W T5 fluorescent lamps). The window HDRI sensor was attached on the interior of the glazing at 1.2 m from the floor (close to typical eye height of seated occupants). To evaluate scenes as observed by an occupant during the shading operation, an additional HDRI sensor was installed at the same height at the occupant position (1.5 m distance from the window facing outside as in Figure 3.14). Both sensors were operated by a single Raspi, enabled by adding an IVMECH Dualplexer V2, which allows connecting more than one camera modules to a single CSI camera port on *Raspi*. Two LI-210R photometers were installed right next to the HDRI sensors to measure vertical illuminance. Measurements were scheduled and collected by an Agilent 34972A DAQ unit.

As the external surroundings visible from the testbed office did not create very bright reflections, a reflector panel was used to create artificial glare sources and mimic exterior reflections for the purpose of the experiments (Figure 3.14). A reflective (mirror-like) finish material was placed on the panel, which had a total area of 1.5 m by 1.2 m. The panel was rotatable and could be placed in any direction, therefore it allowed us to evaluate sources of varying luminance, from a few hundred to over 300,000  $\text{cd/m}^2$ , and varying source size, depending on the relative position of the sun. Luminance values were also measured with a calibrated luminance spot meter, installed next to the installed sensors, aiming at the center of the reflector.

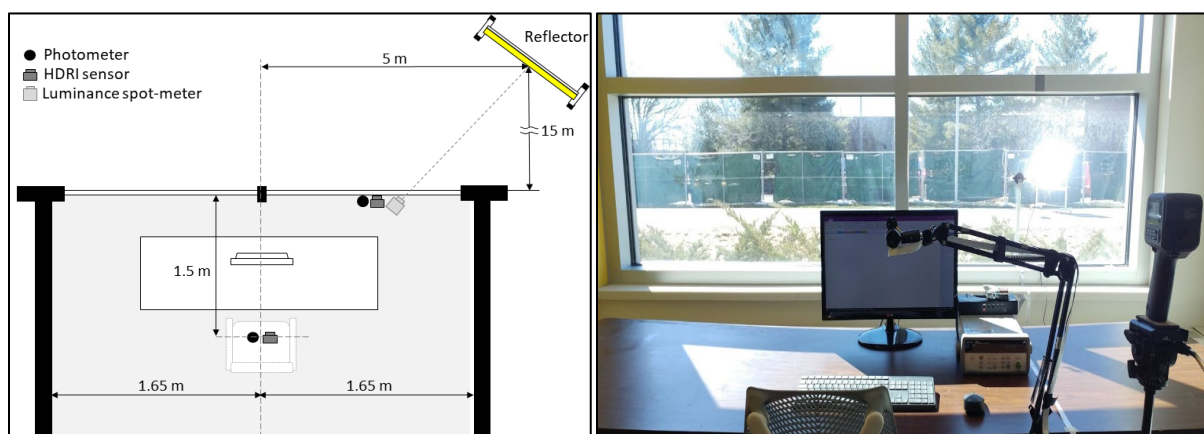


Figure 3.14 Instrumentation schematic (left); observed scene with the exterior glare source (reflector) visible from the interior of the test office, and additional sensors installed at the occupant location (right)

Shading and lighting can be precisely controlled through corresponding control points in the Niagara<sup>AX</sup> Framework [156], which is the Building Management System (BMS) in the building. The new HDRI sensor was integrated in the existing BMS as illustrated in Figure 3.15. Different types of actuators are controlled with Tridium JACE controllers as part of the Niagara<sup>AX</sup> Framework, which allows seamless integration of the building systems irrespective of manufacturers or communication protocols. The shading glare-based control using the window HDRI sensor was operated in *Raspi* through Python scripts. The Python control script determines the set point for the shade position (0-100%, fully-closed to fully-open) in the BMS. The communication between the *Raspi* and BMS was achieved using the Modbus TCP communication protocol with Python *PyModbus* package as an interface. A writable-Modbus holding register was created to receive and send the shade position set point to the corresponding control point in the BMS. The entire process takes about 2 seconds.

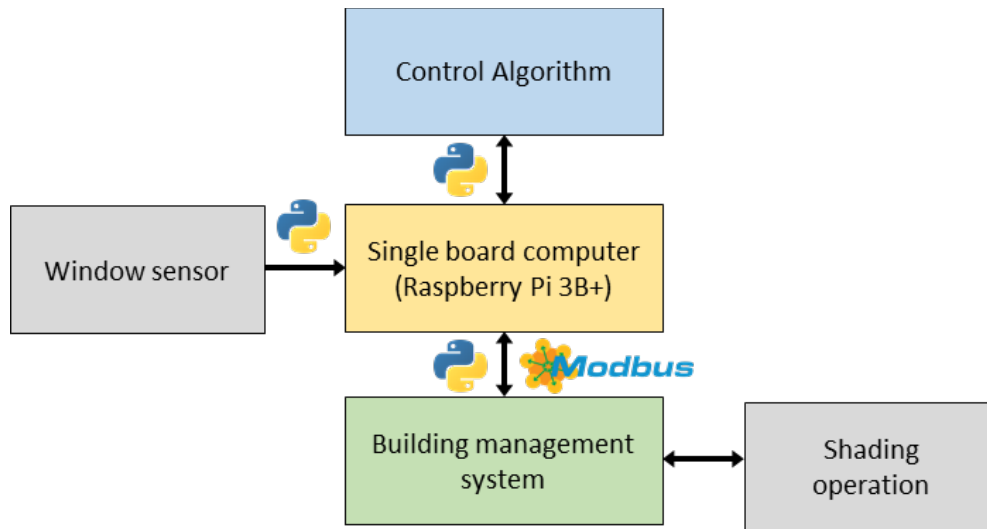


Figure 3.15 Overview of HDRI sensor and shading control integration in the BMS

### 3.5.2 Implementation and comparison with common shading controls for glare protection

Measurements were collected during sunny days in March-April 2019. Data points with reflector luminance over the 30,000 cd/m<sup>2</sup> threshold were used in the analysis. The average luminance of the reflector panel ranged between 36,800 - 332,000 cd/m<sup>2</sup>, while the solid angle of the reflector, as seen by the sensor, ranged from 0.0015 - 0.0077 sr. The selected distance between the occupant and the window ensured that the solar disk is not visible from the occupant-positioned

HDRI sensor during the experimental period, thus no overflow issues affected the interior HDR luminance map.

As described in the previous section, the HDRI-based glare control moves the shades to a height just adequate to cover the lowest profile angle, relative to the person, of any detected glare source (sunlight or bright reflections). It has an advantage over any other direct glare protection method, since it can identify the location, size and brightness of any potential glare source in real-time. To demonstrate these advantages experimentally, the HDRI-based control was compared with:

- A typical “sun-tracking” control, which moves shades to cut-off height that blocks direct sunlight from the occupant’s eyes. This control cannot account for any glare source other than the sun and also can result in high vertical illuminance and discomfort glare when the sun is high in the sky.
- A control that avoids “excessive illuminance”; it operates shades based on transmitted illuminance through the window and moves the shades to the eye height whenever it exceeds a threshold, to avoid excessive vertical illuminance or large glare sources. This threshold can be variable to account for room and window geometry as well as weather conditions, but for our experimental space and sky type it is set to 8,000 lx. This control might over-protect from glare, reducing the admission of useful daylight, and it cannot work for glare sources below the line of sight.

In each experimental run, the reflector tilt was changed to create a specific luminance range at its center. The shades were then controlled with the HDRI-based control, the sun-tracking control and the excessive illuminance control. For each of these operations, all useful measurements were collected, including the average luminance of the source (reflector) measured by the window HDRI sensor, the shade position, vertical illuminance at the occupant position, as well as an interior luminance map using the occupant-positioned HDRI sensor. The latter was used to calculate DGP at the occupant location (the standard *Evalglare* source detection method was used for that purpose, with five times the task average luminance (marked as 0.53 rads around the center of the computer screen). A different reflector luminance was then selected randomly and the entire cycle was repeated. Each cycle lasted less than 30 seconds, thus it was safely assumed that there was no significant luminance variation in the exterior scene (stable, sunny days) during a cycle.

An example of the experimental comparison of the three controls is presented in Figure 3.16. For a given exterior scene with the sun present and the reflector used as a second glare source, HDR images from the occupant sensor are shown after each control is applied. As expected, the sun-tracking control failed to block the reflector, while the excessive illuminance control provided only partial glare protection from the reflector because its line of sight of was partly below the eye height (zero profile angle). On the contrary, the HDRI-based control successfully moved the shade to just cover the reflector surface, fully protecting from the detected glare source as intended.

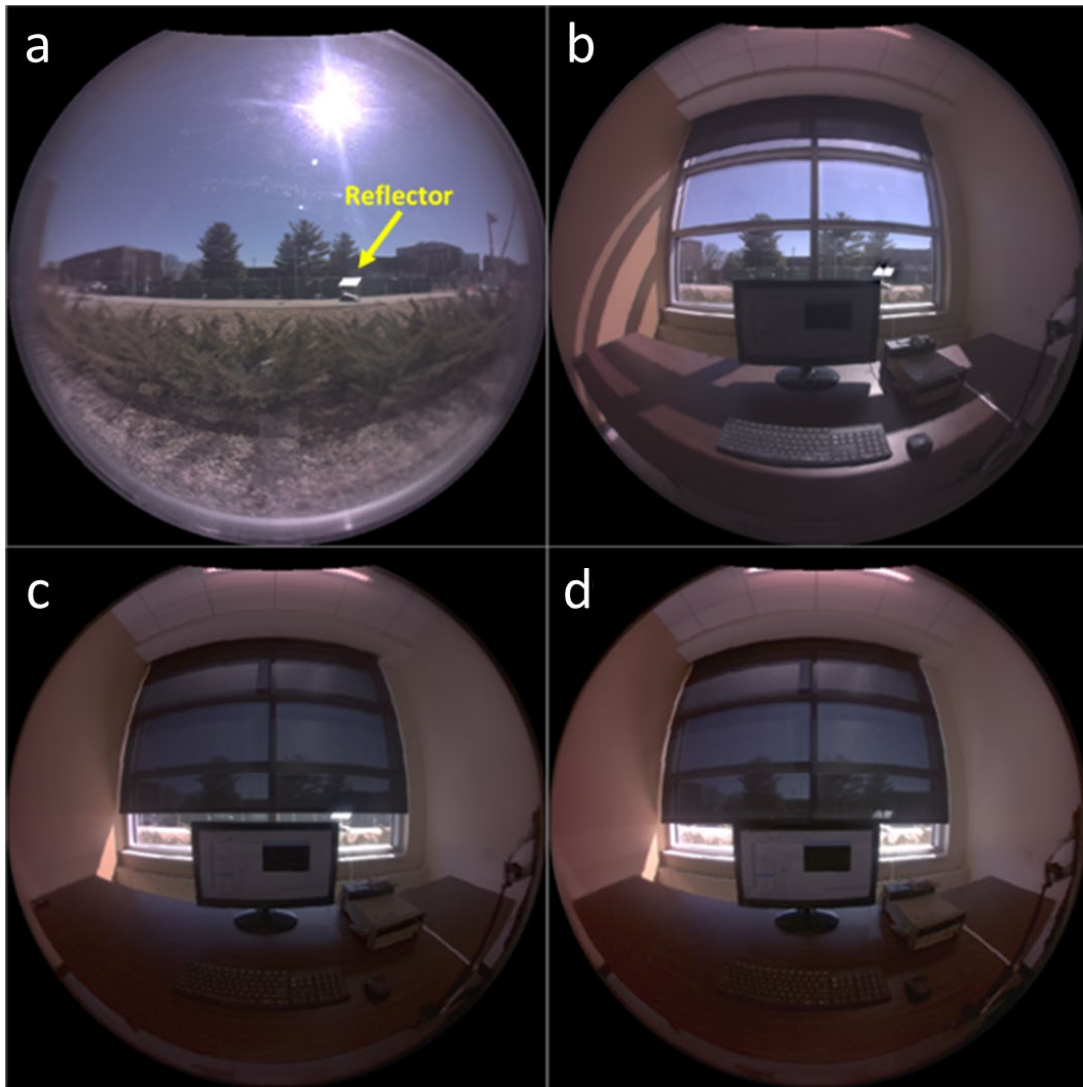


Figure 3.16 HDR images from the implementation case study: Exterior Scene (a) and occupant views with the solar-tracking control (b); excessive illuminance control (c); and HDRI-based control (d), fully protecting from the detected glare source.

More quantitative comparative results are shown in Figure 3.17. For a meaningful representation, the 40 data points (x-axis) are sorted by average luminance of the reflector in ascending order (Figure 3.17, top), and then the resulting shade position,  $E_v$  and DGP at the occupant position are presented for each data point with each of the three controls.

The simple solar tracking control results in higher shade positions due to the high profile angle of the sun, and consequently, in high vertical illuminance on the eye and DGP values. Both remain higher than the recommended glare thresholds (2,760 lx for  $E_v$  according to [38,67] and 0.35-0.40 for DGP based on [42]). However, to be fair, note that the difference in DGP between the solar tracking control and the rest is mainly due to the vertical illuminance term and not the contrast (reflector luminance) term. That is because small but bright sources, such as the reflector used in our experiment, usually have a small contribution to vertical illuminance due to their small solid angle (except if their luminance is extremely high). Nevertheless, the fact remains that simple solar tracking control cannot protect from glare.

On the other hand, the excessive illuminance control can be directly compared to the HDRI-based control in terms of DGP effects (vertical illuminance differences between the two controls only account to 0.03 of the difference in DGP). Since the lower part of the reflector panel is located just slightly below the line of sight of the observer, the differences in shade positions with these two controls are not important (mean difference of 6.3% converted to 13 cm in actual height).

The HDRI-based control always keeps DGP and  $E_v$  at comfortable levels. However, since part of the reflector is visible with the illuminance control logic, DGP increases with reflector luminance and reaches the threshold of 0.35 approximately at 150,000 cd/m<sup>2</sup> (reflector average solid angle is 0.003) using that control, which is certainly possible with specular reflections on building facades. It is worth noting that, for a certain range of reflector average-luminance (150,000~200,000 cd/m<sup>2</sup>) with the illuminance control, DGP can exceed 0.35 without noticeably increasing the vertical illuminance. This finding confirms that previous daylighting controls relying only on photometers could fail to protect from direct glare in such conditions, and HDRI-based controls are more reliable.

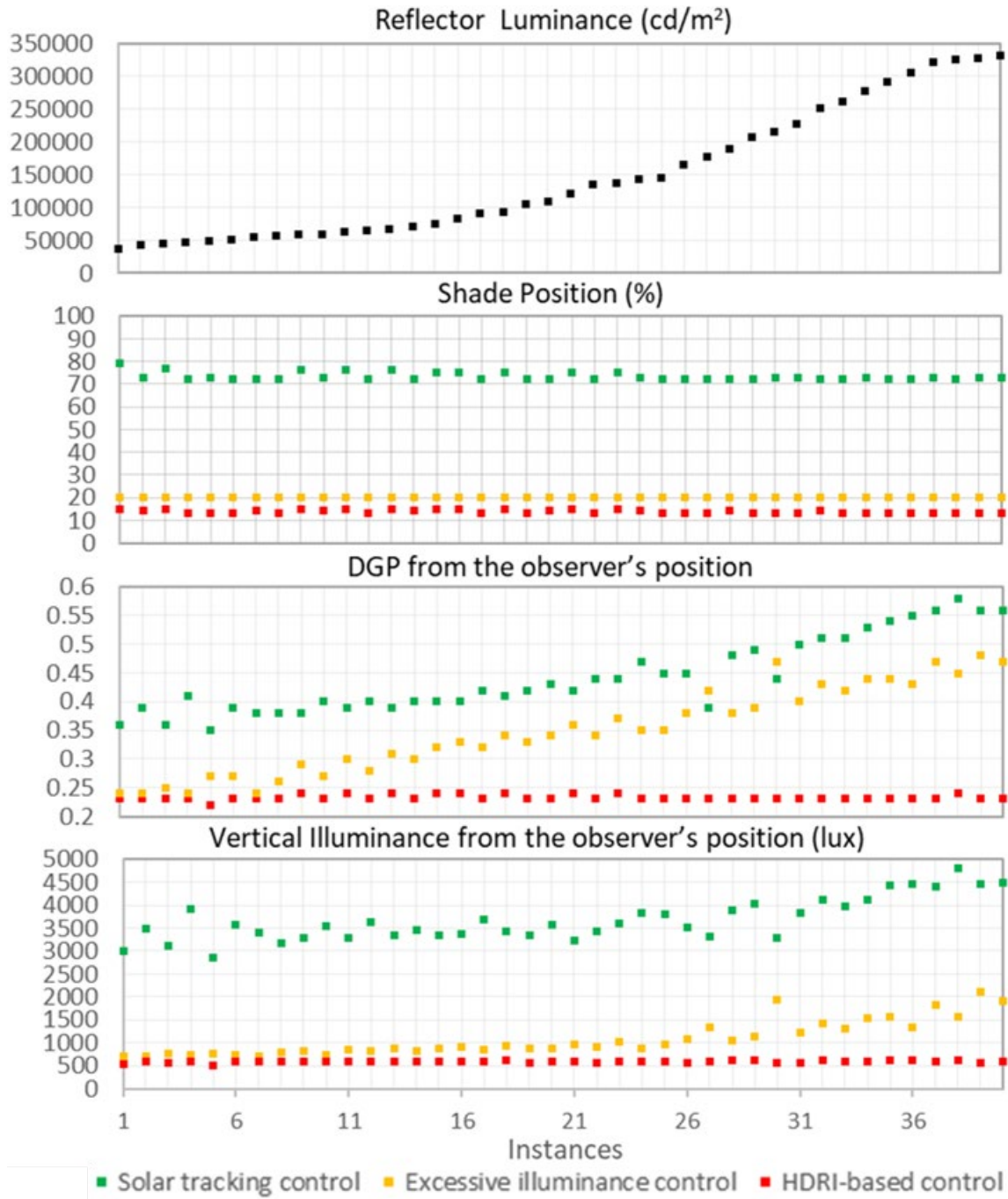


Figure 3.17 40 data points (x-axis) sorted by average luminance of the reflector in ascending order (top) and comparison between respective shade positions, DGP and vertical illuminance at the occupant position, with each shading control.

### 3.6 Chapter conclusion

This study presents the development and implementation of a new daylight glare control framework. Until now, conventional control systems could not detect the location, size and brightness of potential glare sources in real-time, resulting in either increased glare risk or over-conservative shading operation. A low-cost programmable HDRI sensor with a wide fisheye lens was attached on the inside surface of the glazing to capture the full luminance distribution of the exterior scene. After proper photometric and geometric calibration, the HDRI sensor can be used for efficient luminance mapping and further processing of any of the image's pixels of interest. We present a method to enable reliable solar-tracking without prior information or commissioning, and an efficient glare source positioning algorithm, which can also detect glare sources of small size but significant luminance (such as reflections from opposite facades), according to the programmed logic. A secondary layer of protection from reflections near the work plane is presented, and the effect of the occupant and source position relative to the sensor is discussed.

To demonstrate the HDRI-based glare control, experiments were conducted in a private office with automated roller shades. Reflective panels were used to create bright sources of varying size and intensity, in addition to the sun. The new control was operated in Raspi through Python scripts and was integrated into the BMS using the Modbus TCP communication protocol. Two more shading controls, a simple sun-tracking control and a control to protect from excessive vertical illuminance, were also implemented for a direct comparison under the same sky conditions. The results showed that the HDRI-based glare control successfully moved the shades continuously to fully protect from the detected glare source, maintaining low DGP and vertical illuminance values measured at the occupant position inside. Simple sun-tracking cannot prevent from glare. The illuminance control cannot work well for sources below the horizontal line of sight, while it may result in high DGP without reaching increased vertical illuminance values, which might happen with specular reflections from opposite building facades.

The proposed hardware and control framework have limitations. The maximum dynamic range of the image sensor used in this study cannot measure extremely high luminance levels (above  $420,000 \text{ cd/m}^2$ ), creating overflow issues when it tries to capture the sun. Although this is not a big problem, since we can set a lower peak value and use the solar tracking algorithm, it can be avoided by using a sensor with a wider dynamic range [90]. Also, the developed control assumes that glare sources are beyond a certain distance from the window, thus the relative position of glare

sources with respect to an occupant can be well approximated with the window-mounted HDRI sensor. The control could fail to protect from glare sources very close to the facade (5 m or less), although this is not likely to happen.

Although the developed HDRI-based glare control should work better than any other existing method for direct glare protection, it cannot ensure elimination of general discomfort glare (because when the profile angle of the source is high, the shades will move to a high position and that might cause problems similar to “excessive illuminance” type of controls). Therefore, for total daylighting and visual comfort control, the HDRI-based glare control should be added as an extra layer of protection in efficient daylighting controls.

Finally, although it is out of the scope of this study, there is no reliable predictor for daylight glare caused by relatively small sources of significant brightness, despite recent studies related to pupil responses, especially pupil size [157,158]. Determining a practical and reasonable operating luminance threshold for HDRI-based control is a challenging process that should involve experiments with human subjects in multiple indoor environment setups and locations, and it is suggested as future work.

This study is an initial step towards developing a novel daylighting control framework based on HDRI sensors. Future applications are not necessarily limited to efficiently detecting relatively small and bright glare sources, as in this study, but also extend to: enabling model-based controls using the exterior luminance distribution as a quality input; learning visual preferences of occupants associated with the exterior scenes; and eventually fully replacing conventional photometer-based fenestration controls.



## 4. A LOW-COST FISHEYE-STEREO CAMERA SENSOR FOR DAYLIGHTING AND GLARE CONTROL

### 4.1 Scope and objectives of the study

This study presents the development of a window-attached, low-cost fisheye-stereo camera sensor system for reliable daylighting controls in buildings. The stereovision sensor composed of two cameras can measure 3-D position and luminance of any exterior bright sources after photometric and geometric calibration. Also, by applying a neutral density sensor on one of the cameras and substituting the overflown pixels of the luminance map, a complete luminance map with a wide dynamic range can be retrieved. The new sensor exhibited promising results in validation of 3-D positioning and luminance acquisition, and can be used for real-time glare source detection, location and intensity measurements. The overall process is shown in Figure 4.1.

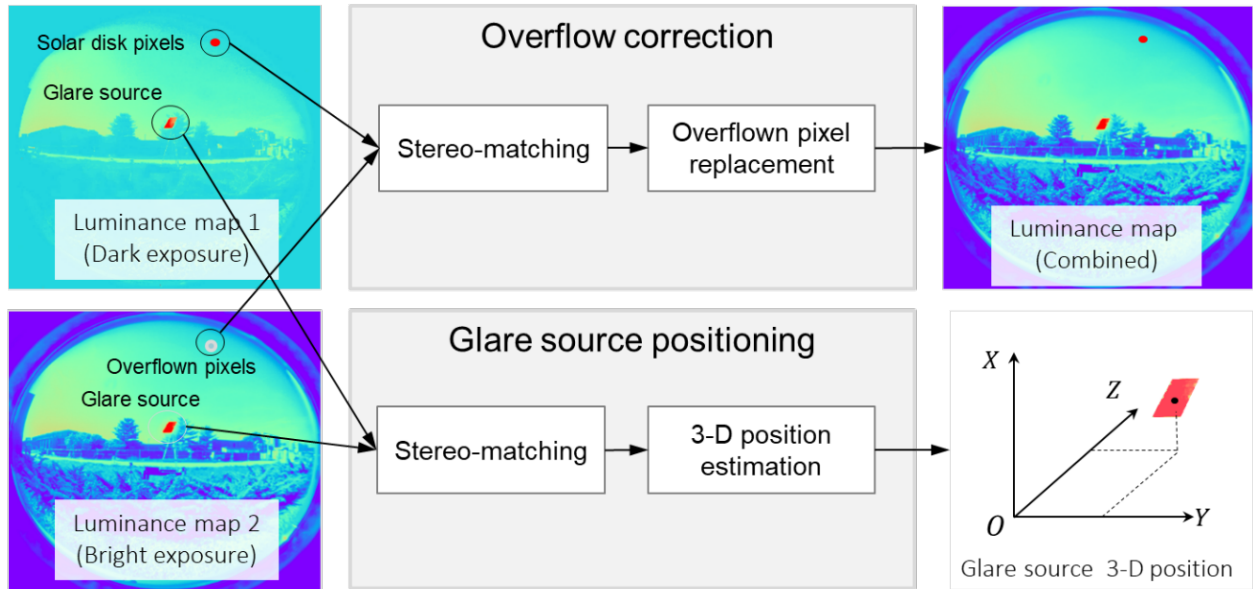


Figure 4.1 Overview of fisheye-stereo vision sensing system

### 4.2 Fisheye-Stereovision System

Two low-cost camera boards (Raspberry Pi Camera Module V2) are the main components of the stereovision system setup (Figure 4.2). The camera board is based on the 8-megapixels CMOS sensor (Sony IMX219) and its operation is fully programmable with Raspberry Pi (Raspi)

through a Python interface. To capture the full exterior scene through the window, a wide-angle fisheye lens was attached to each camera board to expand the field of view (FOV) to nearly 180 degrees. Two camera boards are horizontally integrated via a 3-D printed mount with the baseline distance of 15cm and connected to a single Raspi using IVMech multiplexer V2. In the left camera, an ND4 filter was applied between the image sensor and the fisheye lens as in [154]

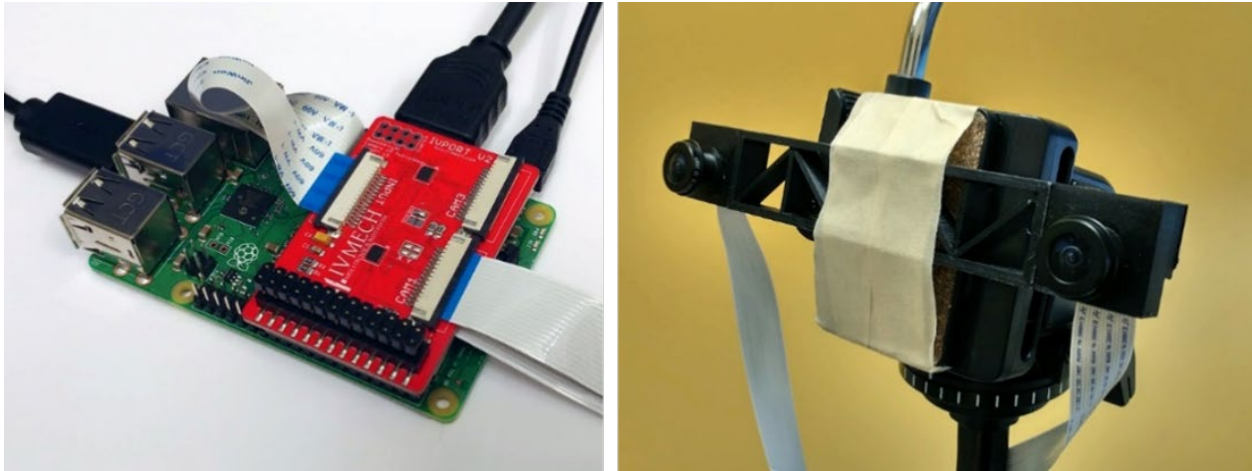


Figure 4.2 Raspberry Pi B+ with IVMECH V2 camera multiplexer (left). Fisheye camera integrated with 3D printed mount (right)



Figure 4.3 Fisheye stereovision sensor mounted attached to window

### 4.3 Fisheye-Stereovision Sensor Calibration

#### 4.3.1 Photometric calibration

Photometric calibration is an essential process to acquire reliable luminance readings from HDR images largely composed in three steps; 1) camera response function (CRF) retrieval, 2) calibration factor (CF) estimation and 3) vignetting correction [27]. The CRF is the key component of HDR imaging, which refers to a non-linear curved function associating radiometric intensity to absolute values of luminance. In the present study, a CRF estimation algorithm proposed by [26] was used, using its OpenCV (computer vision library for C++/Python) implementation. Input to the CRF estimation is a set of low-dynamic images with different exposures. After creating HDR images with the estimated CRF, the calibration factor (CF) that converts the HDR pixel intensities is calculated by fitting the HDR intensities to the absolute luminance measured by scientific-grade luminance spot-meter on the diffusive, neutral-colored surface. The luminance of a gray-colored square placed at the camera optical center (retrieved from the geometric calibration) was calculated from the un-calibrated HDR images and fitted to the luminance spot meter reading by a multiplication factor. To reduce measurement and temporal error, CF was averaged from ten different measurements. The luminance measured by the spot-meter ranged from 4,800  $\text{cd/m}^2$  to 7,540  $\text{cd/m}^2$ . The final part of the photometric calibration is the correction of the vignetting effect, a radial decrease of luminance observed in fisheye cameras of fast apertures that comprises the measurement accuracy of luminance. The process [27] was performed to obtain a 5th-degree polynomial correction function, which was then applied in HDR images via RADIANCE [66].

From the CF retrieved from the non-filter camera, the range of reliable luminance measurement was estimated from the fastest shutter speed used in HDR creation. The HDR merging algorithm weights calibrated intensities from the low-dynamic images based on the isosceles triangle-shaded function that peaks at mid-intensity (128 for 24-bit RGB image) of the image. Thus, the luminance value corresponding to the 50% of the mid-intensity (192 for 24-bit RGB image) calculated from the lowest and the highest exposures can be considered reliable, assuming proper photometric calibration. As shown in Figure 4.4, the measurable luminance ranges by two cameras are 165 ~ 117,000  $\text{cd/m}^2$  (non-filtered) and 11,745 ~  $2.8 \times 10^9 \text{ cd/m}^2$  (ND4). Since the overlapping ranges from 11,745  $\text{cd/m}^2$ , bright sources above this range can be identified by both cameras. Although the luminance of the solar disk observed on earth can reach  $1.6 \times 10^9$

$\text{cd/m}^2$ , the ND4 filtered camera is able to capture most of the instances considering the observed luminance under solar incidence angles on building facades and typical visible transmittance of modern window systems. In any case, values in the order of  $10^9 \text{ cd/m}^2$  are much higher than any discomfort thresholds. The optical filter density above 4.5 will be sufficient for Raspi camera board to capture solar the disk in all circumstances.

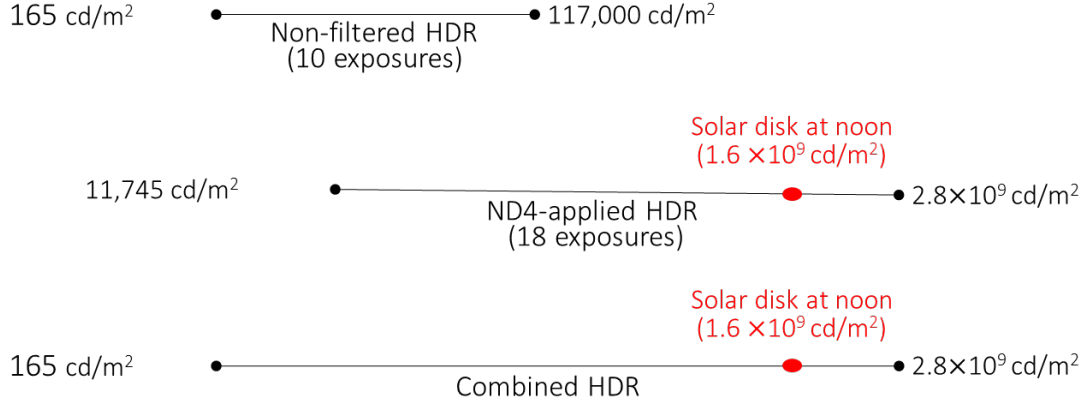


Figure 4.4 Measurable luminance range by fisheye-stereovision

### 4.3.2 Geometric calibration

Geometric calibration of fisheye-stereo estimates camera parameters that determine the 2D projection of real-world scenes into images. In the generic camera model [79] used in this paper (Figure 4.5), there are two types of parameters for each camera (intrinsic parameters  $K$  and distortion coefficients  $d$ ) and stereovision-specific extrinsic parameters  $[R|\vec{t}]$ . In the fisheye eye distortion model, the incoming ray of the scene,  $P$ , is refracted by a factor of  $\theta_d$  (a polynomial function of  $\theta$ ), where  $\theta$  is the angle between the camera principal axis and the incoming ray from the scene  $P$ . The intrinsic parameters  $K$  determine the pixel-scaling of the scene, skewness between the horizontal and vertical pixel array, and principal points (equivalent to fisheye distortion center). Extrinsic parameters  $[R|\vec{t}]$  are the rotation and translation between two camera frames constituting the stereovision. The calibration requires photographs of flat checkerboard patterns with a known square size, taken from many different views. 30 different image pairs were taken from 25.85mm-square checkerboards and put into an OpenCV implementation of fisheye-stereo calibration.

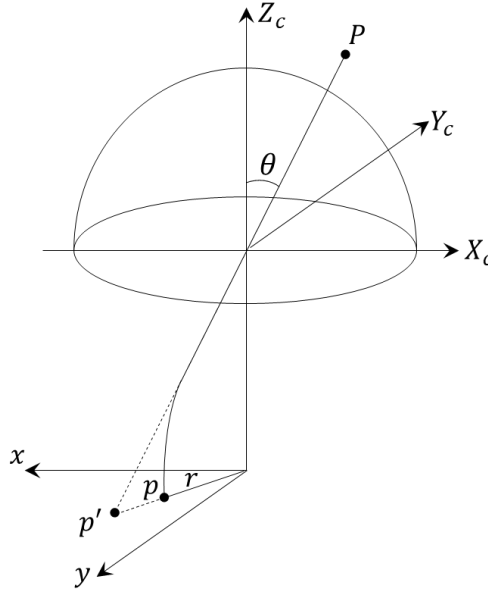


Figure 4.5 Generic fisheye camera model

#### 4.4 Positioning of glare sources

When the sensor identifies a bright source in the exterior exceeding a certain luminance threshold, its relative position to the camera can be estimated in 3D cartesian coordinates via triangulation. For the 3D positioning, the stereo-correspondence problem needs to be solved, referring to the task of finding a set of points in one image which can be identified as the same points in another image. One of the simplest and fastest methods of solving stereo-matching is template matching based on normalized cross-correlation (NCC). This method works well if the variance between corresponding pixels is low. However, there are several factors in fisheye-stereovision that can potentially create high variations within corresponding pixels; slightly different camera intrinsic parameters and fisheye distortion create different shapes and sizes of between the corresponding pixels. Also, mismatching can happen if multiple bright sources are present at the same time. A solution for the above issues is un-distortion and rectification of the fisheye-stereo images.

Correcting the fisheye distortion transforms a fisheye image into a distortion-free perspective image, where the straight lines in the real world remain straight. This can be done by back-projecting the pixels into rays and re-projecting them with any distortion-free perspective projection matrix. In the present study, the same perspective projection is used for both cameras

to make the un-distorted image have equal scaling and principal points, and zero-skewness. Stereo-rectification aligns the camera frames to have the parallel principal axis purely translated in a horizontal direction with the baseline distance. Rectification simplifies the stereo-matching because it makes corresponding epipolar lines to appear as horizontal lines at the same height in the stereo image pairs. Note that any non-occluded corresponding pixels between two images lie on corresponding epipolar lines, which is a stereovision characteristic as illustrated in Figure 4.6. In the rectified stereo image, the search space for template matching reduces into a single horizontal pixel array, at the same height of the template cropped from the image. In the present study, pixels above  $30,000 \text{ cd/m}^2$  are identified as a source of disability glare [81], although this threshold is not absolute. Both luminance maps were converted into binary mask assigning pixels above the threshold as 1 and 0 for the other pixels. Then pixels assigned with 1 were grouped by connected-components labeling with 2-connectivity (neighboring pixels in 8 directions are grouped together). From the labeled binary mask, the bounding boxes for grouped glare source pixels are formed allowing paddings in four directions. Templates for the glare sources were then cropped from the ND4-filtered image (left) using the bounding boxes. Then the NCC was computed along the scanline (corresponding epipolar line to the template) to find the matching point with highest NCC (Figure 4.7).

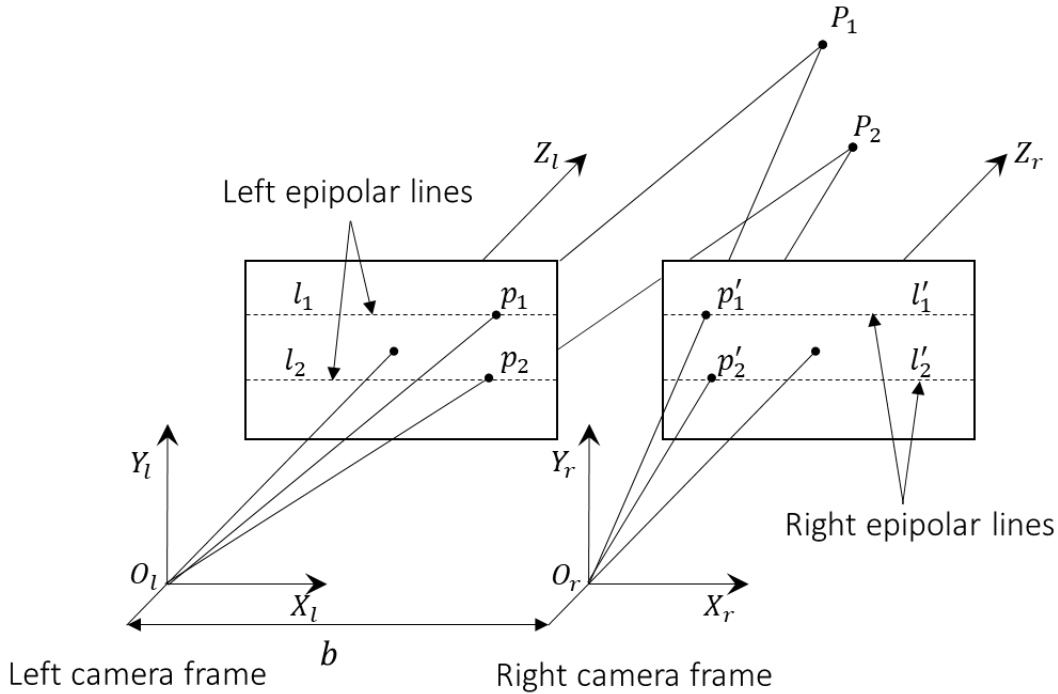


Figure 4.6 Epipolar lines in rectified stereo image pair

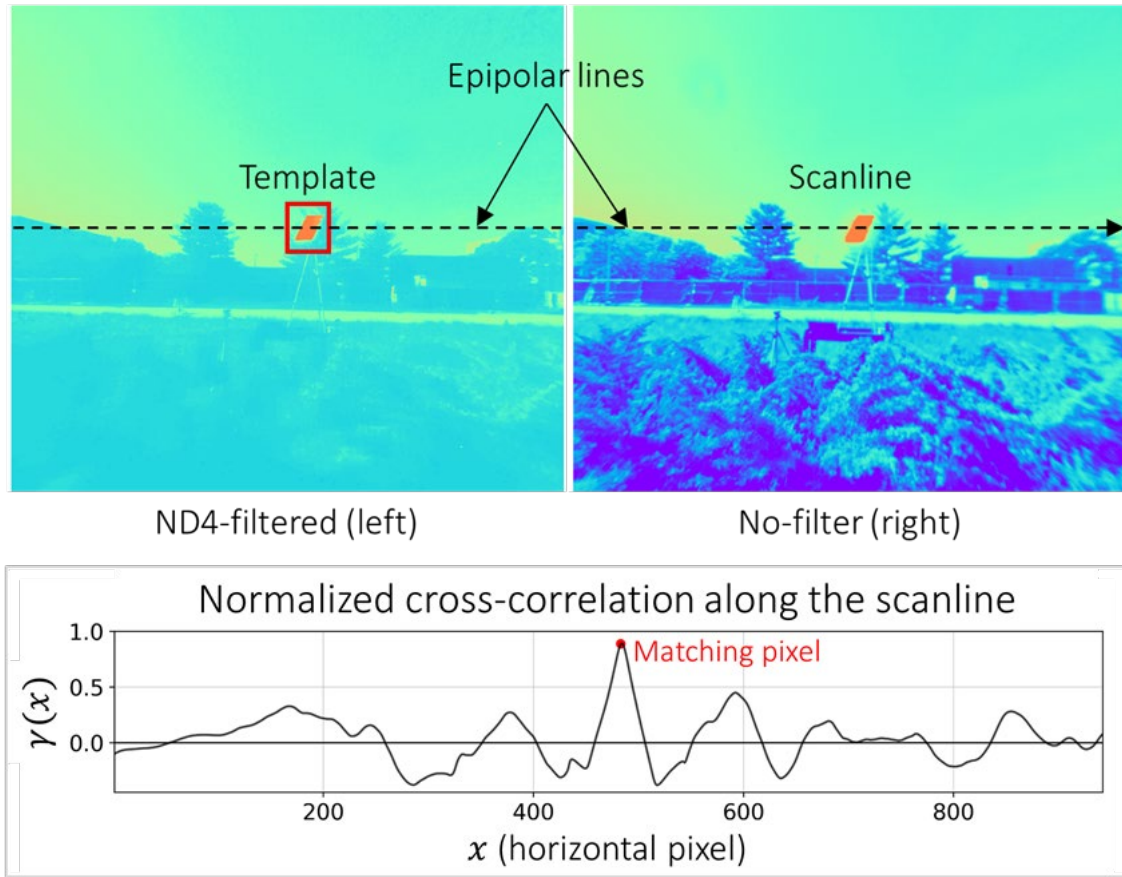


Figure 4.7 Template-matching in rectified stereo image pair

From the correspondence solved, estimation of the 3-D position of the scene is computed from disparity, the horizontal pixel difference between the corresponding pixels between two images (Figure 4.8). 3-D position of any corresponding pixel with disparity  $d$  can be estimated by Equations (4.1-4.3), where  $[X, Y, Z]$  are the 3-D coordinates of the corresponding scene in left-camera frame,  $x$  and  $y$  are pixel horizontal and vertical pixel displacement from the left-camera image's principal point,  $f$  is the focal length of the new camera projection,  $b$  is the baseline distance between two cameras, and  $d$  is the disparity between corresponding pixels.

$$Z = f \frac{b}{d} \quad (4.1)$$

$$X = x \frac{Z}{f} = x \frac{b}{d} \quad (4.2)$$

$$Y = y \frac{Z}{f} = y \frac{b}{d} \quad (4.3)$$



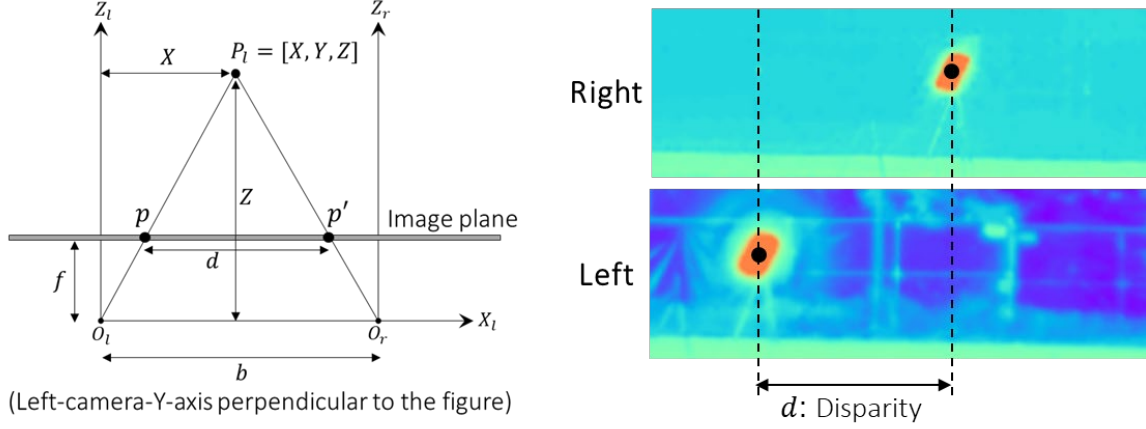


Figure 4.8 3D Positioning from the disparity

#### 4.5 Overflow correction for the solar disk

A correction of the solar disk pixels is required because of “overflow” problems. The basic idea of overflow correction is replacing overflown pixels of the non-filtered luminance map with corresponding pixels of the ND-filtered luminance map containing higher luminance values. Like 3D positioning, stereo-matching of the corresponding pixels is key to success. Finding correspondence for the solar disk can be simple for horizontal stereo images since image projection of the solar disk will be practically identical in the images due to its relatively infinite distance from the cameras. Assuming the intrinsic parameters of two cameras are identical and two camera frames are completely leveled, the solar disk will appear at exactly the same pixel coordinates away from the principal point of each image. The relative squared error (RSE) between pixel-scaling factors (intrinsic parameters), the distortion function  $\theta_d$  in  $[0, \pi/2]$ , and rotational matrix  $R$  and  $I_{3 \times 3}$  (identical camera angles) are extremely small ( $6.0E-0.5$ ,  $8.3E-5$ , and  $1.35E-5$  each). Thus, it can be safely assumed that the solar disk will appear at the same image coordinates if the principal points of the images are aligned, simplifying the template matching needless of undistortion and rectification. The overall overflow correction logic is as follows: 1) from the ND-filtered luminance map, detect the solar disk pixels using threshold of  $10^7$  cd/m<sup>2</sup>, determined by a cloud-covered reading from the luminance map; 2) extract the template from the pixels same as done in 3-D positioning; 3) compute NCC in a padded square pixel area centered at equal image coordinates of the template after aligning principal points of two images; and 4) find the pixel with the highest NCC and replace the overflown pixels with the template (Figure 4.9).



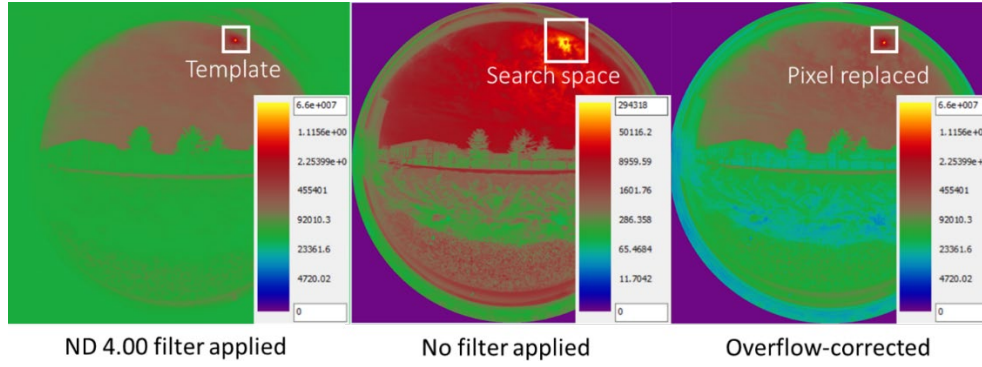


Figure 4.9 Overflow correction for solar disk pixels.

#### 4.6 Sensor validation

The 3-D positioning and complete HDR mapping with overflow correction were validated. The 3-D positioning was validated by comparing estimated stereo-depth to the known distance of an artificial glare source (reflector) from the window measured with a calibrated laser distance meter. The RRSE of estimated depth was 4.20% in 13 measurements ranging from 2~10 m (Figure 4.10).

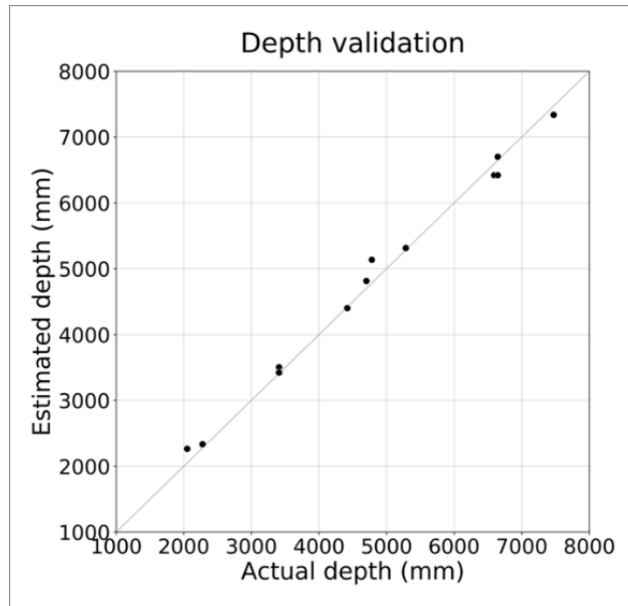


Figure 4.10 Stereo-depth validation

Since we are not able to directly measure the luminance of the sun, overflow correction was validated through vertical illuminance ( $E_v$ ) by integrating the pixel luminance with the configuration factor. The  $E_v$  calculated from the overflow-corrected luminance map was compared

to scientific-grade photometer readings, attached right next to the fisheye-stereovision sensor (Figure 4.3). Figure 4.11 presents comparison of  $E_v$  computed from pair of luminance maps before and after the overflow correction. The red markers in the scatter plot indicates the points from the original luminance map captured by non-filtered camera and the black markers connected to the red markers are corresponding values from the corrected luminance maps. In 44 points measured with sun in FOV, the overflow correction improved the accuracy significantly, reducing the RRSE from 43% to 5.2%.

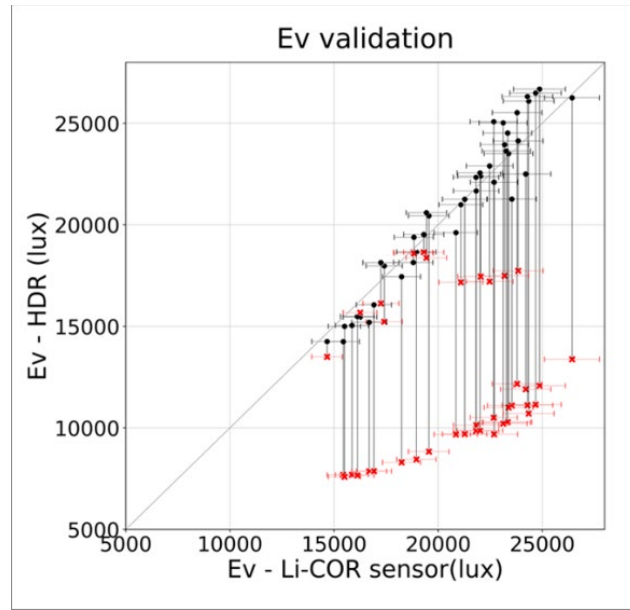


Figure 4.11 Vertical illuminance validation. Horizontal error bar shows measurement error ( $\pm 5\%$ ) for LI-COR photometer

## 4.7 Chapter discussion and conclusion

The proposed low-cost fisheye stereovision sensor can detect potential glare sources, locating them with reasonable accuracy in real time. Also, overflow correction of the solar disk pixels allows lowering the cost by using non-wide dynamic range image sensors and can replace conventional window photosensors while adding more capabilities. Future work includes examining and improving the robustness of the sensor in more challenging conditions, including positioning of highly slanted glare sources or handling cases where the number of detected glare sources is very high. The window-attached fisheye-stereovision sensor allows the implementation

of more advanced control algorithms with real-time glare source detection, location and intensity measurements, important for reliable daylight control operation and measurement-aided simulation. In addition, accurate luminance mapping can be used for visual preference-based modeling and control.

## **5. NON-INTRUSIVE LUMINANCE MONITORING FRAMEWORK VIA HIGH DYNAMIC RANGE IMAGING AND PHOTOGRAMMETRY**

### **5.1 Scope and objectives of the study**

This study proposes a novel, semi-automated framework for monitoring of luminance distribution within occupant-FOV, using a fisheye HDRI sensor installed at the non-intrusive position. The HDRI sensor can capture an accurate luminance map with proper calibration, including the photometric and geometric calibration. The 3D model of the room is automatically reconstructed through SfM-MVS photogrammetry pipeline combined by two open-libraries, COLMAP [146,159] and OpenMVS [160]. The occupants' head-poses are also estimated in the pipeline. The 3D context retrieved from the photogrammetry pipeline enables the back-projection of the luminance map captured by the HDRI sensor into 3D room surfaces which in turn re-projected into occupant-FOVs with their head poses estimated. The only commissioning effort is to capture a short video of the room and take photos from the occupant-views using readily-available camera devices, such as smartphones. The secondary contribution of this paper is the examination of an HDR imaging pipeline that adopts OpenCV-Python and custom Python scripts instead of using widely used HDRgen [74] and RADIANCE [66] commands.

### **5.2 Framework overview**

The overview of the proposed framework is as presented in Figure 5.1. Given a photometrically and geometrically calibrated camera sensor installed in a non-intrusive position in the room, the user is only required to capture two short videos and a single image per occupant (only the gray-shaded blocks in the diagram). The videos and the images can be captured with any video/image recordable devices such as smartphones. The rest of the framework process is fully automated, minimizing the commissioning effort.

One of the videos that capture a geometric calibration pattern will be used for automatic estimation of smartphone camera intrinsic parameters while the other one will be used to extract video frames for photogrammetry. Also, pictures taken from the occupant-head positions will be put into photogrammetry to estimate the virtual camera-poses corresponding to the occupant-FOVs.

Similarly, a picture taken from non-intrusive is also included in the photogrammetry to estimate the sensor-pose.

After pre-processing, the collected data and images are put into the photogrammetry pipeline combined by COLMAP and OpenMVS, which are publicly available 3D reconstruction libraries. The pipeline retrieves a 3D mesh model of the room as well as the estimated occupant and camera-sensor poses. By projecting the 3D model using the estimated camera-sensor pose and its intrinsic parameter, the room-depth perceived from the camera-sensor can be retrieved. Knowing the depth perceived from the camera-sensor allows to back-project the per-pixel luminance measured from HDR images into 3D space which can be re-projected into occupant FOV using the occupant-head pose previously estimated.

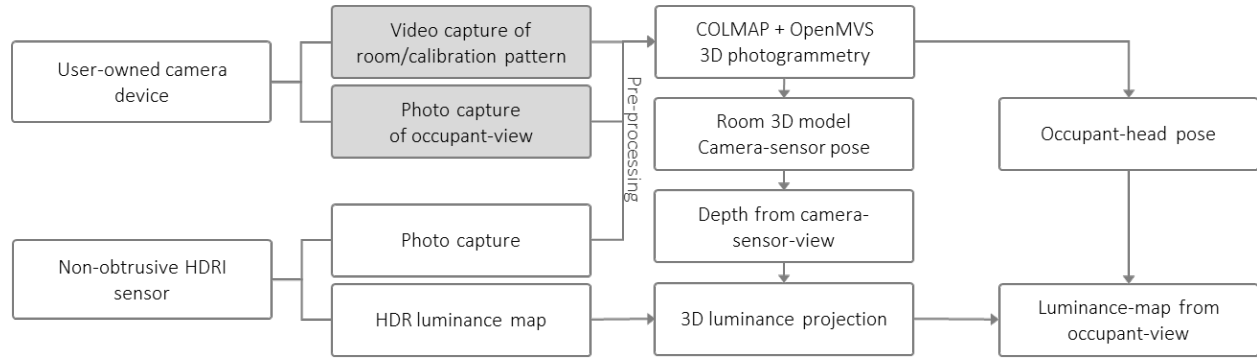


Figure 5.1 Overview of the proposed framework

### 5.3 Devices & calibration

As a high dynamic range imaging (HDRI) sensor, a low-cost camera board (Pi Camera) integrated into Raspberry Pi 3+ single board computer (Raspi) was used in the study [137]. The camera consists of an 8-megapixel CMOS sensor (Sony IMX2019) with maximum dynamic range of 44.56 dB. The operation of camera image-shooting is extensively configurable through its compatibility with Python language via Picamera library, enabling essential controls for HDR luminance map acquisition. The original lens of Picamera was replaced with a custom M12 fisheye lens available in the market that has f/1.8-aperture and 1.02mm-focal length. The expanded FOV through the lens is near 180-degrees that significantly widens the region captured from the sensor. As a video and image recording device, a smartphone (Samsung Galaxy A51) was used. It is worth noting that any video/image-recordable device can be used, as long as the captured videos and the

images share the same camera intrinsic parameters. The proposed framework assumes the installation of factory-calibrated HDRI sensor with well-estimated geometric/photometric parameters, while not requiring prior knowledge about the user-owned camera device for the enhanced scalability for real-building applications. However, for the better performance of photogrammetry, the intrinsic parameters of the device are recommended to be estimated. In this regard, a very simple geometric calibration procedure for the user-owned device was implemented in the framework.

### 5.3.1 Photometric calibration

Photometric calibration for HDRI sensor is a pre-requisite for reliable luminance measurement. Even though the overall photometric calibration process used in this study is very similar to the methods used in other visual comfort studies, this study adopts an alternative pipeline that is fully created in Python language (Figure 5.2). The main reason for the alteration is the speed improvement in HDR merging and vignetting correction.

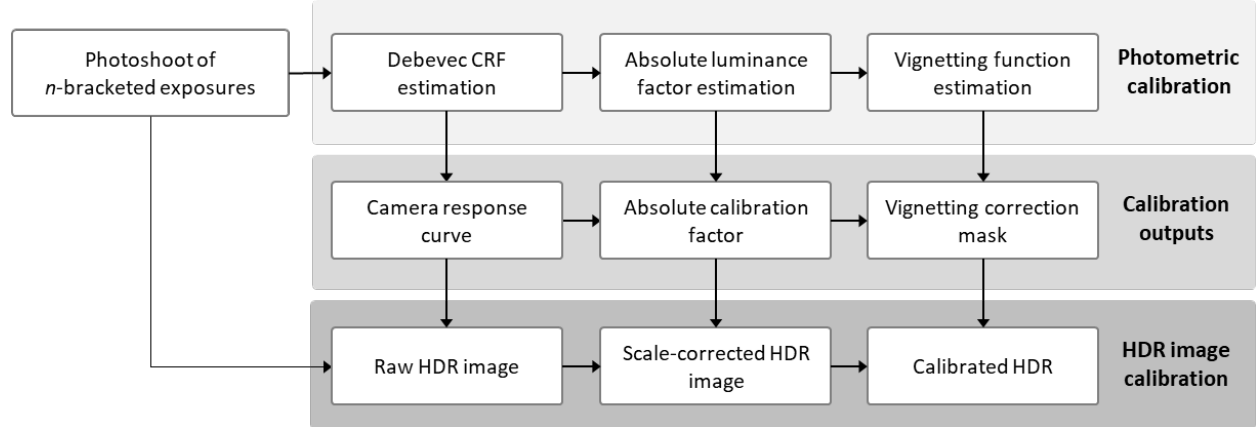


Figure 5.2 Photometric calibration for HDRI sensor

From the  $n$  low-dynamic images with different exposures (camera-shooting parameters for HDR creation is as in Table 2.1, camera response curve that associates the irradiance to the sensor-measured intensity (for each red/green/blue channel) is estimated via OpenCV-Python implementation of Debevec's algorithm [26]. The estimated camera response function of the HDRI

sensor is shown in Figure 5.3. An HDR image merged with the estimated CRF can be converted to a luminance map using the Eq. (5.1) as in (M. N. Inanici, 2006).

$$L = 179 * (0.2126 * R + 0.7152 * G + 0.0722 * B) \quad (5.1)$$

where  $L$ ,  $R$ ,  $G$  and  $B$  are the luminance ( $\text{cd/m}^2$ ) and RGB pixel values of the HDR image pixels.

Table 5.1 Camera settings for HDR image creation

ISO	100
Number of exposures	10
Shutter speed (microseconds)	9, 66, 236, 974, 3185, 12429, 33243 99823, 199749, 799906

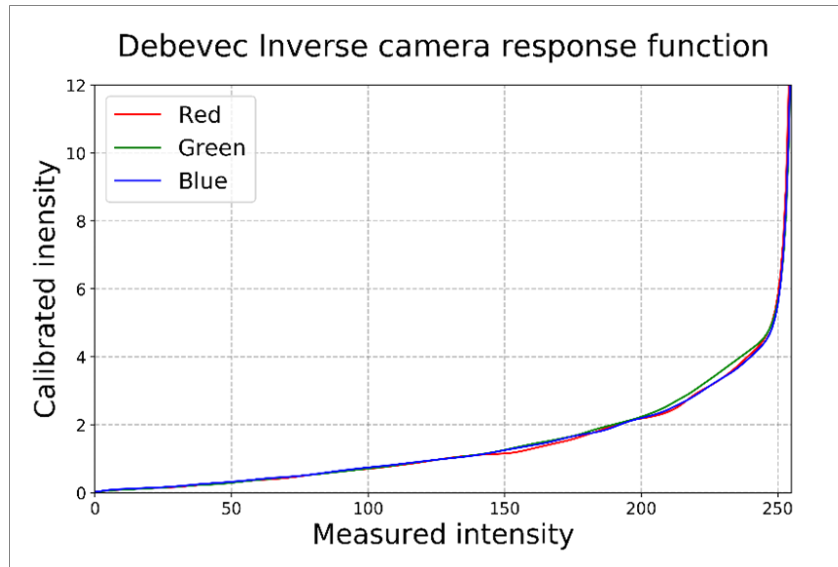


Figure 5.3 Estimated camera response function

By taking raw HDR images centered at neutral-colored surface and matching the surface's luminance measurement to the calibrated luminance spot-meter readings, the absolute calibration factor (multiplier that scales HDR intensities to match absolute luminance values) can be retrieved. A light gray-colored surface, 'Neutral 8' of X-Rite ColorChecker Classic calibration board [161] was measured for the calibration, as suggested by Safranek & Davis (2020). The reason for aiming the neutral surface at camera-optical-center is to avoid the error that can be induced by vignetting

effect on the pixels that are distant from the principal point, which is particularly pronounced in fisheye cameras with small apertures.

Vignetting effect also needs correction. The vignetting curve of the sensor was estimated following the procedure similar to [27]. It was estimated via polynomial fitting of nine luminance measurements of small, neutral-colored diffusive surface with  $0^\circ$  to  $84.375^\circ$  rotation with  $11.25^\circ$  increment ( $5.625^\circ$  for the last one), while the  $0^\circ$  degree rotated image was centered at the target surface. The curve was averaged by five different trials to reduce temporal and measurement errors. In lieu of RADIANCE pcomb command widely used for the vignetting correction in the literature, we created a per-pixel multiplier mask for the fisheye luminance map. The vignetting correction curve is computed by inverting the vignetting curve, and in turn vignetting-correcting multiplier for each pixel was stored in a single-channel array with the same size of the HDR image. Since this array-by-array multiplication does not require any further computation as pcomb that repeats normalization and calculation of multiplier for each pixel, the computation is much faster. The estimated vignetting curve and corresponding correction mask is presented in Figure 5.4.

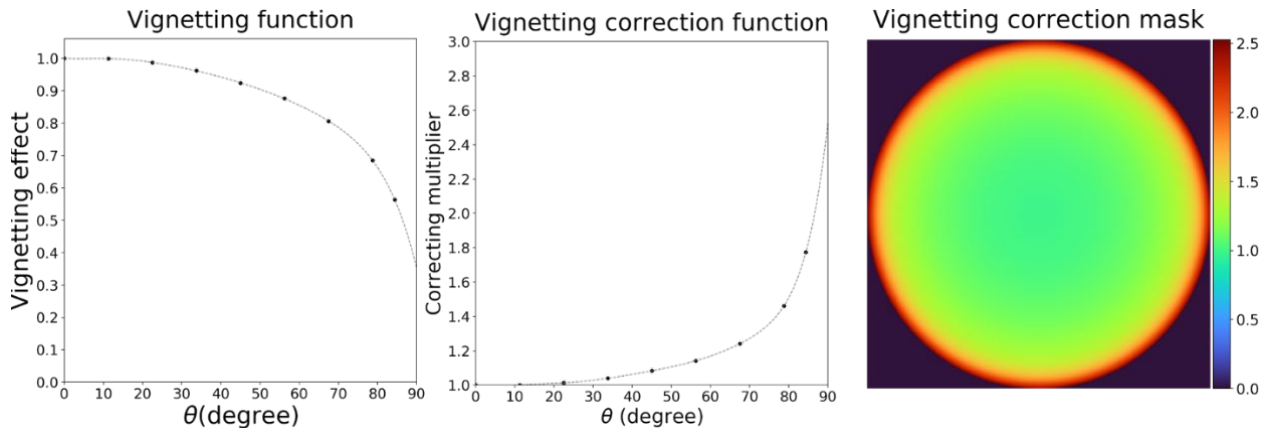


Figure 5.4 Vignetting curve (left). Vignetting correcting function (middle). Vignetting correcting mask (right)

### 5.3.2 Geometric calibration

Geometric calibration of camera estimates camera intrinsic parameters that includes focal length, principal points and radial distortion coefficients that determines real-world projection to the camera image. There are two major reasons for performing the geometric calibration: i) a fisheye image taken from the HDRI sensor needs rectification to be compatible with



photogrammetry pipeline (COLMAP) used in this study; ii) for both HDRI camera and user-owned camera images, knowing the accurate intrinsic parameter accelerates the speed of 3-D reconstruction by bypassing the self-refinement of camera intrinsic parameters during the SfM sparse reconstruction; and iii) if the user prefers to scale the 3-D model to the actual size (in metric system), geometric calibration is necessary.

The high-degree-distortion of fisheye HDRI sensor requires geometric calibration with specific model assumption other than typical camera devices with low-to-moderate distortion. Also, fisheye cameras require careful attention when capturing calibration pattern for the calibration for the same reason. Thus, the calibration of fisheye HDRI and user-owned camera followed different procedure.

Geometric calibration either for fisheye camera or more generic camera model implemented in OpenCV-Python performs the following process: i) take photoshoots of a calibration pattern (a checker board with known square-size) from various views; ii) detect checkboard corners from the images taken; iii) iteratively refine camera intrinsic parameters and extrinsic parameters relative to the checkboard until convergence. This is done by non-linear minimization of re-projection error, based on the estimated intrinsic and extrinsic parameters and the camera model assumed. The outputs of the calibration are intrinsic parameter  $K$ , and model-specific distortion coefficients  $d$ .

For the fisheye HDRI sensor calibration, calibration pattern needs to be shot with caution to ensure the images cover the various regions of the image thus radial distortion can be accurately estimated. Also since typical camera models do not suit fisheye camera calibration due to the high distortion, OpenCV-Python implementation of Kannala and Brandts' generic camera model designed for wide-angle and fisheye camera was used [79]. In contrast, typical camera devices such as smartphone cameras do not have serious distortion even with the state-of-the-art wide-angle-capture modes these days. Thus, it is sufficient to simply take a short video of calibration pattern (less than 10 seconds) and use the video frames extracted for the calibration. Also, OpenCV-Python camera calibration based on Zhang's algorithm [163] which suffices typical low-distortion cameras, was used (Figure 5.5).

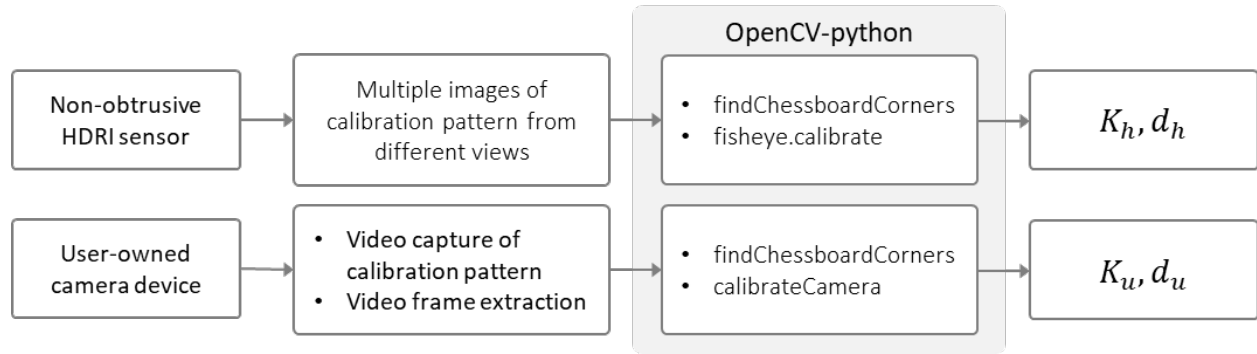


Figure 5.5 Geometric calibration for HDRI sensor and user-owned camera device

Geometric parameters estimated can be used for rectifying the camera images into distortion-free, rectilinear images where the straight elements appear straight. OpenCV-Python functions named `initUndistortRectifyMap` and `remap` allows remapping the images with radial distortion into rectilinear images with arbitrary intrinsic parameters and image-resolution, which are also input parameters along with the estimated camera parameters. This enables the use of any type of camera device for the photogrammetry because the input images can be projected in any desired projection regardless of its original intrinsic characteristics. Figure 5.6 shows an example of fisheye image rectification that preserves the original focal length and the image resolution.



Figure 5.6 Intrinsic-preserving fisheye rectification example

## 5.4 Data collection and preprocessing

### 5.4.1 Video and image collection

As described in Section 5.2, the user who manages the framework only need to take two short videos and photos from the occupant-eye positions. One of the video is for the geometric calibration (Video A) of the user-owned camera, capturing a calibration pattern described in Section 5.3.2 from with various poses. The calibration pattern used in this study is a checkerboard pattern on a flat, planar surface and with a known square-size. A simple method to do this is taking a video of a calibration pattern image displayed on a computer while moving the camera around it screen. The user can easily measure the square size of the checkerboard using a ruler (Figure 5.7). Regardless of several factors, video-length shorter than 20 seconds may be suitable for its purpose.

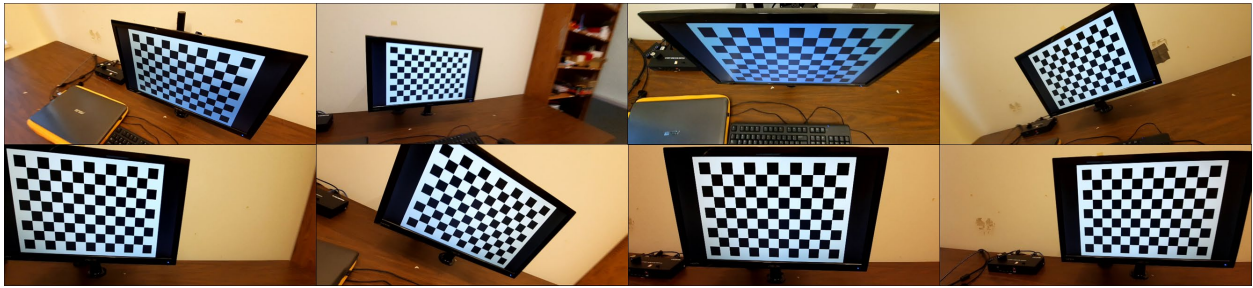


Figure 5.7 Example video frames extracted from Video A

The other video (Video B) needs to capture the entire room, including the same calibration pattern captured in the geometric calibration video. The quality of reconstructed model through photogrammetry largely relies on the manner that the video is taken. In brief, it is recommended to capture the images of the same object in as many view-angles as possible and to capture the same region-of-interest in smaller resolution for the robust model reconstruction (wide-angle mode is preferred for smartphones). While taking the video, the calibration pattern needs to be conducted with caution since it is desired to capture at least three but preferably greater number of frames. The reason for doing this is to rescale to reconstructed 3D model to the actual size, using the camera translation relative to the calibration pattern. The detail is elaborated in the next paragraph. There is no golden rule to decide the video length since it depends on multiple factors such as the room-characteristics, speed of the camera-movement and the frame extraction interval.

Also, an image is taken with the fisheye HDRI sensor installed in a fixed position determined by the user. The factors to be considered for the sensor placement are i) non-intrusiveness: the sensor needs certain level of distance from the office workers to avoid distraction; ii) occlusion-avoidance: potential obstructions such as from the room furniture, building components, or even occupant-bodies should be avoided; iii) view-correspondence: to capture the 3D scene surrounding the occupant as much as possible, sensor-pose needs a certain degree of alignment. The lateral translation of the sensor respect to the occupant's head needs to be limited. Also, the rotation between the sensor and the occupant-view should be constrained to reduce the re-projection error of luminance between different views, and to enable capturing of wider region-of-interest that corresponds to the user's FOV. Regarding this factors, it is advisable to install the camera at certain height above the occupants high enough to avoid distraction and occlusion, oriented similar to the occupant-eyes consistent with findings in [47] - where the ceiling-mounted camera exhibited higher correlation to the occupant-perceived luminance distribution with smaller angle difference.

#### 5.4.2 Data pre-processing

After the video-recordings, their frames are extracted with pre-defined frame-interval. The frames extracted from the calibration-purpose video are fed into OpenCV-calibration as described in Section 5.3.2. Output of calibration are intrinsic parameters and distortion coefficients of the user-owned device ( $K_u$  and  $d_u$ ). These parameters are then used to rectify the frames from the video capturing the room. As described in Section 5.3.2, the user can define the desired intrinsic parameters and the resolution of the rectified images. In this study, we rectified images using pinhole projection choosing the radial focal length as the estimated horizontal focal length of the camera preserving the image resolution and principal points (generally the image center) as the original. Reducing the focal length or image resolution can be viable options for speed acceleration or quality enhancement of the 3D reconstruction, while the choice will depend on the room characteristics, computation power, and user-needs. Rectified video frame examples are shown in Figure 5.8.



Figure 5.8 Rectified video frames example extracted from Video B

After rectifying the images, the rectified images that captures the calibration pattern from Video B are in turn put into re-calibration of camera intrinsic parameters defined previously. The reason for the recalibration is to not only to refine the camera intrinsic parameters but mainly to estimate the translational vectors (in 3D-cartesian-coordinates relative to the calibration pattern) from those images which are extra outputs of the `calibrateCamera` function described in Section 5.3.2. The list of the estimated translations is stored in a text file along with the corresponding image file path in ‘file-path, X, Y, Z’ format (Figure 5.9) for the geo-registration using COLMAP `model_aligner` command described in Section 5.5.1.

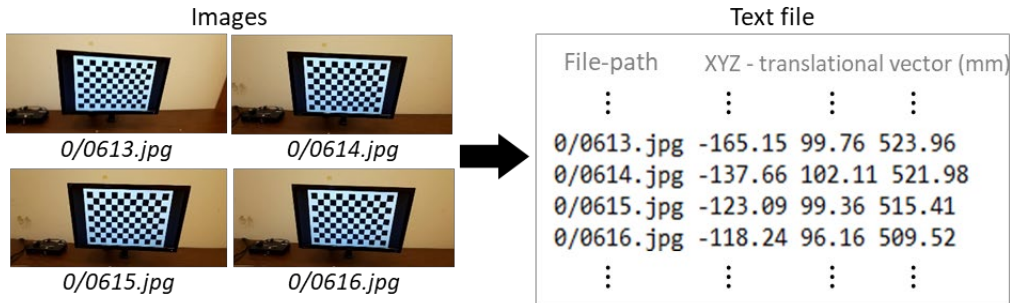


Figure 5.9 Text file creation for camera translation vectors

## 5.5 Photogrammetry task pipeline

The overview of photogrammetry pipeline is as illustrated in Figure 5.10. The inputs to the pipeline are: i) rectified images taken from all camera devices used; and ii) their geometric parameters calibrated. The major building blocks of the photogrammetry pipeline are COLMAP and OpenMVS that sequentially performs sparse reconstruction and dense reconstruction/mesh-creation, respectively. The major reason for using the hybrid pipeline is because COLMAP-OpenMVS combination has exhibited accuracy and robustness with reasonable computation speed

in their comparative studies [149,164]. The sparse reconstruction through COLMAP SfM reconstructs only the interest points (SIFT features) that can be mutually found in different pairs of images. Since only the small number of view-invariant pixels are identified for the reconstruction, robust estimation of image-corresponding camera poses is possible through a RANSAC-based (Random Sample Consensus) algorithm and non-linear optimization. Thus, it is possible to estimate camera poses of specific images to retrieve camera poses from occupant-view or the HDRI-sensor-view. However, the 3D model reconstructed from SfM lacks completeness required for the re-projection of occupant-views.

Thus, the resulting sparse model from COLMAP SfM is densified via OpenMVS to reconstruct a dense point cloud which is in turn transformed to a triangle-mesh model. COLMAP allows seamless integration with OpenMVS by conversion of its output into a compatible format. Thus, the outputs from photogrammetry pipeline are camera poses correspond to HDRI sensor and the occupant-views and the refined mesh model of the room.

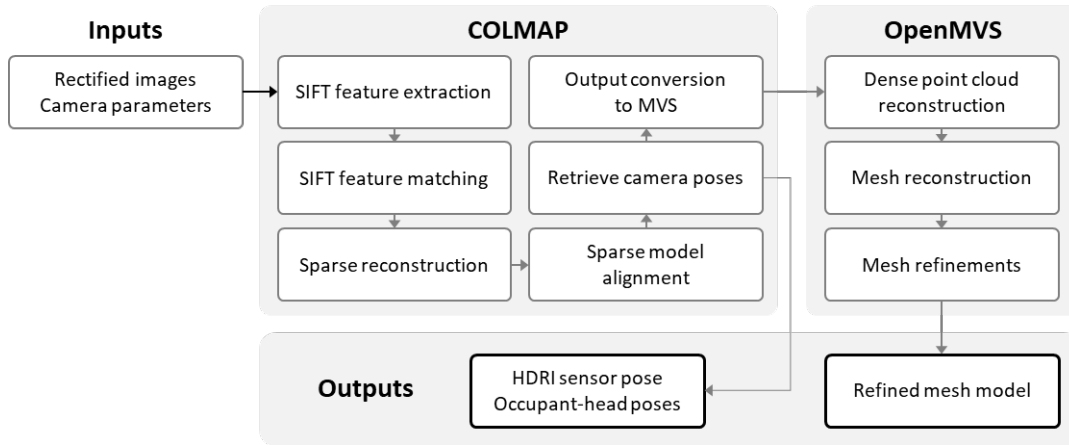


Figure 5.10 Overview of photogrammetry task pipeline

### 5.5.1 COLMAP sparse model reconstruction

COLMAP is a general-purpose SfM-MVS pipeline available with GUI and command-line feature that enables seamless integration to Python scripts for an automated pipeline. Its robustness, scalability and accuracy essential for such general-purpose method were validated in literature [146,149,164]. In the proposed framework, COLMAP commands were used to reconstruct and

post-process the sparse model of the room, and to retrieve camera poses of interest (occupant-head and fisheye HDRI sensor).

The initial inputs of the COLMAP pipeline are the image file paths of the rectified images and the estimated camera parameters. COLMAP commands feature extractor and exhaustive matcher extract SIFT (scale-invariant feature transform) features and find matches them between the entire image-pairs. The COLMAP mapper command performs the SfM sparse model reconstruction, that sequentially grows 3D model from SIFT key-point pixels with iterative refinement of camera poses and points reconstructed in 3D. Figure 5.11 is an example of reconstructed sparse model rendered in COLMAP-GUI. The red-pyramid markers refer to the camera poses for the images, while the pop-up window is displaying the information of a specific view circled. As shown in the window, the rotation and the translation of the camera are stored in quaternion ( $q_w, q_x, q_y, q_z$ ) and 3D Cartesian ( $t_x, t_y, t_z$ ) formats, which will be further utilized in luminance re-projection.

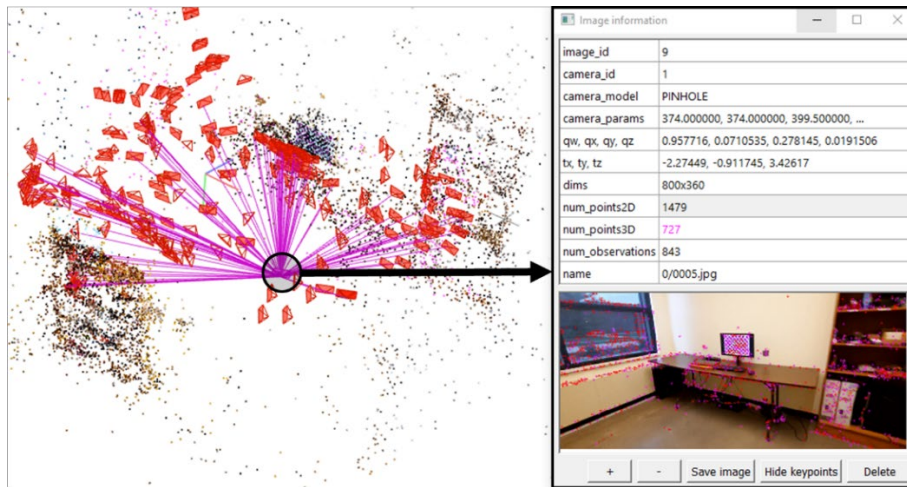


Figure 5.11 Example sparse reconstruction rendered in COLMAP-GUI

The main outputs of COLMAP sparse reconstruction are three binary files ('cameras.bin', 'images.bin', 'points3D.bin') that store lists of geometric parameters of the cameras used, camera pose and projected 2D pixels per-image, and reconstructed 3D points. The reconstructed sparse model is then geo-registered via COLMAP model\_aligner command. Geo-registration refers to scaling and alignment the of the model to using known camera positions that can be estimated



through re-calibration process described in Section 5.4.2. The text file which contains image file-paths and their estimated camera translations through the camera re-calibration is the input to the geo-registration, while the output is new binary files with the aligned model.

To convert the binary-encoded output files into more accessible text format and to OpenMVS-compatible nvm file format, COLMAP `model_converter` was used. By converting ‘images.bin’ file to a text file, camera rotation and translational vectors can be easily accessed. Also, the sparse model reconstructed converted into nvm can be converted to mvs extension for OpenMVS pipeline as described in following Section 5.5.2. The underlying theories and background for the COLMAP SfM pipeline are detailed in [146].

### **5.5.2 OpenMVS dense point cloud & mesh reconstruction**

OpenMVS is a computer-vision library particularly targeted for MVS reconstruction complementary to other SfM pipelines such as OpenMVG [165] or COLMAP. OpenMVS provides a set of algorithms to recover the full surface of the scene from the sparse model and camera poses recovered from the SfM pipeline. Four OpenMVS commands, `InterfaceVisualSFM`, `DensifyPointCloud`, `ReconstructMesh`, and `RefineMesh` are implemented in the photogrammetry pipeline.

`InterfaceVisualSFM` converts nvm sparse model input to mvs format that is compatible to OpenMVS 3D reconstruction modules. `DensifyPointCloud` reconstructs a dense point cloud through a Patch-Match Stereo (PMS) algorithm based on [166]. The PMS algorithm retrieves depth maps from the entire set of images and fuses them by back-projecting the filtered points meeting certain criteria (such as number of views agreed on a pixel or re-projected error of a 3D point). From the dense point cloud, a triangle mesh model is created and then refined via `ReconstructMesh` and `RefineMesh` modules. Mesh modeling is useful since the mesh has a form of connected surfaces rather than a group of points thus has higher completeness. It offers hole-filling and smoothing features for weakly or sparsely reconstructed regions of the dense point cloud. Also, depth map projected into a certain view will be completely filled with per-pixel depth since the points lying on the triangular surfaces can fill the entire depth map pixels regardless of the number of vertices in the mesh, which is not the case for the point cloud depth projection



(RGB projections and depth maps from reconstructed 3D models). The rendered example of 3D textured mesh of a room is presented in Figure 5.12.

Table 5.2 RGB projections and depth maps from reconstructed 3D models


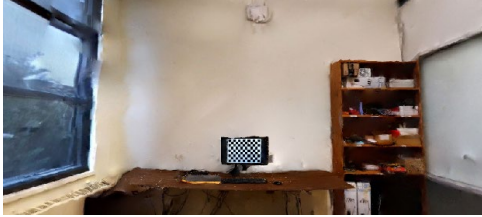
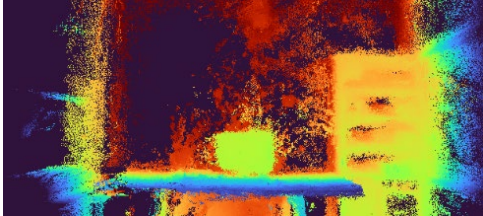
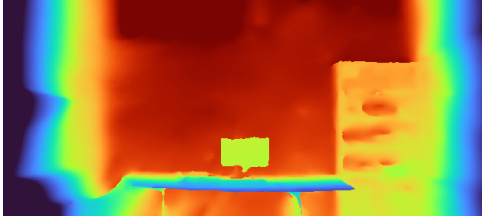
	Point cloud model	Mesh model
RGB projection		
Depth map		



Figure 5.12 Rendered views of textured mesh model

## 5.6 Luminance re-projection

In brief, the re-projection of luminance distribution is done by reconstructing a luminance-mapped mesh model from the HDRI sensor measurement and re-projecting it into an occupants' FOV. The overall sequence of the re-projection process is shown in Figure 5.13. Using the mesh model of the room and extrinsic and user-defined intrinsic parameters of the HDRI sensor, a depth map of the room can be captured from the HDRI sensor position. Since the depth map is aligned with rectified luminance maps captured by the sensor, they can be merged together to compose RGBD images (which contain per-pixel color and depth information). The RGBD images can be

re-projected into the 3D point cloud, then transformed to mesh model. The newly reconstructed mesh model can be re-projected to a view corresponding to the occupants' FOV using the previously retrieved occupant head poses and camera intrinsic parameters  $K_o$ . The entire process is elaborated in the rest of this section.

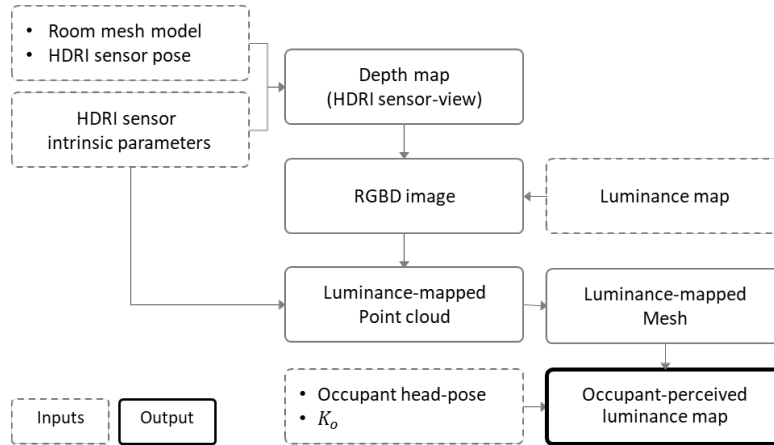


Figure 5.13 Luminance re-projection pipeline

The major building blocks in the luminance re-projection process make extensive use of Open3D-Python [167], an open-source library for processing and visualizing 3D geometries based on C++ with Python-bindings. The first block of the re-projection pipeline is creating a depth map using an Open3D function (*visualization.capture\_depth\_float\_buffer*). As shown in Figure 5.14, Open3D allows capturing the 2D texture and depth map observed from a specific camera defined by the user. Thus, the intrinsic and extrinsic parameters of the HDRI sensor, estimated in the earlier stages, can be used to capture the depth map as perceived by the sensor.

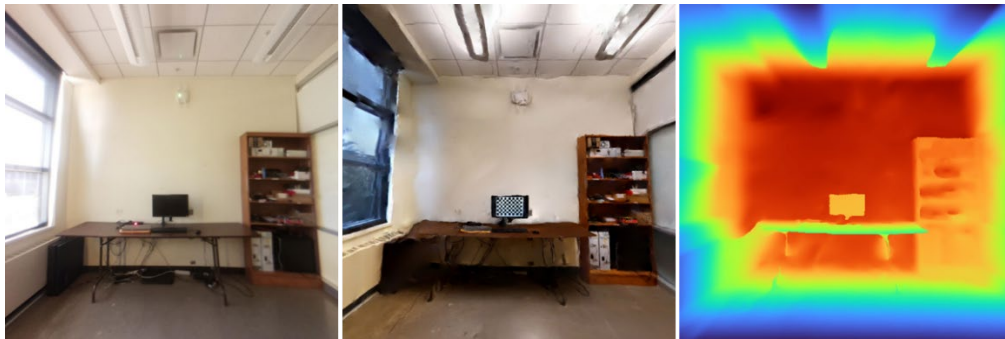




Figure 5.14 Left: Rectified LDR image captured by HDRI sensor; Middle: Mesh projection into 3-channel texture map; Right: Mesh projection into single channel depth map

The current distribution of Open3D (0.9.0) limits the range 2D and 3D-projectable FOV in horizontal and vertical direction to only 90 degrees. This means that the depth maps recovered from the mesh model can only capture 90-degree-FOV; for the re-projected occupant view, this may not be sufficient. Thus, the original C++ source of the Open3D 0.9.0 was modified to remove the FOV constraint that enables smaller focal length within the same image resolution, allowing projection far greater than 90 degrees. Table 5.3 shows an example of 2D projections using the original and modified Open3D visualization modules.

Table 5.3 2D projections before and after Open3D modification.

	Original Open3D	Modified Open3D
2D projection		
FOV	90 degrees (Maximum)	136 degrees

The estimated depth map is then merged with a rectified luminance map from the HDRI sensor to create a 4-channel RGBD image. The pixel values for RGB channels are filled with log-normalized luminance values into  $[0,1]$  range which can be inverted back into the original luminance range. An example of false-color-mapped luminance map with log-normalization is presented in Figure 5.15 - left. A color map named ‘*Turbo*’ was used in this paper for intuitive false-color representation of the luminance distributions in 2D luminance maps and 3D luminance projections [168]. The RGBD map is projected into a 3D point cloud using the sensor’s intrinsic parameters. This is in turn converted into a mesh model (Figure 5.15 - middle/right) to avoid sparse regions when projected into 2D occupant views, as described in Section 5.5.2. The luminance values of the surface points are interpolated by the vertices of the triangles they are lying on. These

will reasonably approximate the real values unless the weakly constructed region contains abrupt luminance variation patterns, such as specular reflections or bright light sources.

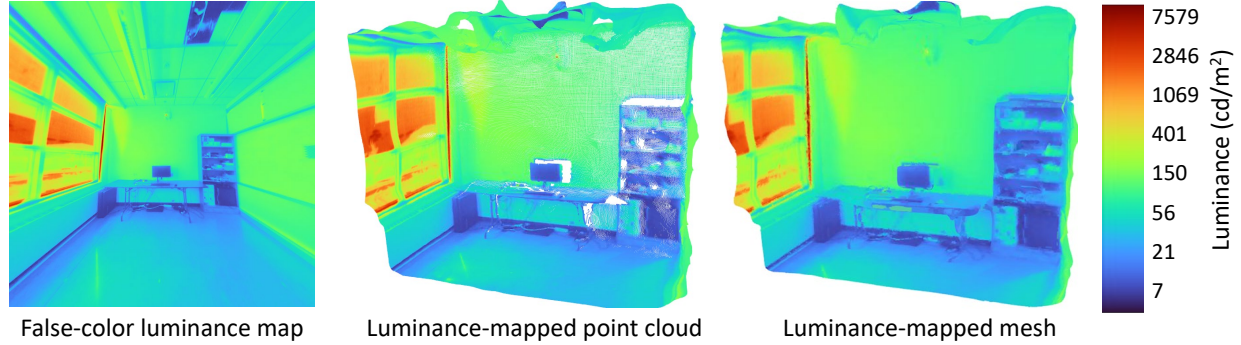


Figure 5.15 Luminance map re-projection

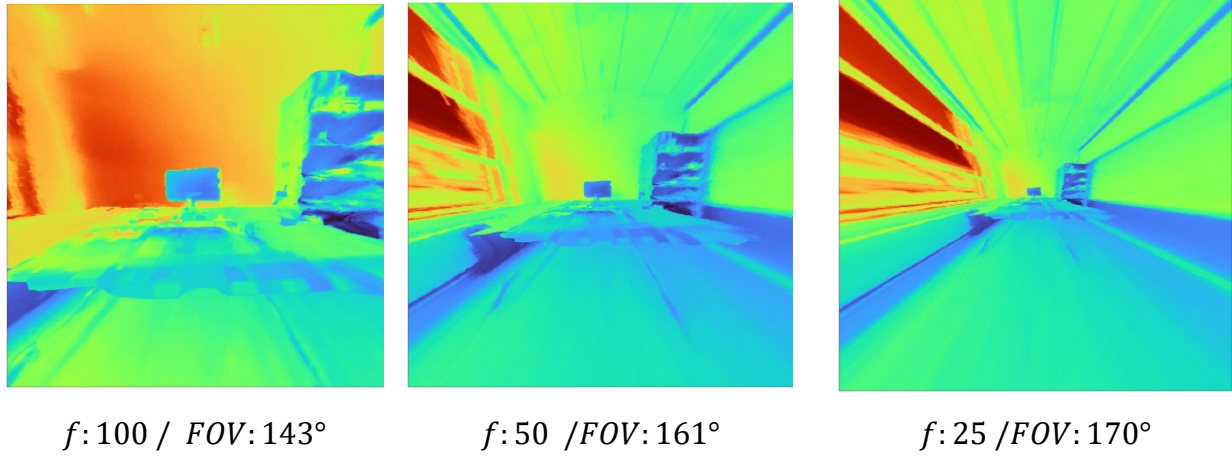
The luminance-mapped mesh can be pinhole-projected into occupant FOV given the camera extrinsic and intrinsic parameters that correspond to occupants' eyes (requires inverse rotation and translation relative to the HDRI sensor pose). The extrinsic parameters already retrieved in the SfM sparse reconstruction (Section 5.5.1) need to be re-aligned to the HDRI sensor-pose, since the back-projected mesh model is centered to the HDRI sensor, different from the original mesh model reconstructed in Section 5.5.2. On the other hand, the intrinsic parameters including the focal length, principal points and image resolution depend on the user's choice. Choosing a small focal length relative to the image resolution is advisable to capture a wider FOV similar to the fisheye cameras. Reducing the focal length lowers the quality of pixels, particularly around the principal point. On the other hand, increasing the image resolution multiplies the computational cost. Therefore, the trade-off between the maximum FOV, image quality and the computation speed needs to be considered (Table 5.4) in this process if optimal results are desired. The maximum horizontal and vertical FOV of the square pinhole-camera image can be calculated using Equation 5.1.

$$\text{FOV} = 2 * \arctan \frac{W}{2f} \quad (5.1)$$

where  $w$  is the horizontal and vertical resolution of the image, and  $f$  is the focal length of the pinhole camera.



Table 5.4 Pinhole-projected images with varying focal lengths



Even though the pinhole re-projection of luminance distribution can cover the occupant FOV, it is transformed into a fisheye image for a practical reason. Since most human visual comfort studies leveraging HDRI techniques have been using wide-angle fisheye cameras to fully capture human-FOV, visual comfort analysis tools such as *Evalglare* [65] were developed with fisheye-image compatibility. To utilize *Evalglare* for future implementation and experimental validation in this study, the pinhole luminance map was transformed to an equidistant fisheye luminance map. The mathematical representation of pinhole and equidistant fisheye map is listed in Table 5.5.

Table 5.5 Mathematical representations of camera projections used

Projection	Mathematical representation
Pinhole (Rectilinear)	$R = f \cdot \tan \theta$
Equidistant-fisheye	$R = f \cdot \theta$

where  $R$  is pixel distance from the image principal point and  $\theta$  is the angle between the principal axis and the ray emanated from the camera center to the real-world scene corresponding to the pixel. The logic for fisheye transformation is shown in Table 5.6.

Table 5.6 Equidistant fisheye projection pseudo-algorithm

- 
1. Initialize a zero-filled  $N \times N$  single-channel array  $L$
  2. **FOR** each  $i$ -th pixel in vertical direction
  3.     **FOR** each  $j$ -th pixel in horizontal direction
  4.         **IF**  $\frac{R_{i,j}}{N} < 0.5$  **THEN**
  5.             Compute  $\theta_{i,j}$  (using the equation in Table 6.3)
  6.             Replace  $L_{i,j}$  with luminance in the pinhole-image pixel corresponding to  $\theta_{i,j}$  (nearest-neighbor sampling)
  7.         **END IF**
  8.     **END**
  9. **END**
- 

Figure 5.16 shows a comparison of camera-captured and re-projected fisheye luminance mapping from the occupants' FOV using a false-color representation, at two different times with slightly different luminance conditions. The FOV is re-projected nicely using the developed method, and the re-projected luminance values show reasonable agreement with the measured ones. A more detailed experimental evaluation of the method and validation of its accuracy is presented next.

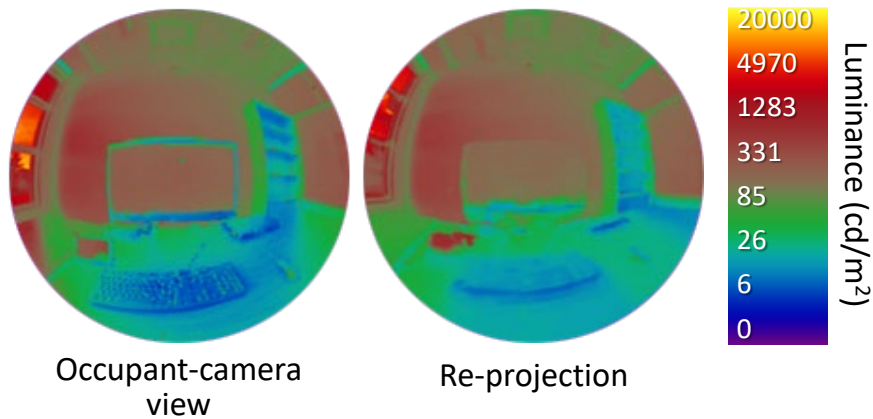


Figure 5.16 Equidistant-fisheye luminance maps (occupant camera-captured vs. re-projected)

## 5.7 Implementation of non-intrusive luminance monitoring framework and experimental performance evaluation

The proposed non-intrusive luminance monitoring framework was implemented in a side-lit, private office. The re-projected luminance maps into the occupant FOV were compared with the respective real measurements taken from the occupant position, under various interior luminance distributions, to validate the method and evaluate its performance. Three distinct quantitative measures were selected for comparative evaluation and validation of the developed framework: Daylight Glare Probability (DGP), average luminance of the scene ( $L_{avg}$ ), and vertical illuminance on the eye ( $E_v$ ). These have showed robustness in performance as visual discomfort predictors in a recent cross-validation study [169], compared to several other metrics. The basic experiment included a fixed shading position and more “standard” conditions, while additional experiments were conducted under excessive brightness scenarios to examine potential errors associated with those cases.

### 5.7.1 Experimental setup

The proposed framework was implemented in a 3.2 m × 4.0 m × 3.2 m high private office in West Lafayette, Indiana (40°25'N, 86°55'W) with a south-facing façade. The façade consists of aluminum curtain wall framing and a high-performance glazing unit (normal  $T_v = 64\%$ ) with a window-to-wall ratio of 0.54. The room is equipped with interior dark-colored motorized roller shades (normal  $T_v = 2.53\%$  and  $OF = 2.18\%$ ). These represent common options in modern office buildings.

The experimental setup and layout is shown in Figure 5.17 and Figure 5.18. The room has a typical side-lit layout where the occupant is seated parallel to the window and 2.5 m away from it (facing west with limited direct window view). This was done on purpose to minimize the effects of high brightness and glare, which were examined separately later on. It is also a common scenario in single-occupancy offices. The occupant was assumed to be looking towards a computer screen 0.6 m away (typical office work). Note that the surface of the desk had a specular reflectivity thus it can create reflections that will cause glare when exposed to direct sunlight.

Two calibrated HDRI sensors were installed at different positions: Sensor I served as the non-intrusive luminance measurement sensor, vertically attached to the wall behind the occupant position at 2 m from the floor, facing 20 degrees downward; and Sensor II was installed at the

occupant eye-position (1.2 m above the floor looking towards the computer screen) for simultaneous comparison with Sensor I and overall evaluation of the method. Each of the sensors was connected to a single Raspberry Pi, where the collected luminance maps are stored during the experiment. The post-processing including the re-projection pipeline of the luminance maps and analysis of the collected luminance maps were performed on a separate desktop computer. The purpose of the experimental evaluation was to assess the performance of the method and compare the consistency of re-projected vs. actual luminance maps under various luminance distributions.

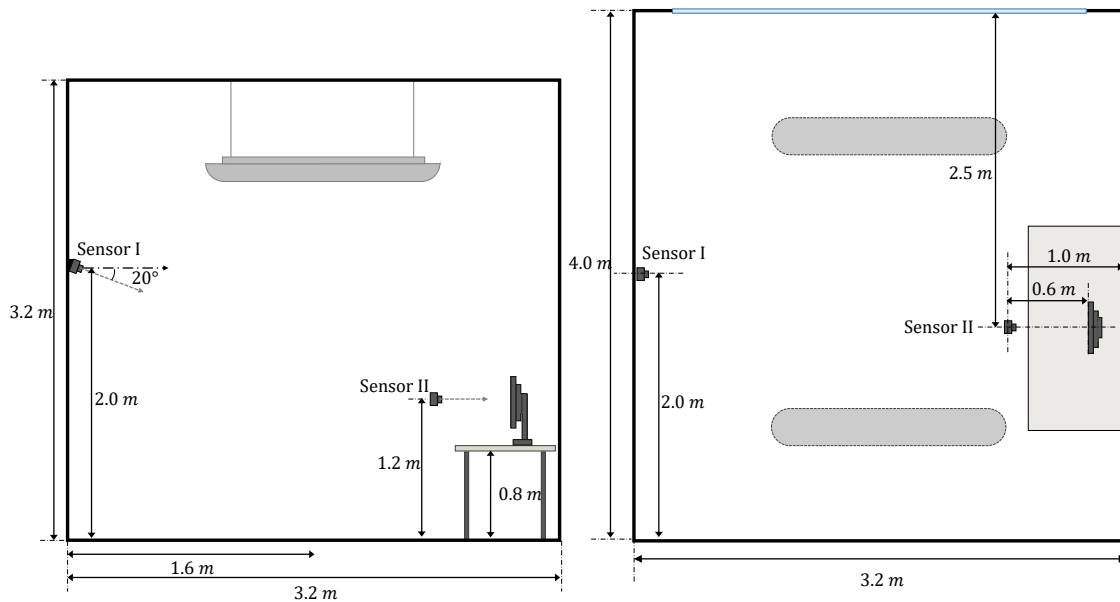


Figure 5.17 Instrumentation and space layout for Experiment I (left: side view; right: top view)

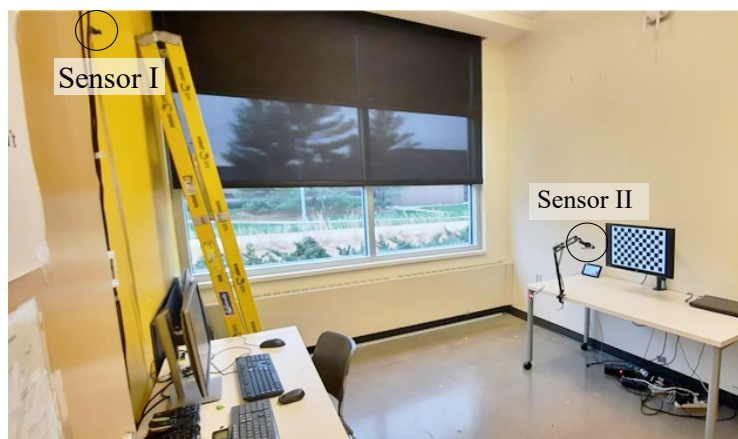


Figure 5.18 Interior view of test office with two camera sensors installed



### 5.7.2 Experimental procedure, data analysis and performance evaluation

The re-projected luminance maps of the occupant FOV, measured from Sensor I, were collected and compared with the luminance maps from the actual occupant position (Sensor II). The two HDRI sensors were synchronized and captured luminance maps every 10 minutes. For the basic experiment, the roller shades were kept at 35% open (a bit above eye height) under sunny days to mimic realistic conditions in office spaces with daylight provision –occupants or the control system will control shades to reduce glare but allow some outside view; this usually happens around the eye height. More shade positions were examined to study high brightness scenarios as discussed later. The experiment was performed in sunny days of winter (November - December 2020), where the average horizontal irradiance at midday was around  $485 \text{ W/m}^2$ . A total number of 287 points were collected.

Daylight Glare Probability (DGP), average luminance of the scene ( $L_{avg}$ ), and vertical illuminance on the eye ( $E_v$ ) were systematically compared. All the indicators were computed via Evalglare, where, for glare source detection, a multiplier of 4 of task zone luminance was used, with an opening angle of 0.53 steradian at the image center as proposed by [42]. For consistent glare estimation with these measures, the “valid” range of DGP is within 0.2 - 0.8, and  $E_v$  should be above 380 lux [170]. Therefore, the dataset was again screened for values within the “valid” DGP and  $E_v$  range for a fair comparison with respect to visual comfort sensation, and the resulting data points were reduced to 77. There was no filtering for solar disk within the FOV (that could result in overflown pixels) since the shades are lowered to 35% (Figure 5.18).



Figure 5.19 HDR images captured by Sensor I during a sunny day

Figure 5.20 presents selected examples of captured and re-projected luminance maps at three different times of a day (9AM/ 12PM / 3PM) during the experiments, and respective DGP values (data screening for DGP was not applied here to present the examples during a day). HDRscope [73] was used for visualization of false-color luminance maps. For a fair comparison, the logarithmic false color scale was set equally to 0 - 20,000 cd/m<sup>2</sup> for all the luminance maps. The actual absolute difference in per-pixel luminance is also shown in the last row for each case. Some qualitative observations are listed below:

- Overall, the luminance map re-projection shows a nice resemblance for the majority of mapping regions. Although there are some scenes with inaccurate reconstruction, such as the exterior scene visible through the window, still the major parts of the room (screen, walls, and ceiling) seem to be well aligned.
- The majority of the pixels, except for directly sunlit areas, showed small absolute luminance errors (below 100 cd/m<sup>2</sup>). Whenever there is a significant sunlit projection on interior surfaces (e.g., on the wall or desk at 9 am), the absolute luminance error becomes significantly higher.
- DGP values calculated from re-projected luminance maps match closely with the measured ones from the occupants' FOV.

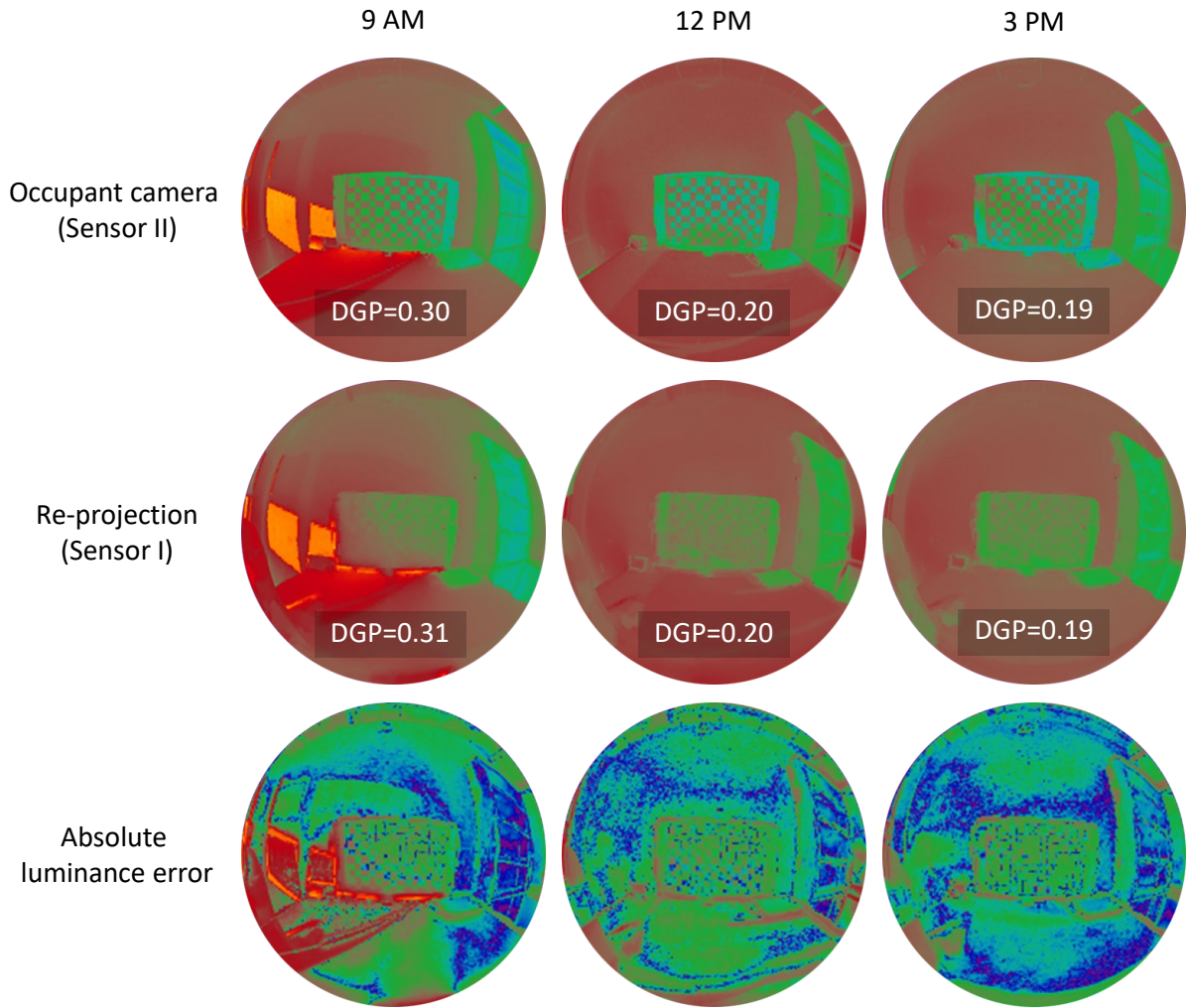


Figure 5.20 False-color luminance maps comparison: occupant camera-measured vs re-projected

To evaluate the predicting performance of daylight glare sensation through the proposed framework, the root mean squared error (RMSE) between Sensor I re-projection and Sensor II measurement was calculated for each of the three metrics (DGP,  $L_{avg}$  and  $E_v$ ). These are displayed together with scatterplots of measured vs re-projected DGP,  $L_{avg}$  and  $E_v$  in Figure 5.21. Despite the errors associated with pixels of excessive luminance, the RSME is small for all three visual comfort performance metrics. These results prove that the proposed framework can be used for non-intrusive monitoring of occupant visual comfort for the studied configurations and typical office luminance variations.

Table 5.7 Experimental data statistics

	DGP			$L_{avg}$ (cd/m <sup>2</sup> )			$E_v$ (lux)		
	min / max (std.)	RSME	R <sup>2</sup>	min / max (std.)	RSME	R <sup>2</sup>	min / max (std.)	RSME	R <sup>2</sup>
Sensor I (Re-projection)	0.20 / 0.37 (0.05)			6 / 995 (193)			28 / 3042 (548)		
Sensor II (Occupant position)	0.20 / 0.34 (0.04)	0.01	0.964	8 / 838 (179)	21	0.993	40 / 2669 (584)	51	0.996

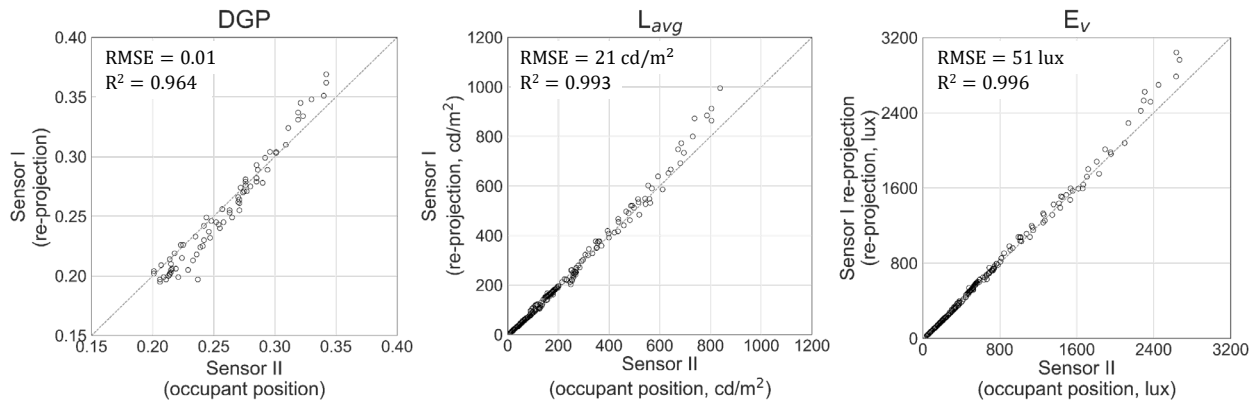


Figure 5.21 Scatter plot of DGP, Lavg and Ev with RSME for each metric (re-projected quantities vs. actual measurements from occupant position)

## 5.8 Discussion

The framework was evaluated in a typical small private office, under sunny conditions in late fall. The studied cases included a person seated close to the side wall, parallel to the window. The results ensure that the method is applicable to (i) cloudy conditions, or any condition with lower luminance/illuminance values, since in this case the variation would be much smaller, and the relative errors even smaller, (ii) higher solar angles, meaning all other seasons except for winter and (ii) in deeper rooms, where the luminance and illuminance values will naturally decrease with room depth. Therefore, we do not need to demonstrate the validity of the proposed method for the above cases.

However, in our experimental evaluation, the window did not constitute a significant part of the occupants' fixed FOV. As a result, the solar disc was not visible by the occupant, not were

extremely bright areas from the sky through the unshaded portion window (as commonly recommended). Given the fact that luminance errors were introduced when pixels with high luminance were present (i.e., sunlight in the occupants' FOV), it is worth investigating the validity of the method under high or extreme luminance conditions. Although such conditions should be normally avoided in occupied offices for glare protection reasons, they can occur sometimes and they are useful when evaluating the performance limits of the method, since it is expected that the prediction accuracy will be compromised under such conditions. Since the SfM-MVS 3D reconstruction pipeline reconstructs the window as a flat surface, it fails to correctly re-project the exterior scene through the window. Sensor I is tilted 20 degrees downward, so it is missing a significant portion of the sky patch visible through the window (compared to the occupant position), the discrepancy in re-projecting the window exterior scene correctly can be intensified. This is also related to the relative position between the two sensors.

For these reasons, an additional evaluation was performed in late fall (end of November) when the solar incidence angle remains low. The exact same procedure was followed but the window portion within the occupants' FOV was increased by moving the occupant closer to the window (2m away) and in the middle of the room. In this setup, the window region covers a significant portion of the occupant FOV in this layout - a solid angle around 0.50 steradian according to the fisheye image taken from the occupant position. Furthermore, to allow excessive luminance values in the FOV, the shades were moved to 50% (half-open) and 100% (fully open), creating different luminous conditions in the room captured from both sensors. A total of 289 points were collected. These were filtered to (i) remove instances that included the solar disc, since they will result in overflowed pixels and (ii) as before, check again for values within the "valid" DGP range. After these modifications, the dataset was reduced to 119 data points.

The RMSE for each of the three metrics was again calculated and displayed together with scatterplots of measured vs re-projected DGP,  $L_{avg}$  and  $E_v$  in Figure 5.22. Despite the errors associated with problematic re-projection of exterior views and excessive luminance values resulting in significant absolute luminance errors, the RSME is relatively small for all three visual comfort performance metrics. Nevertheless, the results show that there are several cases with inaccurate estimations. Therefore, improvements in future work are required for a correct reconstruction of the exterior scene and luminance map re-projection within the occupants' FOV,

for cases where occupants are seated close to unshaded windows under sunny skies. One idea for future work is to apply an indoor “mask” on the window surface in the HDR image using a photo-editing software, so that it is excluded from further analysis.

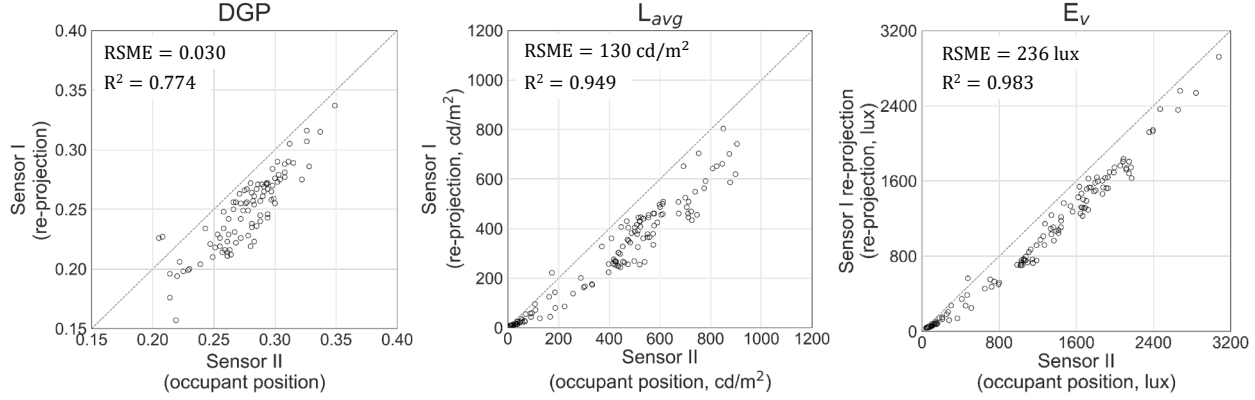


Figure 5.22 Scatter plot of DGP,  $L_{avg}$  and  $E_v$  with RSME for each metric with increased window views and open shades (re-projected quantities vs. actual measurements from occupant position)

## 5.9 Chapter conclusion

This study presents the development and implementation of a novel, semi-automated framework for non-intrusive monitoring of occupant-perceived luminance distribution, using an HDRI sensor. Despite the obvious potential of using HDRI sensors for daylighting controls in buildings, there has not been a practical and scalable method to measure occupant-perceived luminance maps either without intrusiveness/distraction or manual commissioning. A Structure-from-Motion and Multi-View-Stereo (SfM-MVS) photogrammetry framework was employed to automatically reconstruct the 3D geometry of the room and estimate the occupant head-poses. Retrieved 3D context enables the back-projection of the camera-captured luminance distribution into 3D spaces that are in turn re-projected to occupant FOVs with the estimated head poses. The proposed method does not require expensive devices or labor-intensive commissioning effort for modeling of 3D geometry that is essential for non-intrusive luminance re-projection. The user can utilize readily available camera devices without knowing camera geometric parameters a priori and is only required to take a short video and pictures at the occupant position. The rest of the framework including the camera calibration, 3D room reconstruction, and re-projection is fully automated. Since the method offers an end-to-end pipeline for occupant-perceived luminance map

creation, there is no need for post-processing or model fitting for its outputs to predict occupant visual comfort.

To demonstrate the method and evaluate the performance of the proposed framework, experiments were conducted in a side-lit private office under various luminous conditions. Using a sensor installed 2 meters high on the wall, occupant-perceived luminance maps were created. The evaluation was performed by calculating three visual comfort metrics from the HDR images: daylight glare probability, average luminance of the scene, and vertical illuminance at the eye. The RMSE results showed that the quantities computed from the re-projected luminance maps show good agreement with the occupant-measured values, except when reflection of direct sunlight presents nearby the occupant, where the scale of luminance error becomes noticeable –however, these instances should be avoided for glare protection. Also, since the SfM-VMS pipeline does not accurately reconstruct the exterior scene through the window, the re-projected luminance maps may yield erroneous visual comfort predictions if the occupant FOV is dominated by large bright window views.

The proposed method assumes predominantly diffuse interior surfaces – which is generally true in offices - that reduce the error in luminance perceived from different views of the room. However, if the specular reflectivity of the surfaces is high, then the performance of the framework is compromised. Also, the SfM-MVS pipeline used in this study is an established method but has limitations under certain circumstances, such as for surfaces with texture-less regions – such as single-color painted walls– because SfM reconstructs points with interest points with distinctive features. To address this issue with the proposed method, the user can manually add such features if the room is relatively small. Instead, as a future improvement, we can replace the SfM-MVS with a different method of 3D reconstruction, such as using RGBD cameras or LiDAR (Light Detection and Ranging). Those systems can reconstruct accurate and robust 3D models even without the texture-richness of the objects but the equipment required can be expensive. Also, an increasing number of end-user products such as smartphones and tablets, include Time-of-Flight (ToF) cameras - for depth estimation – or even built-in LiDAR that can serve as an indoor reconstruction tool.

Finally, this study presents a novel first step towards non-intrusive luminance monitoring of occupant-perceived scene based on HDRI sensors. Certainly, there are improvements required before wide-scale practical application in real buildings. One example is the ambiguity in sensor

installation. There are no guidelines for recommended sensor locations with respect to the occupant position for this type of applications, and future work should explore the performance of various relative positions and installation configurations to ensure a certain performance of the method.



## **6. PERFORMANCE EVALUATION OF NON-INTRUSIVE LUMINANCE MAPPING TOWARDS HUMAN-CENTRIC DAYLIGHTING CONTROL**

### **6.1 Experimental evaluation and data analysis**

To evaluate the luminance re-projection framework, the method was implemented in a full-scale private office room. Luminance maps collected by an HDRI sensor installed at a non-intrusive position were re-projected to two different occupant views for a comprehensive analysis and assessment. The performance of the re-projected luminance maps was evaluated via per-pixel and metric-based comparison to the actual measurements from HDRI sensors installed at the corresponding occupant positions.

#### **6.1.1 Experimental setup**

The experiment was performed in a south-facing office room, 3.2 m wide  $\times$  4.0 m long  $\times$  3.2 m high. The façade has a high-performance glazing unit (normal  $T_v = 64\%$ ) with a window-to-wall ratio of 54%. The room is equipped with interior dark-colored motorized roller shades (normal  $T_v=2.5\%$  and openness factor 2.2%) controllable either via building management system or manual override.

The instrumentation setup and room layout are shown in Figure 6.1 and Figure 6.2. The room has a typical side-lit layout where the occupant is seated parallel to the window. Although the testbed room is a private office suited for one-person use, two different occupant positions are tested to examine the proposed system's behavior and sensitivity relative to the distance from the window (bright source). The occupant position closer to the window (1.5m) is labeled as Position I and the other one (2.5m) is labeled as Position II. The varying distances from the window were intended to create different window portions within the occupant FOV as well as the overall perception of brightness during the experiment: Position I represented a position exposed to frequent bright conditions within the FOV (where glare is very likely without proper shading operation) and larger outside views. Position II shares a smaller window view within the FOV of the occupant but is also more protected from bright conditions and sunlight. To create a real office-

like setup, a typical workstation configuration (a table and a computer screen) was set for each occupant position.

Three calibrated fisheye HDRI sensors - namely Sensor I, II, and III - were installed at different positions: Sensor I and Sensor II (occupant sensors) were installed at occupant Positions I and II to capture the actual luminance distributions perceived from the virtual occupants. Both sensors were installed at seated occupant eye height (1.2 m from above the floor). Sensor III was vertically attached to the wall behind the occupant positions at 1.8 m height and served as the non-intrusive HDRI sensor for luminance monitoring. Each of the sensors was connected to a single Raspberry Pi B+ single-board computer for HDR image collection and real-time processing. Example images taken from the sensors are presented in Figure 6.3.

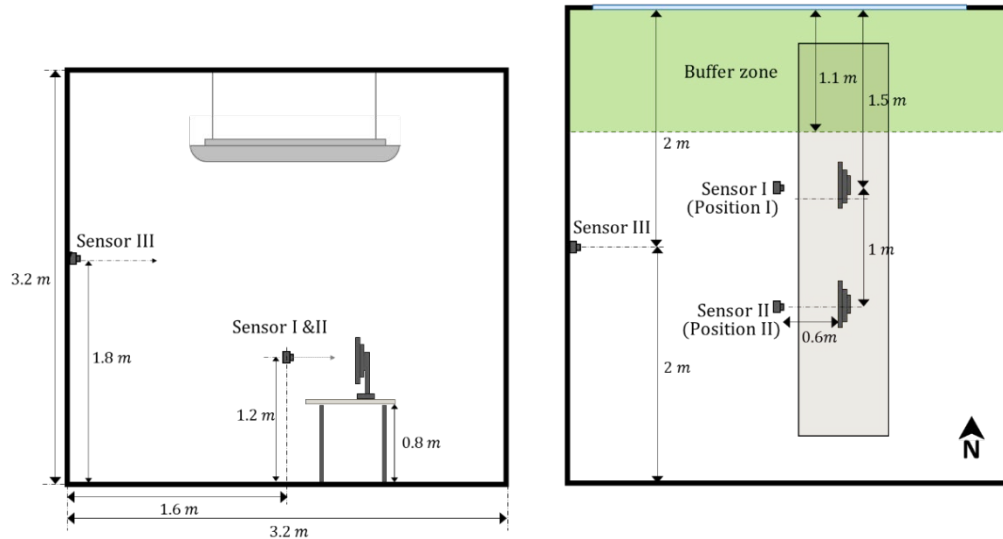


Figure 6.1 Instrumentation and space layout for experiment (left: side view; right: top view)



Figure 6.2 Interior view of testbed office

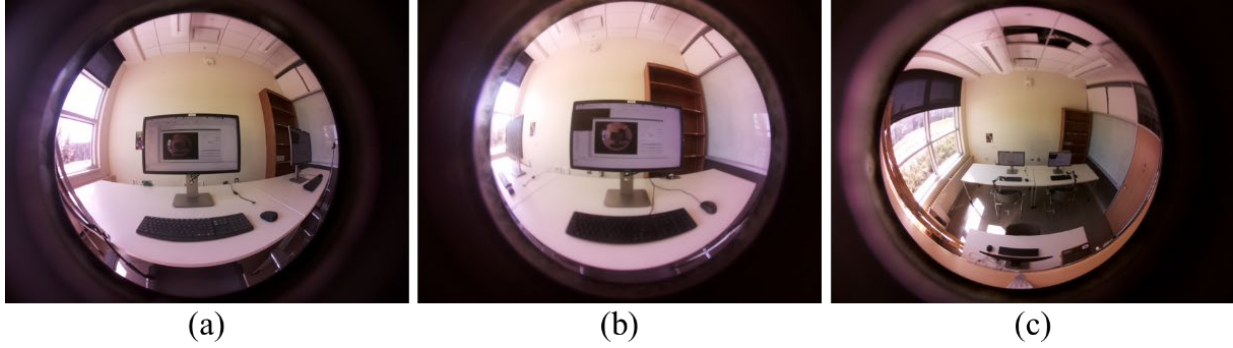


Figure 6.3 LDR images captured by HDRI sensors (a) Sensor I (b) Sensor II (c) Sensor III

### 6.1.2 Experimental procedure and data collection

Before the data collection, the 3D mesh model of the room and HDRI-sensor perceived depth maps required for the luminance map re-projection were retrieved via COLMAP-OpenMVS 3D reconstruction pipeline[146,160]. The luminance maps stored in Raspberry Pi B+ were post-processed on a separate desktop computer. The post-processing includes: i) the re-projection of luminance maps captured by the Sensor III into the occupant FOVs; ii) re-projection of luminance maps measured by occupant sensors into a standardized fisheye projection; iii) visual comfort metrics calculation from all output luminance maps for performance evaluation of the proposed system.

The re-projected luminance maps were collected and compared against the luminance maps taken from the occupant positions (Sensor I and Sensor II readings). Luminance map captured by all the HDRI sensors was synchronized via Python scripts with a 5-minute-interval. To test the performance of the proposed system in realistic conditions, roller shades were controlled based on a glare protection mode, including a sun-tracking algorithm and a buffer zone ( $>1.1\text{m}$  from the window) similar to a model-based control [100], to avoid sunlight on the work plane near the person, as in Figure 6.2 (any customized shading control is possible but that is outside the scope of this study). The algorithm requires calculation of the solar profile angle ( $\Omega$ ) and knowing the basic room geometry. The experiment was performed in sunny days with intermittent cloud coverages in Spring 2021, from 9 AM to 6 PM each day.

The luminance maps collected from non-intrusive Sensor III were re-projected into an equidistant fisheye projection with FOV of 170 degrees. The reason for not choosing the 180-degree-FOV is because the current version of Open3D-Python, used for the re-projection, does not

support capturing such extremely distorted still images from the reconstructed 3D models: the occupant-perceived scene is re-projected into a pinhole with a small focal length, which is in turn re-mapped into an equidistant fisheye image via OpenCV-Python *remap* function. For this method, the one-to-one pixel correspondence between the original camera projection and the target projection needs to be calculated based on the camera geometric parameters estimated through the calibration procedure. Luminance maps captured from occupant positions are also converted to the same equidistant projection as the re-projected maps. As shown in Figure 6.4b, the resulting luminance maps are equidistant images centered at square (1:1 aspect ratio) resolution where the principal (distortion) center matches the image center. The reason for synchronizing the projection between the non-intrusive HDRI sensor and the occupant sensors is two-fold: i) to align the pair of images (the re-projected luminance map and the occupant sensor measurement) as much as possible for pixel-to-pixel comparison; ii) to create luminance maps that have Evalglare-compatible fisheye projection (equidistant projection) for further analysis using this tool [65].

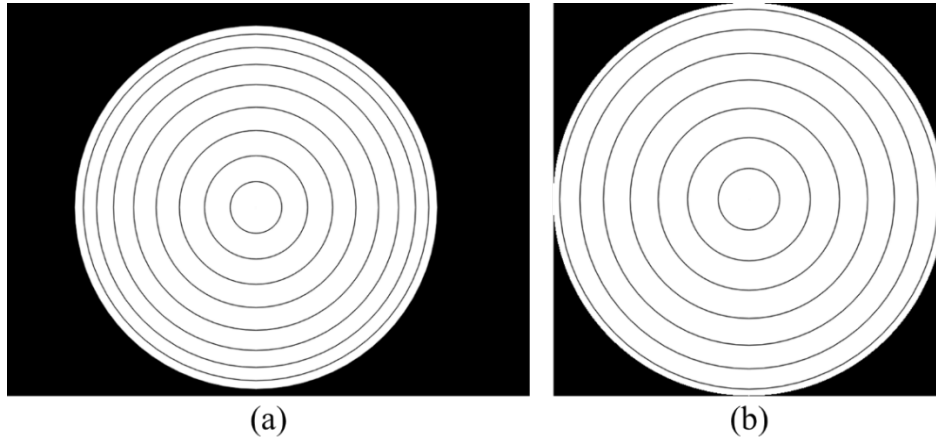


Figure 6.4 Fisheye transformation example. Concentric circles represent incident angles with 10-degree increment (a) Original Sensor I projection (180-degree FOV); (b) Output equidistant fisheye projection (170-degree FOV)

## 6.2 Performance evaluation

The performance of the luminance re-projection pipeline was investigated four-fold as summarized below.

- The per-pixel similarity between the actual measurement from occupant sensors and the re-projected luminance maps was quantified via a similarity metric named Structural Similarity Index Measure (SSIM).
- Comparison of visual comfort metrics - DGP and vertical illuminance ( $E_v$ ) - was performed to evaluate practical implications for visual comfort prediction through the proposed system.
- Region-by-region analyses of SSIM and visual comfort metrics: The re-projected luminance maps and the occupant sensor measurements were compared regionally to detect errors between regions of interest, as well as to identify the major source of errors.
- A case example of DGP threshold was determined to evaluate occupant glare prediction from re-projected luminance maps, based on Receiver Operating Characteristic (ROC) curves.

### 6.2.1 Structural Similarity Index Measure (SSIM)

Structural Similarity Index (SSIM) was used as a measure to evaluate the similarity between the re-projected luminance maps and the measured from the actual occupant positions. SSIM is a perceptual measure that quantifies the degradation of image quality between a pair of images -a reference image and a test image [171]. The metric is formulated as an average of products of comparison metrics for three key features, locally extracted from a pair of images. The key features include luminance, contrast, and structure. The major advantage of using the metric over simpler similarity measures that consider pixel-to-pixel error quantification is that it allows comparing images in superpixel-scale (a perceptual group of pixels that share common characteristics). Thus, we can quantify the similarity between luminance maps where the coordinates of corresponding pixels do not exactly match (due to the re-projection process). The equational form of local SSIM computed from a local window (region) of reference image  $\mathbf{X}$  and test image  $\mathbf{Y}$  is:

$$\text{SSIM}(\mathbf{x}, \mathbf{y}) = \frac{(2\mu_x\mu_y + C_1)(2\sigma_{xy} + C_2)}{(\mu_x^2 + \mu_y^2 + C_1)(\sigma_x^2 + \sigma_y^2 + C_2)} \quad (6.1)$$

where  $\mu_x$  and  $\mu_y$  are mean pixel intensity of  $\mathbf{X}$  and  $\mathbf{Y}$ ,  $\sigma_x$  and  $\sigma_y$  are the standard deviation of  $\mathbf{X}$  and  $\mathbf{Y}$ ,  $\sigma_{xy}$  is the correlation between  $\mathbf{X}$  and  $\mathbf{Y}$ , and  $C_{1-2B}$  represents stability constants that are usually determined by the dynamic range of the data. Finally, the global SSIM value can be calculated by taking the mean of entire local SSIM values across the image.

$$\text{MSSIM}(\mathbf{x}, \mathbf{y}) = \frac{1}{M} \sum_{j=1}^M \text{SSIM}(x_j, y_j) \quad (6.2)$$

where  $x_j$  and  $y_j$  are image patches covered by the  $j$ -th local window and the number of local windows over the images is represented by  $M$ . The metric value is adjusted to be ranged between  $[0, 1]$ , where a value of 1 indicates that the two images are identical while 0 indicates they are completely dissimilar. Since fisheye images processed for this analysis contained zero-filled pixels outside of the fisheye circle outside the maximum FOV, those pixels are excluded when pixel-averaging for global SSIM calculation.

### 6.2.2 Visual comfort metrics comparison – DGP and $E_v$

To assess the proposed re-projection pipeline with respect to the practical implication (can we effectively predict occupant visual comfort from the re-projected luminance maps?), two visual comfort metrics, DGP and  $E_v$  were compared. They were validated as the best glare predictors in terms of performance and robustness in a recent cross-validation study [71]. The commonly used DGP threshold for noticeable glare is 0.35, while the threshold for  $E_v$  derived from simplified DGP (DGPs) is 2,670 lux. Note that DGPs was derived from a correlation to the original DGP metric and assumes there is no direct sun or specular reflection within occupant FOV [67]. Both metrics are calculated using Evalglare [65], open command-line software for glare analysis on fisheye HDR images.

### 6.2.3 Region-by-region analysis

To quantify errors segmented by regions of interest, four different masks were applied to the luminance maps. The purpose of this analysis was to understand the magnitude of regional error in the re-projected image that can potentially occur in a real office environment and to identify the major contributor to the error. The four regions of interest (Figure 6.5) include *Interior* regions excluding the window, *Window* region, *Task area* (defined as the pixels that refer to the 30-degree-FOV zone center-aligned at an image), and the *Computer screen*. For each region, a numeric array filled with 0 (for the non-interest region) and 1 (for interest region) was manually created via photo-editing software. Each of the luminance maps was then multiplied with the masks, thus each resulting luminance map includes each region of interest, while the rest of the pixels were filled with zeros. SSIM and visual comfort metrics were then computed again from

the fabricated (mask-applied) luminance maps. For each region, MSSIM was computed from only the corresponding pixels within the mask. For visual comfort metrics (DGP and  $E_v$ ), applying the mask for small regions (*window*, *task area*, and *screen*) is not suitable since metrics computed from such a limited portion do not convey meaningful information. Alternatively, the metrics were computed applying only the *interior* mask, so we could isolate the effect of window –the major candidate for introducing errors in re-projected luminance maps. Examples of interior-masked luminance maps are shown in Figure 6.6.

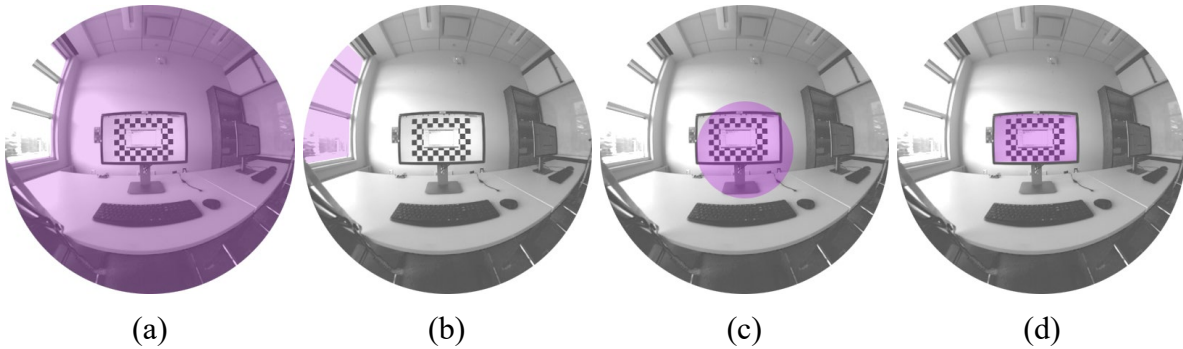


Figure 6.5 Masks by region. (a) Interior; (b) Window; (c) Task; and (d) Computer screen as seen from occupant Sensor I

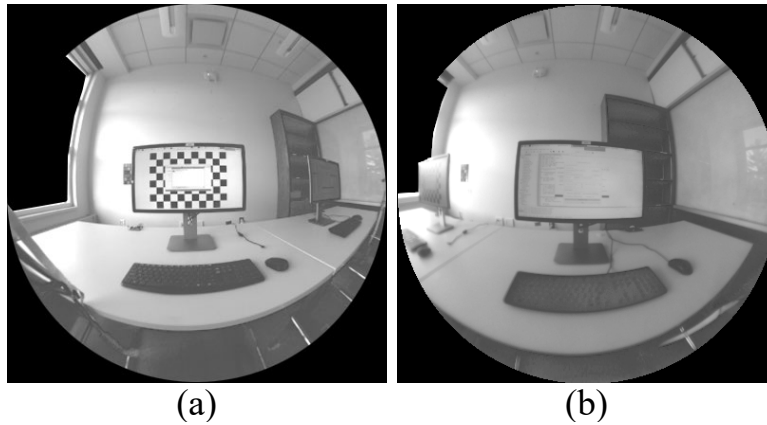


Figure 6.6 Masked luminance map with interior region-only as seen from occupant sensors (a) Sensor I (b) Sensor II

#### 6.2.4 Receiver Operating Characteristic (ROC) Curve

To assess the predictive power of the proposed non-intrusive luminance monitoring framework, a diagnostic analysis based on Receiver Operating Characteristic (ROC) curve was

used. ROC curve is a graphical plot that evaluates the diagnostic accuracy of a binary classifier system. In human-centric daylighting research, Rodriguez et al. [172] and Wienold et al. [169] utilized the ROC curve-based analyses as an assessment tool to examine the discriminative power of glare metrics developed from human experiments. The major outcomes provided by ROC are two: the diagnostic accuracy of the test and the optimal cut-off value for the test.

ROC curve is a probability curve that plots the true positive rate (TPR) of a binary classifier against its false-positive rate (FPR) at various cut-off (threshold) values. TPR in visual comfort metrics can be interpreted as a probability of being classified as positive from a visually disturbed person, while FPR corresponds to a probability of having a positive result from a person without a comfort issue. An ideal binary classifier is a classifier that has 100% TPR and 0% FPR that completely distinguishes between positive and negative instances. The 45-degree diagonal line from (0, 0) to (1, 1) serves as a reference line that refers to a completely useless classifier that cannot distinguish between the true positives and negatives. Thereby, the higher the ROC curve drawn above the reference line, the better the diagnostic accuracy of the classifier. It is practically impossible to have a perfect classifier due to the probabilistic nature of human visual perception. Nevertheless, ROC can still serve as an effective tool to assess the general performance of a classifier and to choose an optimal threshold value based on TPR/FPR trade-offs.

Some useful diagnostic indicators can be extracted from a ROC analysis. Area Under Curve (AUC) is one of the commonly used summary measures for overall diagnostic accuracy of the classification that is invariant to the cut-off value. AUC can be retrieved by integrating the area beneath the ROC curve with respect to the FPR and practically lies between 0.5 and 1.0. A model whose predictions are completely uninformative has an AUC of 0.5 (a random classifier); one whose predictions are 100% accurate has an AUC of 1.0 (an ideal classifier). The rule-of-thumb interpretation of model accuracy based on AUC value is presented in Table 6.1 [173].

Table 6.1 Interpretation of AUC value

AUC = 0.5	$0.7 \leq \text{AUC} < 0.8$	$0.8 \leq \text{AUC} < 0.9$	$0.9 \leq \text{AUC}$	AUC = 1.0
Uninformative	Acceptable	Excellent	Outstanding	Ideal



In this study, we used DGP and  $E_v$  for ROC analysis for the similar reason described in Section 6.2.2. Although DGP has a probabilistic nature - its value being correlated with the percentage of dissatisfied people -, it provides thresholds that are widely accepted for practical use. We chose 0.35 (noticeable glare) as a visual comfort threshold for DGP: a DGP above the value was considered to pose a glare risk. For  $E_v$ , a cut-off value of 2,670 lux was inversely calculated from DGPs value of 0.35. Deriving the  $E_v$  from DGPs was valid since the automated roller shades control prevented the sunlight from reaching the occupant FOV, guaranteeing the high correlation between DGPs and DGP [37]. In a practical perspective, a daylighting system should maintain a DGP or  $E_v$  (perceived from the occupants) below a certain threshold. Thus, the instances where the DGP measured from the occupant position ( $DGP_{occ}$ ) greater than 0.35 were labeled positive and vice-versa for the negative instances (similarly for  $E_v$ ). DGP and  $E_v$  calculated from the re-projected luminance maps ( $DGP_{rp}$ ) were treated as the binary classifier subject to the ROC analysis. To summarize, the purpose of ROC analysis was to evaluate the performance of visual comfort prediction based on the non-intrusive luminance monitoring framework (sub-optimal classifier) compared to the system based on HDRI sensor placed at the actual occupant position (assumed as an optimal classifier). In this context, TPR and FPR for the ROC curve were defined as presented in Table 6.2.

Table 6.2 DGP classification for ROC analysis

	$DGP_{rp} (E_v) \geq \text{Threshold}$	$DGP_{rp} < \text{Threshold}$
$DGP_{occ} \geq 0.35$ ( $E_v \geq 2,670 \text{ lux}$ )	True positive (TP)	False negative (FN)
$DGP_{occ} < 0.35$ ( $E_v < 2,670 \text{ lux}$ )	False positive (FP)	True negative (TN)

There remains a practical need to select a specific cut-off value when one attempts to apply the non-intrusive luminance monitoring framework to a human-centric daylighting control. Several methods exist to determine the cut-off threshold, and in this study we used the three most common ones. The first popular method is using the Youden index ( $J$ ) method. This method defines the optimal cut-off value as the point that maximizes the sum of TPR and TNR over all possible cut-off values. Another method is choosing a cut-off value that minimizes the squared distance (sqD) between the corresponding point (FPR, TPR) and the top left corner (a perfect

classifier) of the ROC plot. Aside from the commonly used methods that pose equal weights to TPR and FPR, it is possible to opt a customized cost function (labeled *custom*) subject to minimization as follows:

$$Cost = C_{TP}TPR + C_{FP}FPR$$

where  $C_{FP}$  and  $C_{FN}$  corresponds to the cost associated with the TPR and FPR. This method is particularly useful when it is desired to assign different weights for the classification scores. In this study,  $C_{TP}$  of -2 and  $C_{FP}$  of 1 was tried to examine the threshold, since false detection of glare was deemed less significant than failing to identify discomfort in glary situations. Table 6.3 summarizes the metrics examined for optimization of the cut-off value for non-intrusive visual comfort prediction.

Table 6.3 Optimization metrics for cut-off determination

Youden Index ( $J$ )	sqD	<i>Custom</i>
Maximize the sum of TPR and TNR (=Maximizes TPR subtracted FPR)	Minimize the Euclidean distance from (TPR:1, FPR:0)	Minimize the customized cost function = $-2 * TPR + FPR$

### 6.3 Results

A total of 756 points was collected throughout the experiment. Figure 6.7 presents representative examples of captured and re-projected luminance maps at the occupant position during five different times (9 AM – 5 PM with two-hour-interval) of a day. The images on the first row are the false-color luminance maps taken from occupant Sensor I and corresponding re-projections are shown in the second row. For false-color visualization of luminance maps, HDRscope [73] was used. The logarithmic color-scale was synchronized to  $[0 \text{ cd/m}^2, 20,000 \text{ cd/m}^2]$  for all the luminance maps for a fair comparison in visualization. Some qualitative observations preliminary to the further analysis are as follows:

- At a glance, re-projection and the actual measurement luminance patterns show a nice resemblance for most of the image. Despite some misalignment due to the re-projection process, the position and the relative proportion of major elements perceived by human vision (i.e., building elements and computer screen) look very similar.

- The exterior scene visible through the window is poorly re-constructed compared to the interior objects, consistent with the observation from Chapter 5.

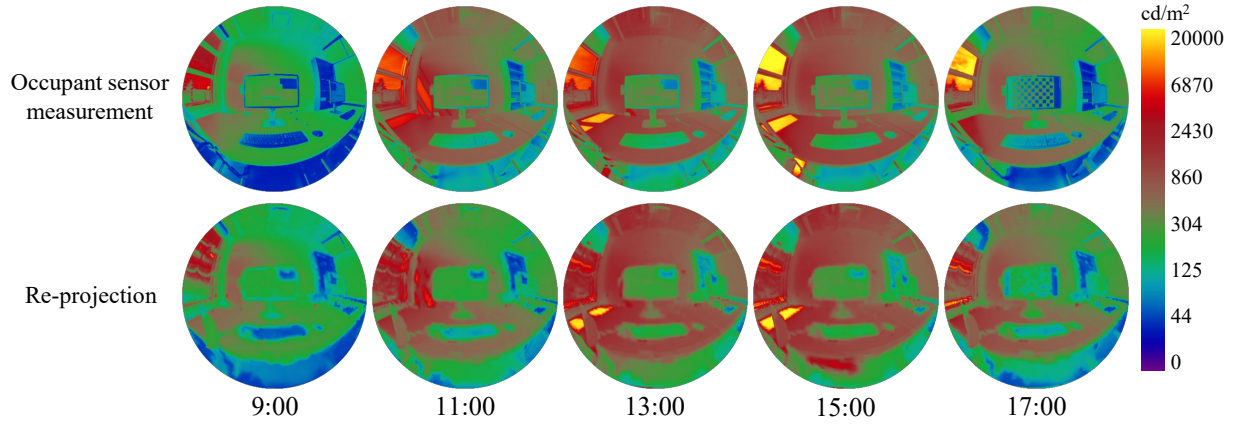


Figure 6.7 Representative false-color luminance maps comparison: occupant camera-measured vs re-projected maps

### 6.3.1 Data statistics, overall and regional similarity measure of re-projected luminance

The distribution of visual comfort metrics extracted from all luminance maps is presented in Figure 6.8. The actual DGP measured from the occupant positions ranged between 0.19 – 0.41 for Position I and 0.18 – 0.26 for Position II. For  $E_v$ , the respective ranges were 497 – 3365 lux and 279 – 1538 lux. The boxplots present median as middle line in each box and have whiskers with maximum 1.6 IQR (interquartile range). As expected, values are higher for Position I due to closer proximity to the window. For all positions and metrics, the re-projection showed slightly lower distribution compared to the occupant sensor readings. The percentage of points exceeding  $DGP=0.35$  (the pre-defined discomfort threshold) was around 10 % (75 out of 756 points) for Position I, while the entire measurement set from Position II was below the threshold. The DGP and  $E_v$  basic statistics from measured and re-projected images are presented in Table 6.4.

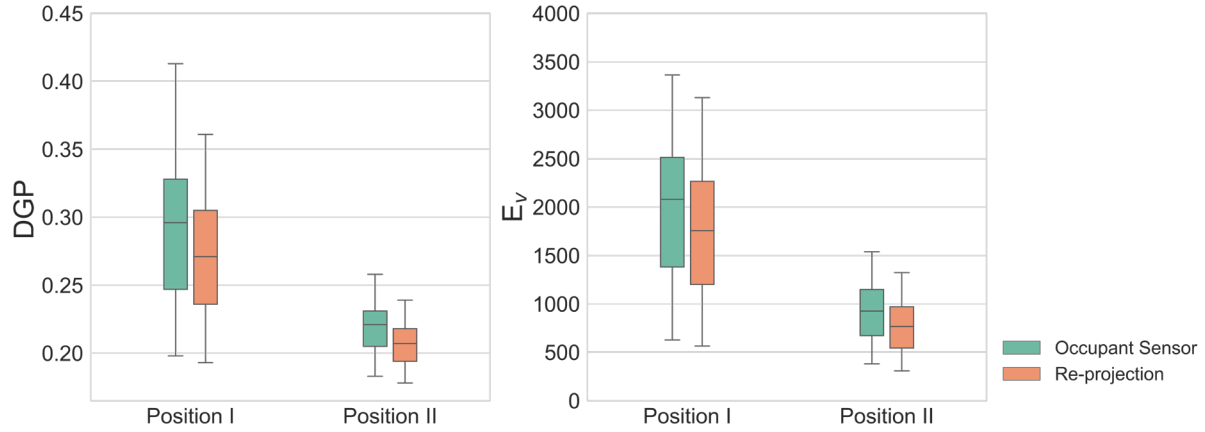


Figure 6.8 Visual comfort metrics distribution from luminance maps

Table 6.4 Data statistics

Position	Measurement	DGP			$E_v$ (lux)		
		Range	Mean	Std	Range	Mean	Std
Position I	Occupant	0.19 – 0.41	0.29	0.05	497 – 3365	1913	689
	Re-projection	0.18 – 0.36	0.27	0.04	404 – 3130	1691	641
Position II	Occupant	0.18 – 0.26	0.22	0.02	279 – 1538	893	289
	Re-projection	0.17 – 0.24	0.21	0.01	227 - 1323	739	247

For each pair of (occupant sensor-measured and re-projected) luminance maps, the overall MSSIM was calculated first. The average of MSSIMs computed from Position I and Position II are 0.82 (std=0.08) and 0.85 (std=0.05) respectively (Figure 6.9), which shows that the re-projected luminance map can mimic the actual occupant-received luminance despite small issues with accurate alignment of pixels etc.

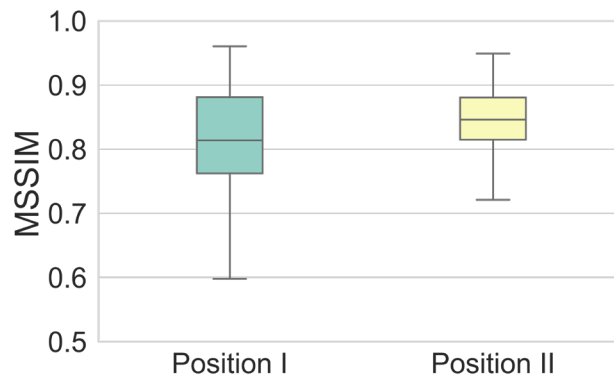


Figure 6.9 MSSIM distribution

For a region-scale analysis of SSIM, the masks shown in Figure 6.5 were applied to the full SSIM map (Markers outside of the whiskers are outliers). Then, the mean value (MSSIM) for each region was computed by averaging the masked SSIM map. As summarized in Table 6.5 and Figure 6.10, the mean MSSIM exceeded 0.8 in all regions for both positions, except for the window region, where MSSIM values are around 0.5. There is no widely agreed criterion on the acceptable range of MSSIM for re-projected luminance maps. However, through this regional comparison of MSSIM, it is clear that the method works well for all regions except for the window, which is identified as the main source of error between the actual and re-projected luminance distributions.

Table 6.5 MSSIM statistics by region

Region	<i>Full</i>		<i>Interior</i>		<i>Window</i>		<i>Task</i>		<i>Screen</i>	
Position	I	II	I	II	I	II	I	II	I	II
Mean	0.82	0.85	0.84	0.85	0.52	0.51	0.84	0.90	0.82	0.89
Std.	0.08	0.05	0.07	0.05	0.19	0.03	0.10	0.03	0.12	0.03

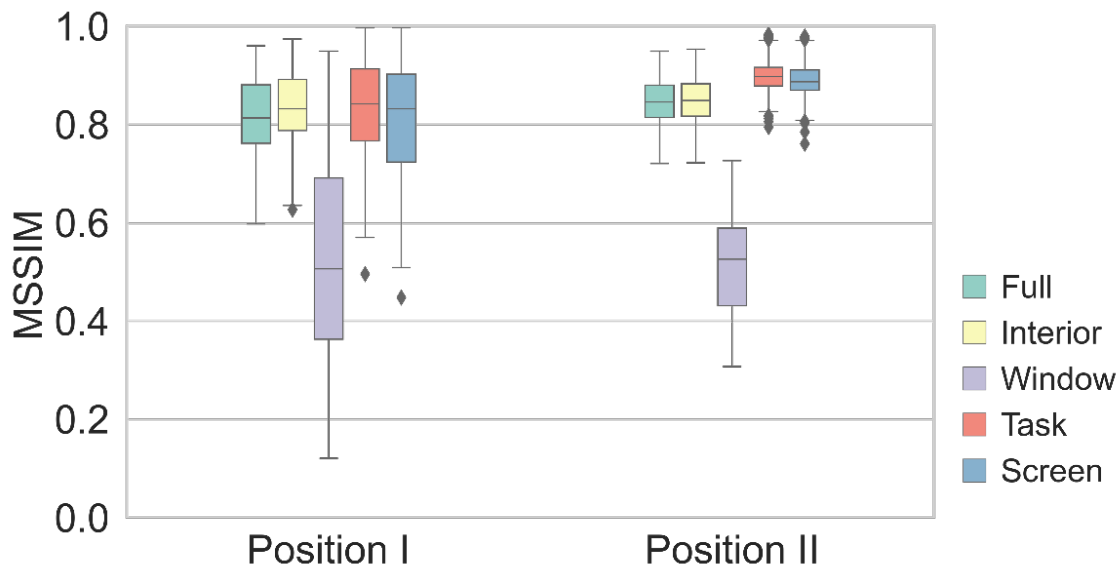


Figure 6.10 MSSIM distribution by region

### 6.3.2 Visual comfort metrics using re-projected luminance maps

The error in visual comfort metrics between the actual measurements and re-projected luminance maps at the occupant positions was examined in more detail. Figure 6.11 shows the scatter plots of measured vs re-projected DGP and  $E_v$ . Consistent with the boxplots in Figure 6.8, there is a wider spread and higher relative errors for Position I which is closest to the window, as expected. The RMSE for both metrics and positions is shown in Table 6.6. Figure 6.12 presents the relative error histograms of the visual comfort metrics. The maximum bound of DGP relative error is around 20% for Position I and 12% for Position II, while its  $E_v$  counterpart is much greater (50% and 25%). DGP is less sensitive to luminance pattern differences compared to  $E_v$  since the extreme luminance of glare source pixel can be smoothed by averaging and  $E_v$  is more directly correlated with luminance intensity of each pixel, compared to the logarithm applied to the square of average source luminance in DGP.

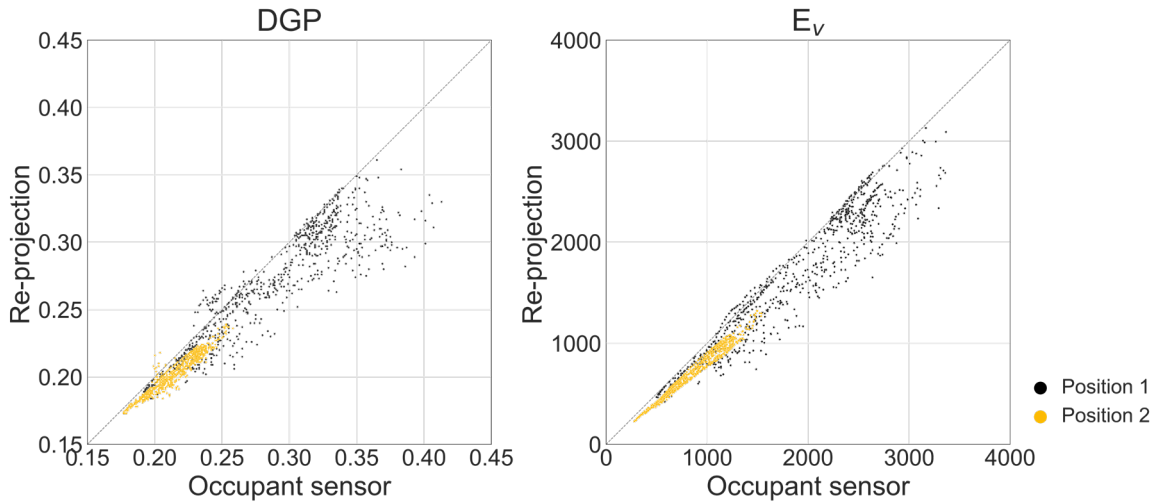


Figure 6.11 Scatter plot comparison of visual comfort metrics (re-projected vs measured luminance maps)

Table 6.6 Error statistics of visual comfort metrics using re-projected luminance maps

Position	DGP		$E_v$	
	RMSE	$R^2$	RMSE	$R^2$
Position I	0.029	0.83	310 lux	0.90
Position II	0.013	0.92	165 lux	0.97

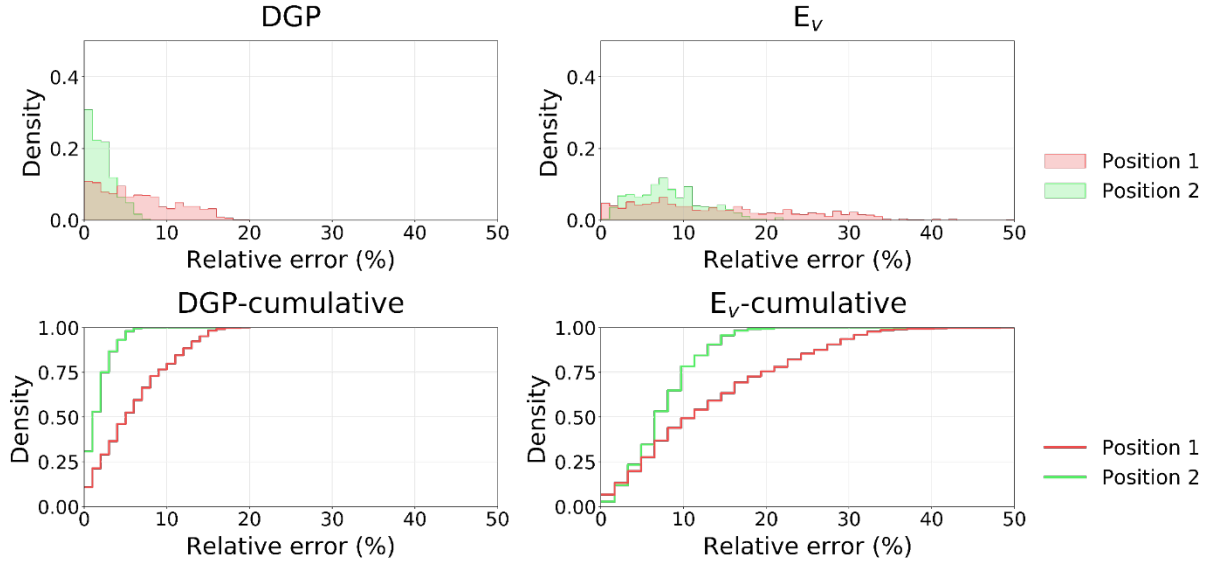


Figure 6.12 Relative error histograms of visual comfort metrics

Since the exterior scene through the window was identified as the main source of error between measured and re-projected luminance maps, DGP and  $E_v$  were computed again from the *interior* region that excludes the *window* region (Figure 6.5a), to examine how this masking scene can reduce that error. The scatter plots of DGP and  $E_v$  from the *interior*-masked luminance maps are presented in Figure 6.13 (subscript ‘int’ refers to the *interior* region). Errors in both metrics were significantly reduced for all ranges. The DGP RMSE was reduced from 0.029 to 0.006 and the  $E_v$  RMSE was reduced from 310 lx to 120 lx for Position I. Although the impact of the window exclusion is less significant for Position II, the error was reduced for that occupant position as well. These results indicate that the non-intrusive luminance re-projection method presents no noticeable errors in visual comfort metrics for occupant viewpoints with smaller window views.

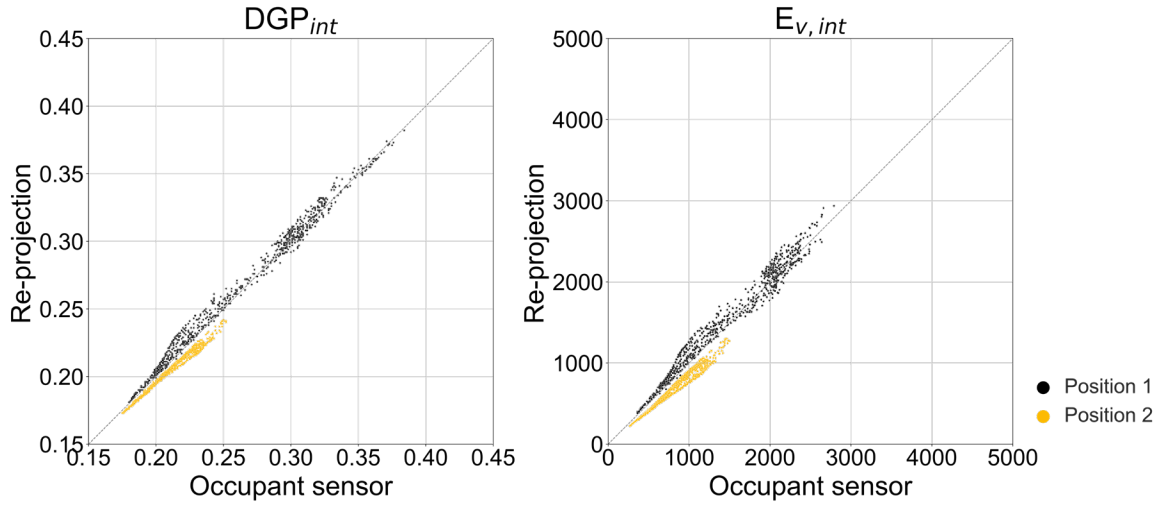


Figure 6.13 Scatter plot comparison of visual comfort metrics from interior-only luminance maps

Table 6.7 Error statics of visual comfort metrics from interior-masked luminance maps

Position	DGP <sub>int</sub>		E <sub>v, int</sub>	
	RMSE	R <sup>2</sup>	RMSE	R <sup>2</sup>
Position I	0.006	0.99	120 lux	0.97
Position II	0.007	0.98	155 lux	0.97

The ROC curves from the visual comfort metrics-based binary classifiers are presented in Figure 6.14. The AUC values from both metrics are above 0.80, meaning that the overall discriminative performance of the binary classification based on re-projected DGP and E<sub>v</sub> is ‘excellent’ according to the criterion presented in Table 6.8. The (FPR, TPR) coordinates corresponding to optimized cut-off values are displayed in the plot. The DGP threshold values for the re-projected occupant maps are 0.280, 0.290, and 0.275 based on Youden Index, sqD, and the customized cost function respectively. The TPR and FPR corresponding to the cut-off values are presented in Table 6.8, and can be useful for practitioners when choosing an optimal cut-off value.



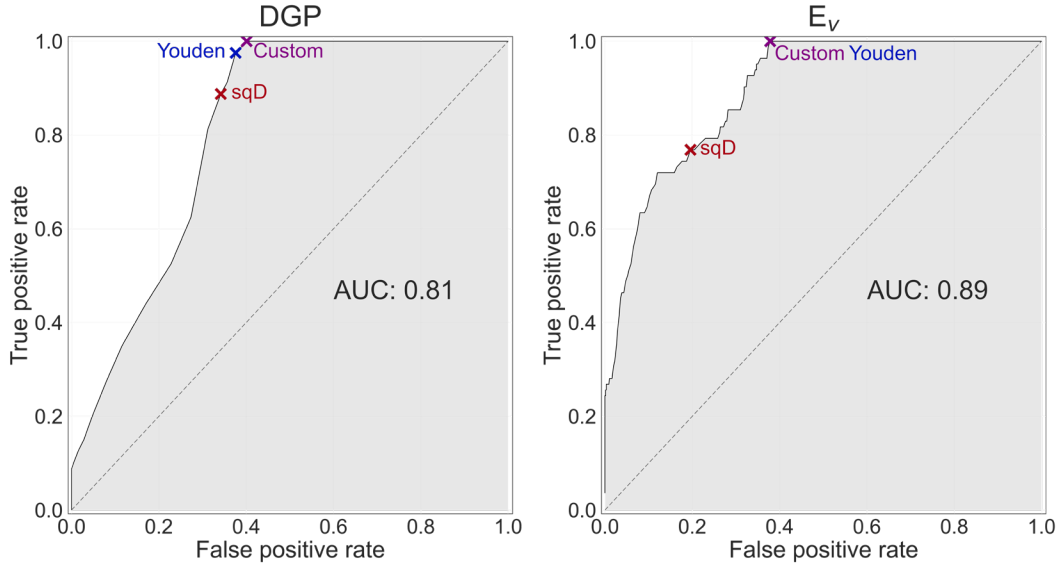


Figure 6.14 ROC curves from re-projected visual comfort metrics

Table 6.8 Optimized cut-off values from ROC analysis

	DGP			E <sub>v</sub>		
	sqD	Youden	<i>Custom</i>	sqD	Youden	<i>Custom</i>
Threshold	0.290	0.280	0.275	2250 lux	1860 lux	1860 lux
TPR	0.89	0.98	1.00	0.77	1.00	1.00
FPR	0.37	0.38	0.40	0.20	0.38	0.38

## 6.4 Discussion

In this study, the luminance map re-projection pipeline based on a non-intrusive HDRI sensor was implemented in a real office room. Two occupant positions, closer and further from the window, were examined, and larger window views within the occupant FOV resulted in larger errors in re-projected values. In our experiment, the interior roller shade was controlled to the highest possible position that prevents direct sunlight around Position I, and the parallel sun-tracking control allowed a realistic and practical operation that allows outside views. Nevertheless, there could be instances with a risk of glare even under this shading operation. According to the experimental results, around 10% of the points (75 out of 756) collected from HDRI sensor at Position I exceeded DGP of 0.35 (no such cases for Position II). The purpose of this work however

was not to develop perfect glare-based controls, but to test the non-intrusive luminance re-projection framework under reasonable, daylight control scenarios.

The RMSE of DGP for Positions I and II were each 0.029 and 0.013 respectively, both smaller than 0.05 which corresponds to the interval between different categorizations of glare perception. Yet, as observed from Figure 6.11, for larger DGP values, the absolute error of DGP can exceed 0.05, shifting values to the next glare category. Therefore, we should avoid using the original glare perception classification when using DGP from the re-projected luminance maps. However, it can be also claimed that the metrics error in comfort caused by the re-projection has a reasonable and acceptable range, even when tested at a challenging position close to the window.

As a similarity measure to examine the overall quality of re-projected luminance maps against the actual luminance maps captured from the occupant positions, the Structural Similarity Index (SSIM) was used. There is no agreed threshold criterion for SSIM to evaluate the quality of re-projected luminance maps. Further research is required on similarity metrics for luminance maps, to deliver semantical information and to globally use for luminance maps captured under different conditions. Nevertheless, the mean MSSIM computed from both positions showed good agreement with values above 0.80.

To evaluate the magnitude of re-projection error segmented by interest regions, a superpixel-scale analysis was performed by applying masks of four different regions of interest – interior, window, task area, and computer screen. Consistent with the findings from the qualitative observation (comparison of luminance maps in Figure 6.7), the window region showed a significantly lower MSSIM distribution compared to the others. Due to the poor reconstruction, the pixels corresponding to the exterior scene through the window had the greatest intensity and structural error, making itself the major contributor of DGP and  $E_v$  error computed from the entire luminance map. To examine the impact of re-projected window regions on errors in comfort metrics, DGP and  $E_v$  were re-calculated from the luminance maps where the *window* regions' pixels are excluded (set to 0  $\text{cd/m}^2$ ). Although the comparison is performed with fabricated luminance maps, it still provides a useful insight into the proposed system's performance on re-projection of interior regions. The exclusion of the *window* region significantly lowered the RMSE of DGP and  $E_v$  computed from the luminance maps. The resulting RMSE of DGP is below 0.01 for both occupant positions. Additional experiments are needed under different room

configurations, sun paths, shading systems and luminous conditions, including glare occurrences, for a more complete evaluation and generalization of the method.

To examine the performance of the visual comfort prediction using the re-projection framework, a ROC curve-based analysis was presented. The AUC value from DGP and  $E_v$ -based classifiers from re-projected luminance maps were 0.81 and 0.89, showing excellent overall diagnostic performance across all possible thresholds. A case method to determine the cut-off value for visual comfort prediction was presented. Two common methods based on squared distance and Youden index, along with a method using customized cost function was used to find optimal cut-off values. The ROC curve provides useful insight when choosing an optimal cut-off value since it allows to examine the TPR and FPR with varying cut-off values that are largely dependent on the classifier characteristics. There is a limitation in that the ROC analysis was not based on true on-site occupant responses thus it does not evaluate the actual performance of the proposed system to predict occupant visual comfort. Rather, the analysis compares the non-intrusive luminance monitoring system against the one that works with an HDRI sensor placed at the occupant position assuming it as a complete classifier (the ideal but impractical case). Experiments involving human subjects are always preferred when assessing the real-world performance of visual comfort delivery systems.

## **6.5 Chapter Conclusion**

This study presents the performance evaluation of a non-intrusive luminance monitoring framework. The method combines HDRI luminance monitoring from a non-intrusive position with 3-D reconstruction of the space to allow re-projection of luminance distribution, as perceived from the occupants, without labor-intensive commissioning or distractive sensor installation. A systematically-designed experiment was performed to collect a wide spectrum of interior luminous conditions in a real office environment. The experiment was conducted in a side-lit office with an interior roller shade automatically controlled via a sun-tracking-based algorithm and work plane sunlight protection. To examine the quality of re-projection relative to the size of the window, two different occupant positions were tested, close and further from the window.

The Structural Similarity Index (SSIM) was used to evaluate the overall agreement between re-projected and actual luminance maps captured from the occupant positions. The mean MSSIM

computed from both positions was above 0.8. Reasonable RMSE values were observed from the comparison of DGP and  $E_v$ . As suspected from previous work and from the qualitative comparison between selected actual and re-projected luminance maps, the major source of error was confirmed to be the pixels of the exterior scene visible through the window. A region-scale analysis was performed by applying masks in different regions of interest, to further assess the influence of various elements on errors. With the removal of the window region from the luminance maps, the RMSE of DGP and  $E_v$  were both significantly reduced to negligible values. The result partially confirms the hypothesis that the proposed framework can accurately re-project luminance maps exposed to any interior surface, even not fully diffuse. The diagnostic performance of the re-projection-based visual comfort predictor, relative to a predictor based on the occupant sensor measurement, was also evaluated. The AUC values above 0.8 from the classifiers revealed that the visual comfort prediction from the re-projected luminance map reasonably approximates the prediction from the actual HDRI sensor measurement from the occupant position - that even includes the large portion of the window within the FOV.

The proposed framework requires further improvement. Although the in-situ implementation in the testbed office exhibited a partial success, a more robust re-construction of the window region is needed for completion. To address the issue, the SfM-MVS pipeline used for 3D reconstruction can be replaced or reinforced with different methods, such as using RGBD cameras or LiDAR (Light Detection and Ranging) that yield robust and accurate 3D models. Generally, it is more expensive to operate such systems than the proposed framework, which only requires a readily available camera device. However, there is an increasing trend towards end-user products equipped with a built-in Time-of-Flight (ToF) camera or even LiDAR sensor that can boost the accuracy and robustness of depth estimation and indoor reconstruction. Considering that the commercialization of such products has emerged just recently, the future cost of their application is expected to reduce.

Overall, this study presents the systematic evaluation of the performance of the non-intrusive luminance monitoring framework. Although the framework needs further improvement for the wide-scale application across buildings, the results demonstrate the feasibility of the framework. When limited to the building interior, the re-projection yielded comfort metric values very similar to the actual measurements from the occupant positions. The future study recommendation includes the establishment of a systematic method to determine optimal sensor

placement concerning the office layout, maximizing the performance of the luminance monitoring system. Also, a long-term, large-scale field experiment involving multi-occupants in various office environments would provide useful insights on the practical implications of the framework towards generalization.

## 7. FUTURE WORKS

This chapter presents recommendations for extensions of this work.

### 7.1 Development of open-toolset for High Dynamic Range Imaging application

As described in Section 2.5, there exists a need for a user-friendly toolset to facilitate the adoption of low-cost camera sensors for human-centric daylight control or visual comfort studies. In such context, this thesis aims to develop a Python-based open GUI toolset based on Raspberry Pi and its camera module that includes:

- **Camera calibration module:** Although the Pi Camera module is factory-calibrated, attaching the fisheye lens or any specific filter (e.g. neutral density filter) yields extra needs for geometric and photometric calibration per-user customization. The toolset will include the whole calibration procedure. The photometric calibration submodule will adopt Debevec's HDR merging algorithm implemented in OpenCV-Python and will include estimation of: a) camera response function (CRF); b) absolute calibration factor; and c) vignetting curve. The submodule for geometric calibration will be based on OpenCV-Python implementation of Kannala and Brandt's generic camera model [79] which retrieves camera intrinsic parameters and radial fisheye distortion coefficients. The module will allow user to interactively perform minimum-required manual task needed for parameters-estimation and will be compatible with any fisheye lenses up to 180 degrees-FOV.
- **Controller module for window-mounted HDRI sensor:** This module is the implementation of image-based glare detection/positioning, solar tracking, and shade control logics proposed in Chapter 3. It will provide a GUI control panel for HDRI sensor-based shade control logic. The GUI panel will display the exterior luminance distribution continuously changing and information on glare sources detected by the HDRI sensor— average luminance, solid angle, profile angle, etc. Also several shade control logics and relevant parameters – such as detection thresholds for glare source and solar disk, geometry and layout of the room - can be selected by the user. The shade controls include the conventional sun-tracking algorithm, exterior glare protection algorithm and their combination.

- **Glare assessment tool for visual comfort study:** This module is aimed to provide a cost-effective, standardized solution for people who want to conduct human visual comfort studies in buildings. This tool will not only allow the collection user responses and luminance maps but will also provide a user-friendly toolsets to easily build programs suit the purpose. The data collection can be either fully automated or operated manually and includes the rapid calculation of commonly-used visual comfort indicators such as DGP, enabled by a new open glare evaluation package based on Python to enhance the computational efficiency and scalability from existing software (Evalglare).

## 7.2 Improvement of luminance re-projection framework for non-intrusive luminance mapping

The results from Chapter 5 and Chapter 6 show that the proposed framework for non-intrusive monitoring can reasonably predict occupant visual comfort in day-lit perimeter zones. However, there still exist limitations related to the quality of the 3D as-is model reconstructed via SfM-MVS pipeline even it is a long-term-established method. First, SfM under-performs when a reconstructed space is lacking textures, which is not extremely rare in modern offices (e.g. matte-painted walls). Also, a huge opportunity lies in the enhancement of reconstruction for the window region (including the shaded area and exterior scene) to significantly improve the framework performance. To this end, two approaches are proposed:

- **Utilization of computer vision techniques for rapid and precise 3D reconstruction, such as Structured Light or LiDAR.** Such techniques generally require higher-cost devices than SfM-MVS. However, they exhibit better robustness and speed, enabling real-time 3D mapping of the scenes and the cost barrier is also being lowered, thanks to prosperity in computer vision applications.
- **Geo-registration of building surroundings for re-projection of the exterior scene.** Reconstructing the exterior scene via image-based sensing from indoor space is non-robust and sometimes impossible. Thus, instead of re-constructing the exterior scene, we can geo-register the interior space into the readily available urban-scale 3D model that includes the target building and the surroundings. By measuring the exterior luminance map from the HDRI sensor installed in the room and corresponding it to the 3D model of the surrounding, we can create a better re-projection of the exterior scene perceived by the occupants.

### **7.3 Luminance-based human-centric daylight-linked control**

Luminance distribution within occupant FOV has almost-full accountability of human visual perception. Thus the luminance monitoring framework proposed in Chapter 5 has the potential to effectively aid human-centric daylight control to suit personal comfort and preference and maximize health benefits while reducing energy consumption. To this end, modern machine learning techniques including deep learning can be engaged, incorporating the existing knowledge on human visual systems and responses to luminous conditions. The camera sensor is able to continuously monitor luminance conditions, providing a wealth of data in real time. Occupant feedback can be collected through sporadic web surveys and through actions. Image processing and significant variable identification is required before proceeding with AI-enabled learning of preferred luminous scenes. An important achievement goal is to develop a user interface to efficiently enable economical user response collection and delivering a satisfactory user experience for a variety of luminous conditions. A major challenge in this study is associated with data collection and processing, since models such as deep neural networks may require substantial data size due to the information-rich nature of luminance maps without effort to retain the model and data simplicity.



## REFERENCES

- [1] M. Bodart, A. De Herde, Global energy savings in offices buildings by the use of daylighting, *Energy Build.* 34 (2002) 421–429. [https://doi.org/10.1016/S0378-7788\(01\)00117-7](https://doi.org/10.1016/S0378-7788(01)00117-7).
- [2] P. Ihm, A. Nemri, M. Krarti, Estimation of lighting energy savings from daylighting, *Build. Environ.* 44 (2009) 509–514. <https://doi.org/10.1016/j.buildenv.2008.04.016>.
- [3] EIA, 2012 Commercial Buildings Energy Consumption Survey: Energy Usage Summary, 2012.
- [4] Z. Hamedani, E. Solgi, T. Hine, H. Skates, G. Isoardi, R. Fernando, Lighting for work: A study of the relationships among discomfort glare, physiological responses and visual performance, *Build. Environ.* 167 (2020) 106478. <https://doi.org/10.1016/j.buildenv.2019.106478>.
- [5] W.J.M. van Bommel, G.J. van den Beld, Lighting for work: A review of visual and biological effects, *Light. Res. Technol.* 36 (2004) 255–269. <https://doi.org/10.1191/1365782804li122oa>.
- [6] J.A. Veitch, G.R. Newsham, Lighting quality and energy-efficiency effects on task performance, mood, health, satisfaction, and comfort, *J. Illum. Eng. Soc.* 27 (1998) 107–129. <https://doi.org/10.1080/00994480.1998.10748216>.
- [7] M.L. Amundadottir, S. Rockcastle, M. Sarey Khanie, M. Andersen, A human-centric approach to assess daylight in buildings for non-visual health potential, visual interest and gaze behavior, *Build. Environ.* 113 (2017) 5–21. <https://doi.org/10.1016/j.buildenv.2016.09.033>.
- [8] M.B.C. Aries, M.P.J. Aarts, J. Van Hoof, Daylight and health: A review of the evidence and consequences for the built environment, *Light. Res. Technol.* 47 (2015) 6–27. <https://doi.org/10.1177/1477153513509258>.
- [9] A. Borisuit, The Impact of Light Including Non-Image Forming Effects on Visual Comfort, [Ph.D. Thesis]. École Polytechnique Fédérale De Lausanne, 2013.
- [10] P.R. Boyce, Human factors in lighting, third edition, 2014. <https://doi.org/10.1201/b16707>.

- [11] M.G. Figueiro, R. Nagare, L.L.A. Price, Non-visual effects of light: How to use light to promote circadian entrainment and elicit alertness, *Light. Res. Technol.* 50 (2018) 38–62. <https://doi.org/10.1177/1477153517721598>.
- [12] A.D. Galasiu, J.A. Veitch, Occupant preferences and satisfaction with the luminous environment and control systems in daylit offices: a literature review, *Energy Build.* (2006). <https://doi.org/10.1016/j.enbuild.2006.03.001>.
- [13] K. Konis, A novel circadian daylight metric for building design and evaluation, *Build. Environ.* 113 (2017) 22–38. <https://doi.org/10.1016/j.buildenv.2016.11.025>.
- [14] P. Leather, M. Pyrgas, D. Beale, C. Lawrence, Windows in the workplace: Sunlight, View, and Occupational Stress, *Environ. Behav.* 30 (1998) 739–762. <https://doi.org/10.1177/001391659803000601>.
- [15] K. Van Den Wymelenberg, M. Inanici, A Critical Investigation of Common Lighting Design Metrics for Predicting Human Visual Comfort in Offices with Daylight, *LEUKOS - J. Illum. Eng. Soc. North Am.* 10 (2014) 145–164. <https://doi.org/10.1080/15502724.2014.881720>.
- [16] J.A.. Veitch, G.R. Newsham, Preferred Luminous Conditions in Open-Plan Offices: Research and Practice Recommendations, *Light. Res. Technol.* 32 (2000) 199–212. <https://doi.org/10.1177/096032710003200404>.
- [17] Flad Architects, Purdue University, Center for High Performance Buildings, ArchitypeReview. (n.d.). <http://architypereview.com/project/purdue-university-center-for-high-performance-buildings/> (accessed July 4, 2020).
- [18] J.A. Jakubiec, C.F. Reinhart, The 'adaptive zone'-A concept for assessing discomfort glare throughout daylit spaces, *Light. Res. Technol.* 44 (2012) 149–170. <https://doi.org/10.1177/1477153511420097>.
- [19] J.A. Jakubiec, C.F. Reinhart, K. Van Den Wymelenberg, Towards an integrated framework for predicting visual comfort conditions from luminance-based metrics in perimeter daylit spaces, *Build. Simul. Conf.* (2015) 2–9. <http://www.ibpsa.org/proceedings/BS2015/p2106.pdf> (accessed June 6, 2018).
- [20] K. Konis, Evaluating daylighting effectiveness and occupant visual comfort in a side-lit open-plan office building in San Francisco, California, *Build. Environ.* 59 (2013) 662–677. <https://doi.org/10.1016/j.buildenv.2012.09.017>.

- [21] K. Konis, Predicting visual comfort in side-lit open-plan core zones: Results of a field study pairing high dynamic range images with subjective responses, *Energy Build.* 77 (2014) 67–79. <https://doi.org/10.1016/j.enbuild.2014.03.035>.
- [22] I. Konstantzos, M. Kim, A. Tzempelikos, An integrated method and web tool to assess visual environment in spaces with window shades, *Sci. Technol. Built Environ.* 24 (2018) 470–482. <https://doi.org/10.1080/23744731.2018.1438021>.
- [23] E. Shen, J. Hu, M. Patel, Energy and visual comfort analysis of lighting and daylight control strategies, *Build. Environ.* 78 (2014) 155–170. <https://doi.org/10.1016/j.buildenv.2014.04.028>.
- [24] L. Bellia, F. Fragliasso, E. Stefanizzi, Why are daylight-linked controls (DLCs) not so spread? A literature review, *Build. Environ.* 106 (2016) 301–312. <https://doi.org/10.1016/j.buildenv.2016.06.040>.
- [25] E. Reinhard, High dynamic range imaging: acquisition, display, and image-based lighting, Morgan Kaufmann ; Elsevier Science [distributor], San Francisco, CA : Oxford, 2005.
- [26] P.E. Debevec, J. Malik, Recovering high dynamic range radiance maps from photographs, in: *Proc. 24th Annu. Conf. Comput. Graph. Interact. Tech. SIGGRAPH 1997*, 1997: pp. 369–378. <https://doi.org/10.1145/258734.258884>.
- [27] M.N. Inanici, Evaluation of high dynamic range photography as a luminance data acquisition system, *Light. Res. Technol.* 38 (2006) 123–136. <https://doi.org/10.1191/1365782806li164oa>.
- [28] M. Moeck, Accuracy of luminance maps obtained from high dynamic range images, *LEUKOS - J. Illum. Eng. Soc. North Am.* 4 (2007) 99–112. <https://doi.org/10.1582/LEUKOS.2007.04.02.002>.
- [29] Y. Tyukhova, C. Waters, An assessment of high dynamic range luminance measurements with LED lighting, *LEUKOS - J. Illum. Eng. Soc. North Am.* 10 (2014) 87–99. <https://doi.org/10.1080/15502724.2014.861279>.
- [30] C. Cauwerts, M.B. Piderit, Application of high-dynamic range imaging techniques in architecture: A step toward high-quality daylight interiors?, *J. Imaging.* 4 (2018). <https://doi.org/10.3390/jimaging4010019>.

- [31] D. Fan, B. Painter, J. Mardaljevic, A data collection method for long-term field studies of visual comfort in real-world daylit office environments, in: PLEA 2009 - Archit. Energy Occupant's Perspect. Proc. 26th Int. Conf. Passiv. Low Energy Archit., 2009.
- [32] C. Pierson, M. Bodart, J. Wienold, A. Jacobs, Luminance maps from High Dynamic Range imaging : calibrations and adjustments for visual comfort assessment, *Lux Eur.* (2017).
- [33] C. Pierson, C. Cauwerts, M. Bodart, J. Wienold, Tutorial: Luminance Maps for Daylighting Studies from High Dynamic Range Photography, *LEUKOS - J. Illum. Eng. Soc. North Am.* (2019). <https://doi.org/10.1080/15502724.2019.1684319>.
- [34] A. Wagdy, V. Garcia-Hansen, G. Isoardi, K. Pham, A parametric method for remapping and calibrating fisheye images for glare analysis, *Buildings.* 9 (2019) 1–24. <https://doi.org/10.3390/buildings9100219>.
- [35] H. Cai, T.M. Chung, Improving the quality of high dynamic range images, *Light. Res. Technol.* 43 (2011) 87–102. <https://doi.org/10.1177/1477153510371356>.
- [36] J.A. Jakubiec, C.F. Reinhart, A Concept for Predicting Occupants' Long-Term Visual Comfort within Daylit Spaces, *LEUKOS.* 12 (2016) 185–202. <https://doi.org/10.1080/15502724.2015.1090880>.
- [37] I. Konstantzos, A. Tzempelikos, Y.C. Chan, Experimental and simulation analysis of daylight glare probability in offices with dynamic window shades, *Build. Environ.* 87 (2015) 244–254. <https://doi.org/10.1016/j.buildenv.2015.02.007>.
- [38] I. Konstantzos, A. Tzempelikos, Daylight glare evaluation with the sun in the field of view through window shades, *Build. Environ.* 113 (2017) 65–77. <https://doi.org/10.1016/j.buildenv.2016.09.009>.
- [39] J.Y. Suk, M. Schiler, K. Kensek, Investigation of existing discomfort glare indices using human subject study data, *Build. Environ.* 113 (2017) 121–130. <https://doi.org/10.1016/j.buildenv.2016.09.018>.
- [40] J.Y. Suk, M. Schiler, K. Kensek, Development of new daylight glare analysis methodology using absolute glare factor and relative glare factor, *Energy Build.* 64 (2013) 113–122. <https://doi.org/10.1016/j.enbuild.2013.04.020>.
- [41] K. Van Den Wymelenberg, M. Inanici, Evaluating a New Suite of Luminance-Based Design Metrics for Predicting Human Visual Comfort in Offices with Daylight, *LEUKOS - J. Illum. Eng. Soc. North Am.* 12 (2016) 113–138. <https://doi.org/10.1080/15502724.2015.1062392>.

- [42] J. Wienold, J. Christoffersen, Evaluation methods and development of a new glare prediction model for daylight environments with the use of CCD cameras, *Energy Build.* 38 (2006) 743–757. <https://doi.org/10.1016/j.enbuild.2006.03.017>.
- [43] J.A. Yamin Garretón, E.M. Colombo, A.E. Pattini, A global evaluation of discomfort glare metrics in real office spaces with presence of direct sunlight, *Energy Build.* 166 (2018) 145–153. <https://doi.org/10.1016/j.enbuild.2018.01.024>.
- [44] C. Goovaerts, F. Descamps, V.A. Jacobs, Shading control strategy to avoid visual discomfort by using a low-cost camera: A field study of two cases, *Build. Environ.* 125 (2017) 26–38. <https://doi.org/10.1016/j.buildenv.2017.08.030>.
- [45] G.R. Newsham, C. Arsenault, A camera as a sensor for lighting and shading control, *Light. Res. Technol.* 41 (2009) 143–160. <https://doi.org/10.1177/1477153508099889>.
- [46] A. Sarkar, R.G. Mistrick, A novel lighting control system integrating high dynamic range imaging and DALI, *LEUKOS - J. Illum. Eng. Soc. North Am.* 2 (2006) 307–322. <https://doi.org/10.1080/15502724.2006.10747642>.
- [47] T. Kruisselbrink, R. Dangol, E.J. van Loenen, Feasibility of ceiling-based luminance distribution measurements, *Build. Environ.* 172 (2020) 106699. <https://doi.org/10.1016/j.buildenv.2020.106699>.
- [48] A. Motamed, L. Deschamps, J.L. Scartezzini, On-site monitoring and subjective comfort assessment of a sun shadings and electric lighting controller based on novel High Dynamic Range vision sensors, *Energy Build.* 149 (2017) 58–72. <https://doi.org/10.1016/j.enbuild.2017.05.017>.
- [49] IESNA, *Lighting handbook: Reference & application*, 2000.
- [50] J.J. Vos, Reflections on glare, *Light. Res. Technol.* 352 (2003) 163–176. <https://doi.org/10.1191/1477153503li083oa>.
- [51] Commission Internationale de l’Éclairage, CIE. #146 CIE TC 1–50 report CIE equations for disability glare, 2002.
- [52] M.B. Hirning, G.L. Isoardi, I. Cowling, Discomfort glare in open plan green buildings, *Energy Build.* 70 (2014) 427–440. <https://doi.org/10.1016/j.enbuild.2013.11.053>.

- [53] S. Carlucci, F. Causone, F. De Rosa, L. Pagliano, A review of indices for assessing visual comfort with a view to their use in optimization processes to support building integrated design, *Renew. Sustain. Energy Rev.* 47 (2015) 1016–1033. <https://doi.org/10.1016/j.rser.2015.03.062>.
- [54] C. Pierson, J. Wienold, M. Bodart, Review of Factors Influencing Discomfort Glare Perception from Daylight, *LEUKOS - J. Illum. Eng. Soc. North Am.* 14 (2018) 111–148. <https://doi.org/10.1080/15502724.2018.1428617>.
- [55] A. Tzempelikos, Advances on daylighting and visual comfort research, *Build. Environ.* 113 (2017) 1–4. <https://doi.org/10.1016/j.buildenv.2016.12.002>.
- [56] M.B. Hirning, G.L. Isoardi, V.R. Garcia-Hansen, Prediction of discomfort glare from windows under tropical skies, *Build. Environ.* 113 (2017) 107–120. <https://doi.org/10.1016/j.buildenv.2016.08.005>.
- [57] M.B. Hirning, G.L. Isoardi, S. Coyne, V.R. Garcia Hansen, I. Cowling, Post occupancy evaluations relating to discomfort glare: A study of green buildings in Brisbane, *Build. Environ.* 59 (2013) 349–357. <https://doi.org/10.1016/j.buildenv.2012.08.032>.
- [58] R.G. Hopkinson, Glare from daylighting in buildings, *Appl. Ergon.* 3 (1972) 206–215. [https://ac.els-cdn.com/0003687072901020/1-s2.0-0003687072901020-main.pdf?\\_tid=74aba20b-0171-46d5-a92b-b01a260681a6&acdnat=1528298253\\_631fff10d3977c001123953805e30eb0](https://ac.els-cdn.com/0003687072901020/1-s2.0-0003687072901020-main.pdf?_tid=74aba20b-0171-46d5-a92b-b01a260681a6&acdnat=1528298253_631fff10d3977c001123953805e30eb0) (accessed June 6, 2018).
- [59] W.K.E. Osterhaus, Discomfort glare assessment and prevention for daylight applications in office environments, *Sol. Energy.* 79 (2005) 140–158. <https://doi.org/10.1016/j.solener.2004.11.011>.
- [60] P. Chauvel, J.B. Collins, R. Dogniaux, J. Longmore, Glare from windows: current views of the problem, (n.d.). <http://journals.sagepub.com.ezproxy.lib.purdue.edu/doi/pdf/10.1177/096032718201400103> (accessed June 14, 2018).
- [61] W. Kim, J.T. Kim, A prediction method to identify the glare source in a window with non-uniform luminance distribution, *Energy Build.* 46 (2012) 132–138. <https://doi.org/10.1016/j.enbuild.2011.10.037>.

- [62] A.A. Nazzari, A new evaluation method for daylight discomfort glare, *Int. J. Ind. Ergon.* (2005). <https://doi.org/10.1016/j.ergon.2004.08.010>.
- [63] K. Van Den Wymelenberg, Visual comfort, discomfort glare, and occupant fenestration control: Developing a research agenda, *LEUKOS - J. Illum. Eng. Soc. North Am.* 10 (2014) 207–221. <https://doi.org/10.1080/15502724.2014.939004>.
- [64] Sylvester K., Computing visual comfort rating for a specific interior lighting installation, *Illum. Eng.* (1966) 634–642.
- [65] J. Wienold, C. Reetz, T. Kuhn, J. Christoffersen, A new RADIANCE-based tool to evaluate daylight glare in office spaces, 3rd Int. RADIANCE Work. 2004. (2002) 2. [https://www.radiance-online.org/community/workshops/2004-fribourg/presentations/Wienold\\_extabs.pdf](https://www.radiance-online.org/community/workshops/2004-fribourg/presentations/Wienold_extabs.pdf) (accessed June 6, 2018).
- [66] G. Ward, The RADIANCE lighting simulation and rendering system, in: *Proc. 21st Annu. Conf. Comput. Graph. Interact. Tech. SIGGRAPH 1994*, 1994: pp. 459–472. <https://doi.org/10.1145/192161.192286>.
- [67] J. Wienold, Dynamic simulation of blind control strategies for visual comfort and energy balance analysis, in: *IBPSA 2007 - Int. Build. Perform. Simul. Assoc. 2007*, 2007: pp. 1197–1204. [https://www.aivc.org/sites/default/files/p231\\_final.pdf](https://www.aivc.org/sites/default/files/p231_final.pdf) (accessed March 3, 2019).
- [68] J. Wienold, Dynamic Daylight glare Evaluation, *Build. Simul.* (2009) 944–951. <https://doi.org/citeulike-article-id:11069372>.
- [69] F. Cantin, M.C. Dubois, Daylighting metrics based on illuminance, distribution, glare and directivity, *Light. Res. Technol.* 43 (2011) 291–307. <https://doi.org/10.1177/1477153510393319>.
- [70] K. Van Den Wymelenberg, M. Inanici, P. Johnson, The effect of luminance distribution patterns on occupant preference in a daylit office environment, *LEUKOS - J. Illum. Eng. Soc. North Am.* 7 (2010) 103–122. <https://doi.org/10.1582/LEUKOS.2010.07.02003>.
- [71] J. Wienold, T. Iwata, M. Sarey Khanie, E. Errell, E. Kaftan, R.G. Rodriguez, J.A. Yamin Garretton, T. Tzempelikos, I. Konstantzos, J. Christoffersen, T.E. Kuhn, C. Pierson, M. Andersen, Cross-validation and robustness of daylight glare metrics, *Light. Res. Technol.* 51 (2019) 983–1013. <https://doi.org/10.1177/1477153519826003>.

- [72] C. Pierson, M. Sarey Khanie, M. Bodart, J. Wienold, Discomfort glare cut-off values from field and laboratory studies, in: 29th Quadrenn. Sess. CIE, Washington DC, USA, 2019: pp. 295–305. <https://doi.org/10.25039/x46.2019.op41>.
- [73] V. Kumaragurubaran, M. Inanici, Hdrscope: High dynamic range image processing toolkit for lighting simulations and analysis, in: Proc. BS 2013 13th Conf. Int. Build. Perform. Simul. Assoc., 2013.
- [74] G. Ward, Anywhere Software, (n.d.). <http://www.anywhere.com> (accessed April 5, 2019).
- [75] J. Wienold, Evaluation and validation of the calculation of illuminance in evalglare, n.d.
- [76] D. Geisler-Moroder, E.S. Lee, G.J. Ward, Validation of the Five-Phase Method for Simulating Complex Fenestration Systems with Radiance against Field Measurements, United States, 2016.
- [77] D. Scaramuzza, A. Martinelli, R. Siegwart, A toolbox for easily calibrating omnidirectional cameras, in: IEEE Int. Conf. Intell. Robot. Syst., 2006. <https://doi.org/10.1109/IROS.2006.282372>.
- [78] Mathworks, Fisheye Calibration Basics, (n.d.). <https://www.mathworks.com/help/vision/ug/fisheye-calibration-basics.html> (accessed July 15, 2020).
- [79] J. Kannala, S.S. Brandt, A generic camera model and calibration method for conventional, wide-angle, and fish-eye lenses, IEEE Trans. Pattern Anal. Mach. Intell. 28 (2006) 1335–1340. <https://doi.org/10.1109/TPAMI.2006.153>.
- [80] OpenCV, OpenCV Library, (n.d.). <https://doi.org/OpenCV>.
- [81] J.A. Jakubiec, C.F. Reinhart, Assessing disability glare potential of reflections from new construction: Case study analysis and recommendations for the future, in: Proc. Transp. Res. Board 93rd Annu. Meet., 2014. <https://doi.org/10.3141/2449-13>.
- [82] J.A. Jakubiec, C. Reinhart, The “adaptive zone” - A concept for Assessing glare throughout daylight spaces, in: Proc. Build. Simul. 2011 12th Conf. Int. Build. Perform. Simul. Assoc., 2011: pp. 2178–2185.
- [83] J.Y. Suk, M. Schiler, K. Kensek, Investigation of Evalglare software, daylight glare probability and high dynamic range imaging for daylight glare analysis, Light. Res. Technol. 45 (2013) 450–463. <https://doi.org/10.1177/1477153512458671>.



- [84] J.Y. Suk, M. Schiler, K. Kensek, Absolute glare factor and relative glare factor based metric: Predicting and quantifying levels of daylight glare in office space, *Energy Build.* 130 (2016) 8–19. <https://doi.org/10.1016/j.enbuild.2016.08.021>.
- [85] P. Debevec, Image-based lighting, *IEEE Comput. Graph. Appl.* 22 (2002) 26–34. <https://doi.org/10.1109/38.988744>.
- [86] R. Perez, R. Seals, J. Michalsky, All-weather model for sky luminance distribution- Preliminary configuration and validation, *Sol. Energy.* 50 (1993) 235–245. [https://doi.org/10.1016/0038-092X\(93\)90017-I](https://doi.org/10.1016/0038-092X(93)90017-I).
- [87] N.L. Jones, C.F. Reinhart, Experimental validation of ray tracing as a means of image-based visual discomfort prediction, *Build. Environ.* 113 (2017) 131–150. <https://doi.org/10.1016/j.buildenv.2016.08.023>.
- [88] M. Inanici, Evaluation of high dynamic range image based sky models in lighting simulation, *LEUKOS J. Illum. Eng. Soc. North Am.* 7 (2010) 69–84. <https://doi.org/10.1582/LEUKOS.2010.07.02001>.
- [89] Comission Internationale de L'Eclairage, Spatial distribution of daylight\_CIE standard general sky, Cie S 011/E2003. (2003).
- [90] Y. Wu, J.H. Kämpf, J.L. Scartezzini, Design and validation of a compact embedded photometric device for real-time daylighting computing in office buildings, *Build. Environ.* 148 (2019) 309–322. <https://doi.org/10.1016/j.buildenv.2018.11.016>.
- [91] H. Bülow-Hübe, M. Wall, Solar projection in buildings (No. TABK--01/3060), Lund, Sweden, 2001.
- [92] M. Foster, T. Oreszczyn, Occupant control of passive systems: The use of Venetian blinds, *Build. Environ.* (2001). [https://doi.org/10.1016/S0360-1323\(99\)00074-8](https://doi.org/10.1016/S0360-1323(99)00074-8).
- [93] V. Inkarojrit, Monitoring and modelling of manually-controlled venetian blinds in private offices: A pilot study, *J. Build. Perform. Simul.* 1 (2008) 75–89. <https://doi.org/10.1080/19401490802021012>.
- [94] T. Inoue, T. Kawase, T. Ibamoto, S. Takakusa, Y. Matsuo, The development of an optimal control system for window shading devices based on investigations in office buildings, *ASHRAE Trans.* (1988).

- [95] W. O'Brien, K. Kapsis, A.K. Athienitis, Manually-operated window shade patterns in office buildings: A critical review, *Build. Environ.* 60 (2013) 319–338. <https://doi.org/10.1016/j.buildenv.2012.10.003>.
- [96] M.S. Rea, Window blind occlusion: a pilot study, *Build. Environ.* 19 (1984) 133–137. [https://doi.org/10.1016/0360-1323\(84\)90038-6](https://doi.org/10.1016/0360-1323(84)90038-6).
- [97] C.F. Reinhart, K. Voss, Monitoring manual control of electric lighting and blinds, *Light. Res. Technol.* 35 (2003) 243–260. <https://doi.org/10.1191/1365782803li064oa>.
- [98] A.I. Rubin, B.L. Collins, R.L. Tibbott, Window blinds as a potential energy saver - a case study, *NBS Build. Sci. Ser.* (1978).
- [99] A. Tzempelikos, H. Shen, Comparative control strategies for roller shades with respect to daylighting and energy performance, *Build. Environ.* 67 (2013) 179–192. <https://doi.org/10.1016/j.buildenv.2013.05.016>.
- [100] H. Shen, A. Tzempelikos, Daylight-linked synchronized shading operation using simplified model-based control, *Energy Build.* 145 (2017) 200–212. <https://doi.org/10.1016/j.enbuild.2017.04.021>.
- [101] S.Y. Koo, M.S. Yeo, K.W. Kim, Automated blind control to maximize the benefits of daylight in buildings, *Build. Environ.* 45 (2010) 1508–1520. <https://doi.org/10.1016/j.buildenv.2009.12.014>.
- [102] Y.C. Chan, A. Tzempelikos, Efficient venetian blind control strategies considering daylight utilization and glare protection, *Sol. Energy.* 98 (2013) 241–254. <https://doi.org/10.1016/j.solener.2013.10.005>.
- [103] G. Yun, K.C. Yoon, K.S. Kim, The influence of shading control strategies on the visual comfort and energy demand of office buildings, *Energy Build.* 84 (2014) 70–85. <https://doi.org/10.1016/j.enbuild.2014.07.040>.
- [104] M. Inanici, A. Hashemloo, An investigation of the daylighting simulation techniques and sky modeling practices for occupant centric evaluations, *Build. Environ.* 113 (2017) 220–231. <https://doi.org/10.1016/j.buildenv.2016.09.022>.
- [105] I. Din, H. Kim, Joint blind and light control for lighting energy reduction while satisfying light level and anti-glare requirements, *Light. Res. Technol.* 46 (2014) 281–292. <https://doi.org/10.1177/1477153513497740>.

- [106] K. Kapsis, A. Tzempelikos, A.K. Athienitis, R.G. Zmeureanu, Daylighting performance evaluation of a bottom-up motorized roller shade, *Sol. Energy*. 84 (2010) 2120–2131. <https://doi.org/10.1016/j.solener.2010.09.004>.
- [107] Y.C. Chan, A. Tzempelikos, I. Konstantzos, A systematic method for selecting roller shade properties for glare protection, *Energy Build.* 92 (2015) 81–94. <https://doi.org/10.1016/j.enbuild.2015.01.057>.
- [108] M. Konstantoglou, A. Tsangrassoulis, Dynamic operation of daylighting and shading systems: A literature review, *Renew. Sustain. Energy Rev.* 60 (2016) 268–283. <https://doi.org/10.1016/j.rser.2015.12.246>.
- [109] B. O'Neill, Model-based control of venetian blinds, Concordia University, 2008.
- [110] J. Xiong, A. Tzempelikos, Model-based shading and lighting controls considering visual comfort and energy use, *Sol. Energy*. 134 (2016) 416–428. <https://doi.org/10.1016/j.solener.2016.04.026>.
- [111] J. Wienold, F. Frontini, S. Herkel, S. Mende, Climate based simulation of different shading device systems for comfort and energy demand, in: *Proc. Build. Simul. 2011 12th Conf. Int. Build. Perform. Simul. Assoc.*, 2011: pp. 2680–2687. [http://ibpsa.org/proceedings/BS2011/P\\_1833.pdf](http://ibpsa.org/proceedings/BS2011/P_1833.pdf) (accessed March 14, 2019).
- [112] L. Karlsen, P. Heiselberg, I. Bryn, Occupant satisfaction with two blind control strategies: Slats closed and slats in cut-off position, *Sol. Energy*. 115 (2015) 166–179. <https://doi.org/10.1016/j.solener.2015.02.031>.
- [113] T. Iwata, T. Taniguchi, R. Sakuma, Automated blind control based on glare prevention with dimmable light in open-plan offices, *Build. Environ.* 113 (2017) 232–246. <https://doi.org/10.1016/j.buildenv.2016.08.034>.
- [114] L. Wang, H. Li, X. Zou, X. Shen, Lighting system design based on a sensor network for energy savings in large industrial buildings, *Energy Build.* 105 (2015) 226–235. <https://doi.org/10.1016/j.enbuild.2015.07.053>.
- [115] H. Shen, A. Tzempelikos, Daylighting and energy analysis of private offices with automated interior roller shades, *Sol. Energy*. 86 (2012) 681–704. <https://doi.org/10.1016/j.solener.2011.11.016>.
- [116] L. Roche, Summertime performance of an automated lighting and blinds control system, *Light. Res. Technol.* 34 (2002) 11–25. <https://doi.org/10.1191/1365782802li026oa>.

- [117] A. Atzeri, F. Cappelletti, A. Gasparella, Internal versus external shading devices performance in office buildings, *Energy Procedia*. 45 (2014) 463–472. <https://doi.org/10.1016/j.egypro.2014.01.050>.
- [118] G. Yun, D.Y. Park, K.S. Kim, Appropriate activation threshold of the external blind for visual comfort and lighting energy saving in different climate conditions, *Build. Environ.* 113 (2017) 247–266. <https://doi.org/10.1016/j.buildenv.2016.11.021>.
- [119] P. Chaiwiwatworakul, S. Chirarattananon, P. Rakkwamsuk, Application of automated blind for daylighting in tropical region, *Energy Convers. Manag.* 50 (2009) 2927–2943. <https://doi.org/10.1016/j.enconman.2009.07.008>.
- [120] C.F. Reinhart, Lightswitch-2002: A model for manual and automated control of electric lighting and blinds, *Sol. Energy*. 77 (2004) 15–28. <https://doi.org/10.1016/j.solener.2004.04.003>.
- [121] M.H. Oh, K.H. Lee, J.H. Yoon, Automated control strategies of inside slat-type blind considering visual comfort and building energy performance, *Energy Build.* 55 (2012) 728–737. <https://doi.org/10.1016/j.enbuild.2012.09.019>.
- [122] R. Mistrick, C.H. Chen, A. Bierman, D. Felts, A comparison of photosensor-controlled electronic dimming systems in a small office, *J. Illum. Eng. Soc.* 29 (2000) 66–80. <https://doi.org/10.1080/00994480.2000.10748483>.
- [123] A. Bierman, K.M. Conway, Characterizing daylight photosensor system performance to help overcome market barriers, *J. Illum. Eng. Soc.* 29 (2000) 101–115. <https://doi.org/10.1080/00994480.2000.10748486>.
- [124] C. Ehrlich, K. Papamichael, J. Lai, K. Revzan, A method for simulating the performance of photosensor-based lighting controls, *Energy Build.* 34 (2002) 883–889. [https://doi.org/10.1016/S0378-7788\(02\)00064-6](https://doi.org/10.1016/S0378-7788(02)00064-6).
- [125] A.S. Choi, K.D. Song, Y.S. Kim, The characteristics of photosensors and electronic dimming ballasts in daylight responsive dimming systems, *Build. Environ.* 40 (2005) 39–50. <https://doi.org/10.1016/j.buildenv.2004.07.014>.
- [126] J. Kim, K. Yang, Y. Park, K. Lee, M. Yeo, K. Kim, An Experimental Study for the Evaluation of the Environmental Performance by the Application of the Automated Venetian Blind, (2007).

- [127] M. Chiogna, R. Albatici, A. Frattari, Electric lighting at the workplace in offices: Efficiency improvement margins of automation systems, *Light. Res. Technol.* 45 (2013) 550–567. <https://doi.org/10.1177/1477153512461372>.
- [128] D. Baillie, Lighting Trends: Lighting Decisions, *Today's Facil. Manag.* (2013). <https://facilityexecutive.com/2013/04/lighting-trends-lighting-decisions/>.
- [129] J. Xiong, A. Tzempelikos, I. Bilonis, P. Karava, A personalized daylighting control approach to dynamically optimize visual satisfaction and lighting energy use, *Energy Build.* (2019). <https://doi.org/10.1016/j.enbuild.2019.03.046>.
- [130] P. Wankanapon, R.G. Mistrick, Roller Shades and Automatic Lighting Control with Solar Radiation Control Strategies, *Built.* 1 (2011) 35–42.
- [131] Y.C. Chan, A. Tzempelikos, A hybrid ray-tracing and radiosity method for calculating radiation transport and illuminance distribution in spaces with venetian blinds, *Sol. Energy.* 86 (2012) 3109–3124. <https://doi.org/10.1016/j.solener.2012.07.021>.
- [132] T.I. and M. Tokura, Position index for a glare source located below, *Light. Res. Technol.* 29 (1996) 172–178.
- [133] T.W. Kruisselbrink, M. Aries, A. Rosemann, A Practical Device for Measuring the Luminance Distribution, *Int. J. Sustain. Light.* 19 (2017) 75–90. <https://doi.org/10.26607/ijsl.v19i1.76>.
- [134] M. Kim, I. Konstantzos, A. Tzempelikos, A low-cost stereo-fisheye camera sensor for daylighting and glare control, *J. Phys. Conf. Ser.* 1343 (2019). <https://doi.org/10.1088/1742-6596/1343/1/012157>.
- [135] M. Kim, I. Konstantzos, A. Tzempelikos, Real-time daylight glare control using a low-cost, window-mounted HDRI sensor, *Build. Environ.* 177 (2020) 106912. <https://doi.org/10.1016/j.buildenv.2020.106912>.
- [136] G.K. Adam, P.A. Kontaxis, L.T. Doulos, E.N.D. Madias, C.A. Bouroussis, F. V. Topalis, Embedded microcontroller with a CCD camera as a digital lighting control system, *Electron.* 8 (2019) 33. <https://doi.org/10.3390/electronics8010033>.
- [137] Raspberry Pi Foundation, Raspberry Pi 3 Model B+, (n.d.). <http://www.raspberrypi.org/products/raspberry-pi-3-model-b/> (accessed April 5, 2019).

- [138] Picamera Library, (n.d.). <https://picamera.readthedocs.io/> (accessed May 24, 2020).
- [139] J. Mardaljevic, S. Cannon-Brookes, N. Blades, K. Lithgow, Reconstruction of cumulative daylight illumination fields from high dynamic range imaging: Theory, deployment and in-situ validation, *Light. Res. Technol.* (2020). <https://doi.org/10.1177/1477153520945755>.
- [140] A. Motamed, L. Deschamps, J. Scartezzini, Validation and Preliminary Experiments of Embedded Discomfort Glare Assessment through a Novel HDR Vision Sensor, *Cisbat.* (2015) 235–240.
- [141] Doulos L.T., Tsangrassoulis A., Bouroussis C.A., Topalis F.V., Reviewing drawbacks of conventional photosensors: are ccd/cmos sensors the next generation?, *Lux Eur. 2013, 12th Eur. Light. Conf.* (2013). <http://daysim.ning.com/> (accessed April 25, 2020).
- [142] K. Van Den Wymelenberg, Evaluating Human Visual Preference and Performance in an Office Environment Using Luminance-based Metrics, 2012. <https://doi.org/10.1017/CBO9781107415324.004>.
- [143] A. Motamed, B. Bueno, L. Deschamps, T.E. Kuhn, J.L. Scartezzini, Self-commissioning glare-based control system for integrated venetian blind and electric lighting, *Build. Environ.* 171 (2020) 106642. <https://doi.org/10.1016/j.buildenv.2019.106642>.
- [144] J. Awange, J. Kiema, *Fundamentals of Photogrammetry*, 2019. [https://doi.org/10.1007/978-3-030-03017-9\\_11](https://doi.org/10.1007/978-3-030-03017-9_11).
- [145] J.S. Aber, I. Marzolf, J.B. Ries, S.E.W. Aber, *Principles of Photogrammetry*, 2019. <https://doi.org/10.1016/b978-0-12-812942-5.00003-3>.
- [146] J.L. Schönberger, J.M. Frahm, Structure-from-Motion Revisited, in: *Proc. IEEE Comput. Soc. Conf. Comput. Vis. Pattern Recognit.*, 2016: pp. 4104–4113. <https://doi.org/10.1109/CVPR.2016.445>.
- [147] D.G. Lowe, Distinctive image features from scale-invariant keypoints, *Int. J. Comput. Vis.* (2004). <https://doi.org/10.1023/B:VISI.0000029664.99615.94>.
- [148] N. Micheletti, J.H. Chandler, S.N. Lane, Investigating the geomorphological potential of freely available and accessible structure-from-motion photogrammetry using a smartphone, *Earth Surf. Process. Landforms.* 40 (2015) 473–486. <https://doi.org/10.1002/esp.3648>.
- [149] S. Bianco, G. Ciocca, D. Marelli, Evaluating the performance of structure from motion pipelines, *J. Imaging.* 4 (2018) 1–18. <https://doi.org/10.3390/jimaging4080098>.

- [150] H. Son, C. Kim, Y. Turkan, Scan-to-BIM-an overview of the current state of the art and a look ahead, 32nd Int. Symp. Autom. Robot. Constr. Min. Connect. to Futur. Proc. (2015).
- [151] Q. Wang, J. Guo, M.K. Kim, An application oriented scan-to-bim framework, Remote Sens. 11 (2019). <https://doi.org/10.3390/rs11030365>.
- [152] V. Badenko, A. Fedotov, D. Zotov, S. Lytkin, D. Volgin, R.D. Garg, L. Min, Scan-to-bim methodology adapted for different application, Int. Arch. Photogramm. Remote Sens. Spat. Inf. Sci. - ISPRS Arch. 42 (2019) 1–7. <https://doi.org/10.5194/isprs-archives-XLII-5-W2-1-2019>.
- [153] cctvopticallens.com, (n.d.). <http://www.cctvopticallens.com/product/300W-105mm-14inch-fisheye-lens.html> (accessed July 15, 2020).
- [154] J. Stumpfel, A. Jones, A. Wenger, C. Tchou, T. Hawkins, P. Debevec, Direct HDR capture of the sun and sky, in: ACM SIGGRAPH 2004 Posters, SIGGRAPH 2004, 2004: p. 50. <https://doi.org/10.1145/1186415.1186473>.
- [155] Pyephem-Sunpath, (n.d.). [https://github.com/santoshphilip/pyephem\\_sunpath](https://github.com/santoshphilip/pyephem_sunpath) (accessed July 16, 2020).
- [156] Niagara AX software, Tridium Inc. (n.d.). <https://www.tridium.com/en/products-services/niagara-ax> (accessed July 8, 2020).
- [157] Y. Tyukhova, C.E. Waters, Subjective and pupil responses to discomfort glare from small, high-luminance light sources, Light. Res. Technol. 51 (2019) 592–611. <https://doi.org/10.1177/1477153518772000>.
- [158] Z. Hamedani, E. Solgi, H. Skates, T. Hine, R. Fernando, J. Lyons, K. Dupre, Visual discomfort and glare assessment in office environments: A review of light-induced physiological and perceptual responses, Build. Environ. 153 (2019) 267–280. <https://doi.org/10.1016/j.buildenv.2019.02.035>.
- [159] J.L. Schönberger, E. Zheng, J.M. Frahm, M. Pollefeys, Pixelwise view selection for unstructured multi-view stereo, Lect. Notes Comput. Sci. (Including Subser. Lect. Notes Artif. Intell. Lect. Notes Bioinformatics). 9907 LNCS (2016) 501–518. [https://doi.org/10.1007/978-3-319-46487-9\\_31](https://doi.org/10.1007/978-3-319-46487-9_31).
- [160] OpenMVS, OpenMVS: open Multi-View Stereo reconstruction library, GitHub Repos. (2020).

- [161] X-Rite, ColorChecker Classic, (n.d.). <https://xritephoto.com/colorchecker-classic> (accessed February 5, 2020).
- [162] S. Safranek, R.G. Davis, Sources of Error in HDRI for Luminance Measurement: A Review of the Literature, *LEUKOS - J. Illum. Eng. Soc. North Am.* 00 (2020) 1–13. <https://doi.org/10.1080/15502724.2020.1721018>.
- [163] Z. Zhang, A flexible new technique for camera calibration, *IEEE Trans. Pattern Anal. Mach. Intell.* (2000). <https://doi.org/10.1109/34.888718>.
- [164] E.K. Stathopoulou, M. Welponer, F. Remondino, Open-source image-based 3D reconstruction pipelines: Review, comparison and evaluation, *Int. Arch. Photogramm. Remote Sens. Spat. Inf. Sci. - ISPRS Arch.* 42 (2019) 331–338. <https://doi.org/10.5194/isprs-archives-XLII-2-W17-331-2019>.
- [165] P. Moulon, P. Monasse, R. Perrot, R. Marlet, OpenMVG: Open Multiple View Geometry, 10214 (2017) 60–74. <https://doi.org/10.1007/978-3-319-56414-2>.
- [166] S. Shen, Accurate multiple view 3D reconstruction using patch-based stereo for large-scale scenes, *IEEE Trans. Image Process.* (2013). <https://doi.org/10.1109/TIP.2013.2237921>.
- [167] Q.-Y. Zhou, J. Park, V. Koltun, Open3D: A Modern Library for 3D Data Processing, (2018). <http://arxiv.org/abs/1801.09847>.
- [168] A. Mikhailov, Turbo, An Improved Rainbow Colormap for Visualization, Google AI Blog. (2019). <https://ai.googleblog.com/2019/08/turbo-improved-rainbow-colormap-for.html> (accessed December 12, 2020).
- [169] J. Wienold, T. Iwata, S.K. M., E. Erell, Kraftan Eran, Rodriguez R., T.T. Yamin Garretton J. A., K. I., Christoffersen J., K.T. E., P. C., A. M., Cross-validation and robustness of daylight glare metrics, *Light. Res. Technol.* 0 (2019) 1–31. <https://doi.org/10.1177/1477153519826003>.
- [170] J. Wienold, Daylight glare analysis and metrics, n.d. [https://www.radiance-online.org/community/workshops/2014-london/presentations/day1/Wienold\\_glare\\_rad.pdf](https://www.radiance-online.org/community/workshops/2014-london/presentations/day1/Wienold_glare_rad.pdf).
- [171] Z. Wang, A.C. Bovik, H.R. Sheikh, E.P. Simoncelli, Image quality assessment: From error visibility to structural similarity, *IEEE Trans. Image Process.* 13 (2004) 600–612. <https://doi.org/10.1109/TIP.2003.819861>.
- [172] R. German Rodriguez, J.A.Y. Garret, A.E. Pattini, An epidemiological approach to daylight discomfort glare, (2016). <https://doi.org/10.1016/j.buildenv.2016.09.028>.



- [173] D.W. Hosmer, S. Lemeshow, R.X. Sturdivant, U.S. Army Academy, Applied Logistic Regression Third Edition, 2013. [www.wiley.com](http://www.wiley.com).

## **VITA**

**Ph.D.**, Lyles School of Civil Engineering, Purdue University (2016 – 2021)

**M.S.**, School of Architecture, Carnegie Mellon University (2014 – 2016)

**B.S.**, Department of Architectural Engineering, Yonsei University (2006 – 2014)

## PUBLICATIONS

### REFEREED JOURNAL PAPERS:

1. **Kim, M.**, & Tzempelikos, A. (2021). Semi-automated luminance map re-projection via high dynamic range imaging and indoor space 3-D reconstruction. *Automation in Construction*, 129, 103812. <https://doi.org/10.1016/j.autcon.2021.103812>
2. Konstantzos, I., Sadeghi, S. A., **Kim, M.**, Xiong, J., & Tzempelikos, A. (2020). The effect of lighting environment on task performance in buildings – A review. *Energy and Buildings*, 226, 110394. <https://doi.org/10.1016/j.enbuild.2020.110394>
3. **Kim, M.**, Konstantzos, I., & Tzempelikos, A. (2020). Real-time daylight glare control using a low-cost, window-mounted HDRI sensor. *Building and Environment*, 177(January), 106912. <https://doi.org/10.1016/j.buildenv.2020.106912>
4. Konstantzos, I., **Kim, M.** & Tzempelikos, A. (2018). An integrated method and web tool to assess visual environment in spaces with window shades. *Science and Technology for the Built Environment*, 24(5), 470–482. <https://doi.org/10.1080/23744731.2018.1438021>

### JOURNAL PAPER IN PREPARATION:

1. **Kim, M.**, & Tzempelikos, A. (2021). Performance evaluation of non-intrusive luminance mapping towards human-centric daylighting control, *submitted to Building & Environment*

### REFERRED CONFERENCE PROCEEDING:

1. **Kim, M.**, Zhang, H., Tzempelikos, A., Gasparella, A., & Cappelletti, F. (2021). Non-Intrusive Luminance Monitoring Framework via High Dynamic Range Imaging and 3-D Reconstruction, Indoor Air 2020, Athens, Greece, May 2022).
2. **Kim, M.**, & Tzempelikos, A. (2021). New Low-Cost Sensing Network for Indoor Environmental Monitoring and Control in Buildings, Indoor Air 2020, Athens, Greece, May 2022)
3. Mah, D., **Kim, M.**, & Tzempelikos, A. (2021). Utilization of programmable cameras for web-based sensing and control of daylight in buildings, CISBAT 2021, Laussane, Switzerland, September 2021.
4. **Kim, M.**, & Tzempelikos, A. (2021). Non-Intrusive Luminance Monitoring Framework via High Dynamic Range Imaging and 3-D Reconstruction, CISBAT 2021, Laussane, Switzerland, September 2021.
5. Zhang, H., **Kim, M.**, Liu, X., & Tzempelikos, A. (2021). A Comparison of Sensing Type And Control Complexity Techniques For Personalized Thermal Comfort. *ASHRAE Transactions*, 127(1), 2021.
6. **Kim, M.**, Konstantzos, I., & Tzempelikos, A. (2019). A low-cost stereo-fisheye camera sensor for daylighting and glare control. *Journal of Physics: Conference Series*, 1343(1). <https://doi.org/10.1088/1742-6596/1343/1/012157>.

#### **NON-REFERREED CONFERENCE PROCEEDING:**

1. **Kim, M.**, Konstantzos, I., & Tzempelikos, A. (2018). A New Control Framework for the Visual Environment Based on Low-Cost HDR Luminance Acquisition. Proceedings of 5th High Performance Buildings Conference at Purdue.

#### **POSTER PRESENTATIONS:**

2. **Kim, M.**, & Tzempelikos, A. “Real-time daylighting control using a smart low-cost HDRI sensor”. Presented at the Sigma Xi 2020 graduate research poster award competition at Purdue, February 2020.
3. **Kim, M.**, Konstantzos, I., & Tzempelikos, A. “Low-cost Sensing Network for Indoor Environmental Monitoring and Control in Buildings”. Presented at the Herrick Industrial Advisory Committee (IAC) meeting, Oct 2017.